AD-766 240

AN EMPIRICAL MODEL OF THE POLAR IONOSPHERE

Terence J. Elkins

Air Force Cambridge Research Laboratories
L. G. Hanscom Field, Massachusetts

23 May 1973

AFCRL-TR-73-0331
23 MAY 1973
AIR FORCE SURVEYS IN GEOPHYSICS, NO. 267

AIR FORCE CAMBRIDGE RESEARCH LABORATORIES
L. G. HANSCOM FIELD, BEDFORD, MASSACHUSETTS

An Empirical Model of the Polar Ionosphere

TERENCE J. ELKINS, Editor

AIR FORCE SYSTEMS COMMAND
United States Air Force

Unclassified
Security Classification

DOCUMENT CONTROL DATA - R&D

(Security classification of title, body of abstract and indexing annotation must be entered when the overall report is classified)

1. ORIGINATING ACTIVITY *(Corporate author)* Air Force Cambridge Research Laboratories (LII) L. G. Hanscom Field Bedford, Massachusetts 01730	2a. REPORT SECURITY CLASSIFICATION Unclassified 2b. GROUP

3. REPORT TITLE

AN EMPIRICAL MODEL OF THE POLAR IONOSPHERE

4. DESCRIPTIVE NOTES *(Type of report and inclusive dates)*
Scientific. Interim.

5. AUTHOR(S) *(First name, middle initial, last name)*

Terence J. Elkins, Editor

6. REPORT DATE 23 May 1973	7a. TOTAL NO. OF PAGES ~~150~~ 157	7b. NO. OF REFS 55
8a. CONTRACT OR GRANT NO.	9a. ORIGINATOR'S REPORT NUMBER(S) AFCRL-TR-73-0331	
b. PROJECT, TASK, WORK UNIT NOS. 56311801 c. DOD ELEMENT 62101F d. DOD SUBELEMENT	9b. OTHER REPORT NO(S) *(Any other numbers that may be assigned this report)* AFSG No. 267	

10. DISTRIBUTION STATEMENT

Approval for Public Release; distribution unlimited.

11. SUPPLEMENTARY NOTES TECH, OTHER	12. SPONSORING MILITARY ACTIVITY Air Force Cambridge Research Laboratories (LII) L. G. Hanscom Field Bedford, Massachusetts 01730

13. ABSTRACT

Four separate articles are collected which deal with the construction of empirical models of the polar ionosphere. The particular emphasis in these articles is towards the radio propagation application of the models. Numerical models of the vertical electron density profiles on the topside and bottomside of the F-region are developed, and a model for sporadic-E is included. Special attention is devoted to features which are characteristic of the polar ionosphere—auroral effects, the trough, and magnetospheric cleft regions. The models are constructed specifically for convenience in computer programming, and in fact, all aspects of the models contained in this report are available in the form of Fortran computer programs.

DD FORM 1 NOV 68 1473

Unclassified
Security Classification

14. KEY WORDS	LINK A		LINK B		LINK C	
	ROLE	WT	ROLE	WT	ROLE	WT
Polar ionosphere						
Radio propagation						
Ionospheric model						

AFCRL-TR-73-0331
23 MAY 1973
AIR FORCE SURVEYS IN GEOPHYSICS, NO. 267

IONOSPHERIC PHYSICS LABORATORY PROJECT 5631

AIR FORCE CAMBRIDGE RESEARCH LABORATORIES

L. G. HANSCOM FIELD, BEDFORD, MASSACHUSETTS

An Empirical Model of the Polar Ionosphere

TERENCE J. ELKINS, Editor

AIR FORCE SYSTEMS COMMAND

United States Air Force

Abstract

Four separate articles are collected which deal with the construction of empirical models of the polar ionosphere. The particular emphasis in these articles is towards the radio propagation application of the models. Numerical models of the vertical electron density profiles on the topside and bottomside of the F-region are developed, and a model for sporadic-E is included. Special attention is devoted to features which are characteristic of the polar ionosphere—auroral effects, the trough, and magnetospheric cleft regions. The models are constructed specifically for convenience in computer programming, and in fact, all aspects of the models contained in this report are available in the form of Fortran computer programs.

Introduction

General

This report consists of four separate articles (Chapters 1 through 4) that attempts to construct the most complete model of the polar ionosphere which the present state of the modeling art will permit. There are a number of points which, if mentioned here at the outset, will help to explain many details of the model and the reasons for certain specific approaches. First and foremost, this model has been constructed with a particular aim in mind, and its form and substance reflect that aim. The model is intended primarily to provide the information necessary to plan and implement systems, operating or planned to operate in the polar environment, which make use of radio waves propagated either via or through the ionosphere. The prime requirement of such a model is accuracy in specifying or predicting the three-dimensional distribution of electron density as a function of time and other relevant physical parameters. Other important requirements are the specification of the statistical distributions of random or quasirandom variables, simplicity, and compactness. These last requirements are mainly imposed by the necessity of programming the model into an on-site system computer, which typically has numerous other duties to perform simultaneously. The requirements for accuracy and simplicity are generally in conflict and force certain compromises in formulating the model.

There are two general classes of a model—theoretical and empirical. The theoretical model is based upon the ability to understand the basic physical processes which govern the formation and distribution of ionospheric plasma, and to

formulate them in a mathematically tractable manner. Such a model always requires some minimal amount of input data, and usually involves the physical and mathematical delineation of boundaries, beyond which the model is undefined. On the other hand, empirical models require large amounts of suitable data, collected at frequent enough intervals in time and on a sufficiently "fine" spatial grid to satisfy the model requirements. Most models of complex physical entities, like the polar ionosphere, fall somewhere between the two extreme limits described here. The present model is largely empirical, since the complexity of the physical processes in the polar ionosphere makes an accurate theoretical model impossible at present. Even an empirical model, however, has its limitations, quite apart from the purely practical problem of analyzing and reducing large amounts of data. The scale of significant polar ionospheric phenomena is, in general, smaller than that of the available data gathering network, and the variability of many parameters is so great that available data is often insufficient to determine necessary empirical relationships with the desirable accuracy. The model, therefore, is necessarily deficient in some respects, and further work is required in order to improve it.

While the orientation of this model is basically practical, it has other applications as well. Since it has been developed almost exclusively from actual measured data, it represents an approximation to "reality" which theoretical models might aim to reproduce. Moreover, since theoretical models must consider certain interactive phenomena—such as the coupling between neutral and ionized atmospheric constituents or Joule heating due to ionospheric currents—this model can serve as a starting point in iterative procedures which ultimately generate self-consistent models.

Summary of Report

The first article (Chapter 1) deals with a survey of previous research on many aspects of the physics of the polar ionosphere. It is pointed out that the polar ionosphere is a region more or less directly connected to the solar wind, which itself may be considered as the extension of the solar corona. This connection between ionosphere and solar wind is a complex one, involving large scale processes in the magnetosphere; that is, the earth's magnetic environment. Therefore an understanding of the polar ionosphere entails an understanding of magnetospheric phenomena, to a much greater degree than is required in the case of the temperate or midlatitude ionosphere. A brief review of the pertinent properties of the neutral atmosphere is given, followed by a review of the formation of the ionosphere from the neutral atmosphere.

Following this review, an analysis is presented leading to the formulation of a predictive model of the ionosphere, based on various kinds of data (ground-based

radio propagation, optical and satellite observations). In some instances, for example the normal D-region, relatively simple deterministic models are found to be adequate. In other cases, such as the models for F-region plasma density, a considerably more complex model is required, which is partly deterministic and partly statistical. In still other cases (sporadic-E model), a predominantly statistical model is used.

The polar ionosphere may be described in terms of several boundaries or dominant morphological features, which display certain regular characteristics when examined in the appropriate frame of reference. Among these notable features are the "trough" and the plasma ring irregularity boundary. The second article (Chapter 2) by Sagalyn et al is devoted to a detailed statistical study of these features, as observed by plasma probes mounted on orbiting satellites.

Another difficult problem, which has a number of useful practical and theoretical applications, is the modeling of the electron density profile in the presence of an active auroral display. Article 3 (Chapter 3) by Ulwick describes techniques by which this can be done. The high energy tail of the auroral particle energy spectrum is precipitated equatorwards of the particles responsible for optical emissions. These higher energy particles penetrate into the lower ionosphere, where the collision frequency between electrons and neutral particles is high, and is a major source of high frequency radio absorption at high latitudes. A model describing this auroral absorption has been developed and published separately (Elkins, 1972).*

Article 4 (Chapter 4) by J. Klobuchar, presents a model of the total integrated electron content in part of the polar ionosphere. The total electron content is measured by the Faraday (polarization rotation) technique, using geostationary satellite transmissions in the VHF band. This is a unique technique, completely independent of all others used to develop the model. It therefore serves as a useful check on other aspects of the overall model, while itself being a valuable contribution for certain radio propagation uses (for example, radar group path delay).

In a related study, Gassmann (1973)** has examined the complex spatial and temporal interrelationships between many different phenomena. A major step forward in understanding the polar ionosphere was the realization that the Feldstein auroral oval concept, previously discovered in the course of optical studies of the aurora, could also be used as an ordering device for ionospheric plasma properties with certain modifications. These concepts, as treated in Gassmann's paper are useful in cases where it is necessary to modify instantaneous ionospheric models, on a real-time basis, according to some measured ionospheric property.

---

* Elkins, T.J. (1972) AFCRL Report TR-72-0413, 18 July 1972.

** Gassmann, G.J. (1973), AFCRL Report, TR-73-0151, May 1963.

Contents

Symbols

ϕ	Geographic latitude (deg)
λ	Geographic longitude (deg)
Φ	Corrected geomagnetic latitude (deg)
H_L	Local solar time (hr)
H_M	Corrected geomagnetic time (hr)
z	Vertical coordinate (km)
g	Acceleration of gravity (cm sec^{-2})
χ	Solar zenith angle
δ	Solar declination
H	Scale height (km)
T	Absolute temperature (^oK)
k	Boltzmann's constant
m	Mean molecular weight (grams)
D	Day number in the year
K_p	Planetary magnetic index (quasilogarithmic)
a_p	Planetary magnetic index (arithmetic)
N	Electron density (cm^{-3})
F	Average daily solar flux
$\bar{F}$	Solar flux averaged over three solar rotations
F_c	Composite solar flux ($F_c = 2\bar{F}/3 + F/3$)
R	Zurich sunspot number
f_oF_2	Critical frequency of the F_2-layer

Symbols

f_oF_1	Critical frequency of the F_1-layer
f_oE	Critical frequency of the E-layer
f_oE_s	Critical frequency of the sporadic-E layer
h_{max}	Height of the F-layer maximum density
TEC	Total electron content
$(TEC)_B$	Total electron content of the lower side of the ionosphere
S_B	Bottomside slab thickness
S_T	Topside slab thickness
Å	Angstrom unit

Contents

AN EMPIRICAL MODEL OF THE POLAR IONOSPHERE

1. A Statistical Predictive Model of the Polar Ionosphere

T.J. Elkins and C.M. Rush
Ionospheric Physics Laboratory
Air Force Cambridge Research Laboratories
Bedford, Massachusetts

1-1. PHYSICAL PROPERTIES OF THE POLAR IONOSPHERE

1-1.1 Basic Magnetospheric and Plasmaspheric Processes

It is necessary to define the words "polar" and "high latitude" as used in the context of this model, since they have fairly precise meanings which are somewhat different from their conventional interpretations. From the ionospheric point of view, the boundary between the high latitude and midlatitude ionospheres may be defined as the ionospheric projection of the plasmapause. The plasmapause is the name given to a distinctive feature of the earth's plasma environment forming the boundary between plasma which corotates with the earth, and plasma which is strongly influenced by interaction with the solar wind. The plasmapause contains the "plasmasphere", which is a sphere only in a topological sense. Figure 1-1 shows a meridional cross section through the earth's magnetosphere, with the different plasma regimes illustrated schematically, but roughly to scale. The solar wind is an outflow of charged particles—mainly protons and electrons—from the solar corona, having sufficient number density and remnant magnetic field to behave substantially as a fluid. Its velocity is highly supersonic, so that

(Received for publication 23 May 1973

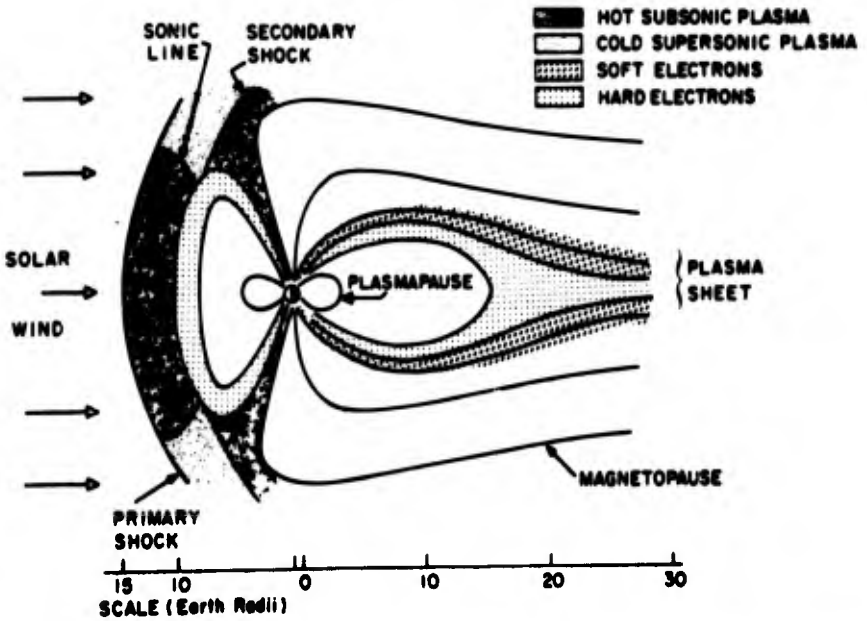

Figure 1-1. Noon-Midnight Cross Section of the Magnetosphere, Illustrating Regions of Different Plasma Properties

when it encounters an obstacle (the earth) in its path, a standing shock is supported at about 15 earth radii on the bow side. The plasma passing through this shock is initially subsonic and adiabatically heated, but it subsequently accelerates and again becomes supersonic, cooling in the process. At a certain depth into the magnetosphere, roughly at 10 earth radii geocentric distance, the plasma kinetic-energy density becomes equal to the magnetic energy density. Because of the high conductivity of the solar wind plasma, the magnetic field lines at greater geocentric distance than this are swept back with the flow, forming the geomagnetic tail. The "last" unbroken field line and the "first" swept back field line form the "magnetopause" or boundary of the magnetosphere. Direct access of solar wind plasma into the region interior to the magnetopause is impossible, except at the boundary between closed and open field lines. Here, at a topological discontinuity in the earth's magnetic field known as the magnetospheric "neutral point" or, more accurately, as the "cleft", solar wind plasma may penetrate to the earth's atmosphere. The discontinuity of the magnetic field at the cleft creates another obstacle to the redirected flow behind the standing bow shock, and a weak secondary shock is formed before the solar wind plasma again accelerates and proceeds along the magnetic tail. The plasma which enters the magnetosphere—mainly, if not wholly, through the cleft region—is redistributed in a complex flow regime which tends to be concentrated near the equatorial cross section of the tail known as the "plasma

sheet". This plasma is strongly influenced by electrodynamic interaction with the solar wind flow, as illustrated in Figure 1-2, while the plasma contained within the plasmapause is relatively unaffected by the solar wind.

Figure 1-2 shows an equatorial cross section of the magnetosphere, with streamlines of plasma convection drawn schematically. The plasma within the plasmasphere is shown to be essentially corotating with the earth. In a frame of reference fixed with respect to the sun, this corotational flow, in the presence of the earth's magnetic field, establishes a Lorentz electrostatic field directed radially outwards from the earth. In the same frame of reference, the solar wind flow along the magnetospheric tail establishes an electrostatic field across the tail, directed from East to West. This cross-tail electric field is responsible for the plasma flow pattern within the tail. Near the plasmapause boundary, the plasma is influenced by the combination of both electric fields, and the flow is complex. Note the considerable shear flow on the evening side of the earth, where the flow direction reverses over a relatively small distance. Exchange of plasma between the plasmasphere and the plasma sheet is possible in this region, and may occur especially during magnetically disturbed periods.

Figure 1-3 shows a three-dimensional view of the magnetosphere, adapted from Walters (1966). The two-dimensional nature of the cleft is clearly seen, and recognized as the demarcation between corotating and polar field lines. (Magnetic field lines may be thought of as rotating, if the plasma with respect to which they are fixed is rotating. Since the coupling between plasma and magnetic field is not perfect, partial rotation is possible. The rate of rotation decreases from corotation at the plasmapause to zero at the magnetopause.) The resultant magnetic field at the demarcation line has a tangential component everywhere except at the North and South neutral points, where the total resultant magnetic field is zero.

Figure 1-4 shows an experimentally measured meridional-field-line configuration (Fairfield, 1968) with an equivalent dipole field configuration as a reference to show the distortion brought about by the solar wind. The distorted field lines are labeled with the geomagnetic latitude at which they intersect the earth's surface. Figure 1-5 shows similarly measured contours of the geomagnetic latitude and local time of the earth intersection points of magnetic field lines in the equatorial plane (Fairfield, 1968). Figure 1-6 (Fairfield, 1968) shows contours of constant magnetic field magnitude in the equatorial plane. Charged particles, having a certain energy and equatorial pitch angle, may completely orbit the earth in the equatorial plane so long as they are trapped on a field line having an equatorial magnitude greater than about 65 gammas. Particles trapped on lines whose contours do not close around the earth in the equatorial plane are quasitrapped, and cannot complete a single revolution around the earth. Thus, they represent a loss of magnetospheric plasma to the solar wind flow, and a means whereby the steady state of flow between the solar wind and the magnetosphere is preserved. Figure 1-7

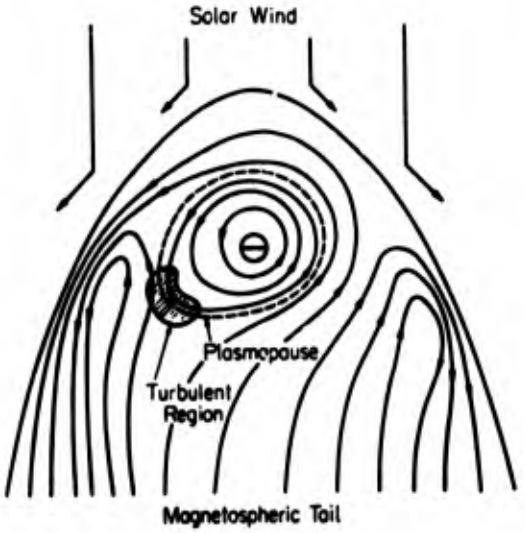

Figure 1-2. Equatorial Cross-Section of the Magnetosphere Showing Plasma Convection Pattern

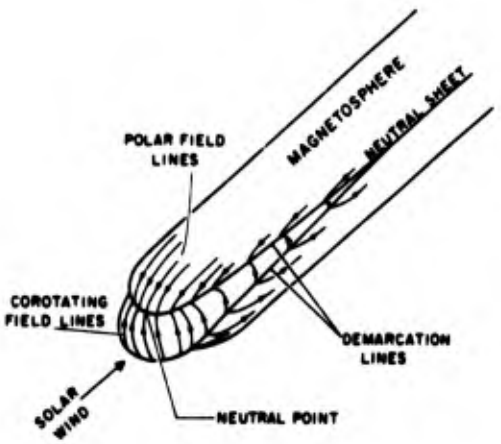

Figure 1-3. View of the Magnetosphere Showing Geometry of the Magnetic Singularity (demarcation lines)

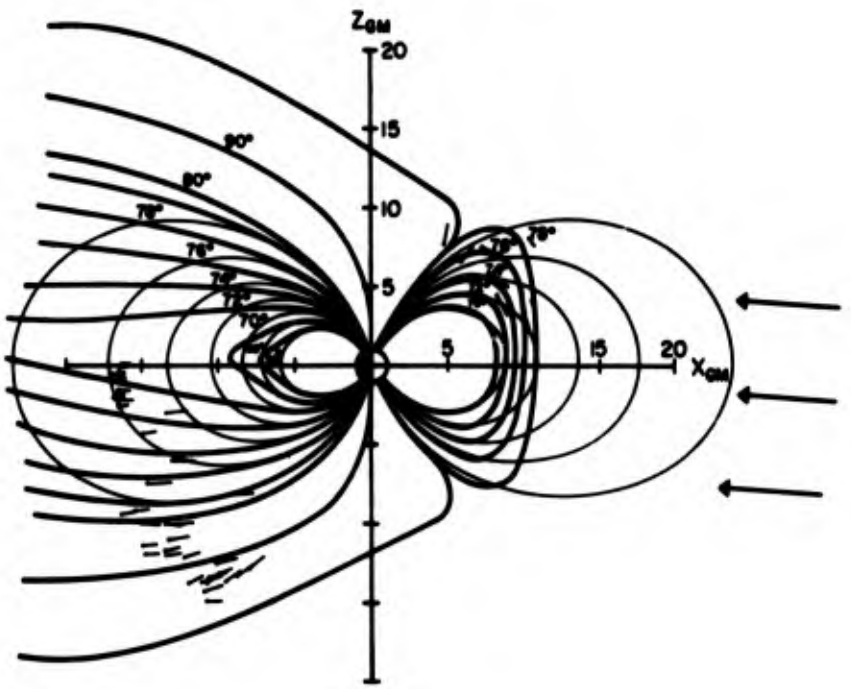

Figure 1-4. Distorted and Dipole Lines of the Noon-Midnight Meridian Plane, Labeled With Their Earth Intersection Latitudes (Fairfield, 1968)

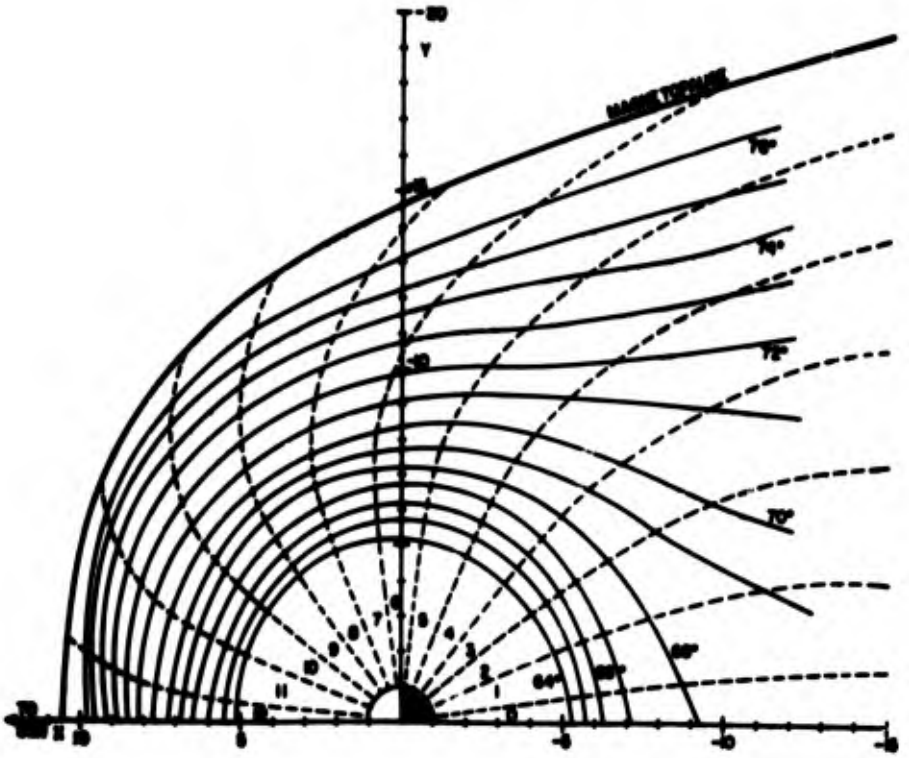

Figure 1-5. Contours in the Equatorial Plane Designating the Latitude and Local Time of the Earth Intersection Point of the Field Line (Fairfield, 1968)

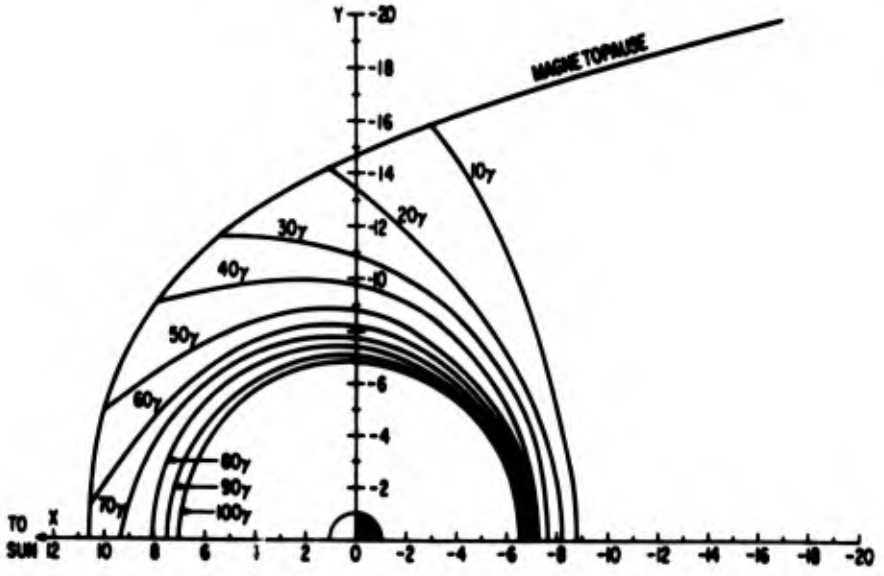

Figure 1-6. Contours of Constant Field Magnitude in the Equatorial Plane (Fairfield, 1968)

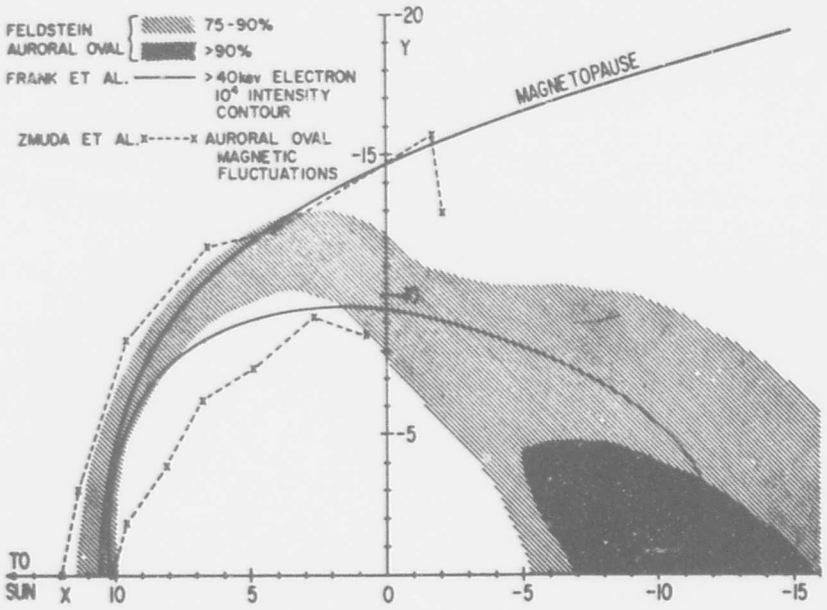

Figure 1-7. Auroral Oval and Associated Phenomena Projected Along the Field Lines to the Equatorial Plane (Fairfield, 1968)

(Fairfield, 1968) shows several measured phenomena mapped along geomagnetic field lines to the equatorial plane, using the information of Figure 1-5. The Feldstein auroral oval is derived from ground based optical measurements of auroral emission, with the different contours representing the percentage occurrence of visible aurora in the maximum phase of the solar cycle. Also shown are the mappings of energetic auroral electrons measured by satellite-borne instruments and of rapid fluctuations of the geomagnetic field associated with the auroral region. All of these phenomena, and especially (in the context of the model) the auroral oval itself, are seen to associate with quasitrapped magnetospheric particles.

1-1.2 Neutral Atmosphere

Since the ionosphere is derived from the neutral atmosphere and—in terms of ionization density—is a small fraction of the neutral density, it is appropriate to begin by noting some of the major properties of the neutral atmosphere at ionospheric altitudes, and their implications with respect to ionospheric morphology.

The variations in temperature, density, and chemical composition of the neutral atmosphere are all directly or indirectly caused by variations in solar

activity. The principal source of heat input is the absorption of solar UV radiation in the process of dissociating molecular oxygen, giving rise to the Shumann-Runge continuum absorption spectrum. The temperature of the upper atmosphere is thus strongly correlated with the rate of emission of solar UV, which originates mainly from plage regions on the solar disc. This UV emission is known to be extremely erratic and, as a consequence, the atmospheric temperature and particularly the atomic oxygen concentration is also highly erratic. It will be remarked subsequently that the atomic oxygen species is the principal source of electrons constituting the ionospheric F-region, so that this variability is very significant. Underlying this highly variable component of solar UV, however, is a steadily varying component which exhibits a considerable correlation with gross indicators of solar activity, such as the Zurich Sunspot Number and the 10.7-cm radio flux. This correlation of a parameter not readily measurable (solar UV) with another that is readily measurable (sunspot number or 10.7-cm flux), offers a convenient means of measuring and predicting exospheric properties.

In addition to global heating of the neutral atmosphere by UV absorption, solar activity may cause the atmosphere to be heated in localized regions through other processes. The principal additional sources of solar energy input are:

(1) Joule heating by ionospheric current systems, which ultimately derive from solar wind-magnetosphere interaction, and are strongly enhanced in the polar regions.

(2) Direct heat input from the solar wind to the ionosphere via the neutral points (singularities) of the magnetosphere on the dayside of the earth at high latitudes.

The exospheric temperature and pressure undergo regular temporal variations, of which the most pronounced is the diurnal variation due to the earth's rotation. The diurnal minimum temperature occurs at about 2-to 3-hr local time and may be expressed as (Chandra and Krishnamurthy, 1968):

$$(T_n)_{min} = 524 + 2.73\,\bar{S}_{10.7} + 1.77\,(\Sigma K_p - \overline{\Sigma K_p}) \quad (^{o}K) \tag{1-1}$$

where $\bar{S}_{10.7}$ is the slowly varying component of solar flux at 10.7-cm wavelength (in standard flux units), ΣK_p is the sum of eight daily 3-hr planetary magnetic indices, and $\overline{\Sigma K_p}$ is the average of ΣK_p over five consecutive days. The last term in Eq. (1-1) expresses short term variations due to varying magnetic activity on a global scale. Actually, the temperature and density fluctuations due to varying magnetic activity are greatest at high latitudes, and it is probable that better indices of magnetic activity are available to describe them (for example, the auroral electrojet index (AE)).

There are also annual and semiannual variations in exospheric temperature and density, the latter considerably exceeding the former in magnitude. The exospheric temperature maximizes in April and October, thus exhibiting a phase lag with respect to the equinoxes. The semiannual variation in the neutral atmosphere is the source of an important, and for a long time puzzling, semiannual variation in ionospheric F-region density. Variations in neutral atmosphere properties with a scale longer than 1 year are related to the 11-year solar cycle and to secular trends in solar activity.

Convection of the neutral atmosphere (winds) is another factor which has an appreciable effect upon the ionosphere. Such winds affect the distribution of ionization through the viscous drag-like force which neutral atoms and molecules exert on ions. Conversely, if the ions are driven by, say, an electric field, they can cause the neutral species to move through the same "ion drag" force. Neutral winds are driven by pressure gradients established principally by solar UV heating and by tidal motions of the atmosphere in response to solar heating and, to a lesser extent, solar and lunar gravitational attraction. The effect of neutral winds on ionization distribution, however, is complicated by the geometry of the magnetic field. Since ions can only move freely in the direction of the magnetic field vector, the response of the ions to a neutral convective motion is highly anisotropic. Thus, as the dominant neutral wind vector rotates diurnally, the vertical component of motion at any given location varies in such a way as to maximize when the wind direction coincides with the local magnetic declination. This effect gives rise to appreciable longitudinal effects in F-region electron density.

The vertical distribution of the various neutral constituents is a dominating factor in determining the properties of the upper ionosphere. Below a certain level ($\sim$ 120 to 150 km) the atmosphere is uniformly mixed by convection and turbulence, and its composition is close to that at sea level. Above this level (the "turbopause"), the various constituents are each independently in diffusive equilibrium under the influence of gravity. The altitude variation of a given constituent is a function of its molecular mass, the exospheric temperature, and the vertical temperature gradient. As one proceeds upwards from the turbopause, the mean molecular weight steadily decreases. The principal constituent at F-region altitudes is atomic oxygen, but at about 700 km (depending on the phase of the solar cycle) the principal constituent becomes helium and ultimately, at great altitude, hydrogen predominates. At high geomagnetic latitudes, this simple picture of diffusive equilibrium is complicated by a large scale upwards convective force, related to the geometry of the magnetosphere, known as the "polar wind". The polar wind acts in such a way as to reduce the light ion concentration over the polar regions, with the result that the transition from heavy to light ions takes place at a greater altitude there than at low latitudes. This has important consequences in determining the structure of the topside ionosphere.

1-1.2.1 RELATIONSHIP BETWEEN SUNSPOT NUMBER AND SOLAR FLUX

As noted earlier, the Zurich sunspot number (R) and the 10.7-cm solar flux (F) are used as approximate but convenient estimators of the solar eUV and soft X-ray flux, which heats and ionizes the neutral atmosphere. Some of the analysis that follows has been performed using R as a variable, and some using F as a variable. The reasons for this are partly historical, and partly of convenience. It is necessary, however, to provide a relationship between R and F in order to maintain consistency. The relation used is taken from Rawer and Suchy (1967):

$$F = 69 + 0.38\,(R - 8)^{1.17}\,.$$

1-1.3 Solar Produced Ionosphere

The photoionization of the neutral atmosphere resulting from irradiation by solar UV and soft X-rays is the principal source of the ionosphere. Variations in the properties of the neutral atmosphere are reflected in variations in the ionosphere, while the influence of the terrestrial magnetic field upon the ionization gives rise to other morphological features which are peculiar to the ionosphere. It is customary to speak of the ionosphere in terms of discrete "layers"—the D-, E- and F-layers—even though no clear lines of demarcation actually exist.

1-1.3.1 D-REGION

The lowest ionospheric region extends from about 50 to 85 km, and is known as the D-region. The principal source of ionization is hydrogen Lyman alpha radiation and hard X-rays, which ionize nitric oxide (NO) forming NO^+. At the lowest altitudes, an appreciable proportion of the ionization is due to galactic (and occasionally solar) cosmic rays. Negative ions play a significant role in D-region ionization balance, in contrast to the higher regions, where their concentrations are insignificant. The upper D-region electron density undergoes a very pronounced diurnal variation, with rapid recombination and attachment to neutral molecules (forming negative ions) taking place after sunset.

The relatively high neutral atmospheric density at D-region altitudes results in a high electron collision frequency in this region. This has important consequences in the propagation of radio waves, since it leads to absorption or attenuation of the waves. Another consequence of the high neutral density is the manifestation of neutral atmosphere circulation patterns in the ionization distribution of the D-region. A source of abnormal D-region ionization is X-radiation emitted from the solar chromosphere in the vicinity of a flare. Such events—known as sudden ionospheric disturbances (SID)—are relatively infrequent and short lived, but cover the whole sunlit ionosphere. Other, nonsolar, effects are

produced by energetic particle fluxes in the polar ionosphere and will be discussed separately.

1-1.3.2 E-REGION

The E-region spans the altitude range approximately 85 to 140 km. Photoionization occurring in this region is caused by soft X-rays of solar origin. The principal ionic species in the E-region are O_2^+ and NO^+, with the concentration of the latter exceeding that of the former by a factor of 3 or more. The electron concentration in the E-region exhibits a maximum value of about 10^5 cm^{-3} near noon and also displays a pronounced seasonal variation. The electron concentration (N) depends upon solar zenith angle (χ) according to a law of the form

$$N \sim (\cos \chi)^n$$

where n is typically in the range 0.6 to 0.8, depending on factors such as season and latitude.

Sporadic-E is a commonly occurring E-region perturbation which, at mid-latitudes and often at high latitudes, takes the form of a thin layer of enhanced, patchy ionization. Sporadic-E layers may be partially transparent to incident radio waves and often have steep vertical electron density gradients associated with them. At high latitudes, sporadic-E is often associated with the aurora and energetic particle streams, and in these cases it may not be correct to speak of a "layer" at all, but rather of a sporadic-E region, which has considerable vertical extent.

1-1.3.3 F-REGION

The F-region extends from about 140 km out to about 1000 to 2000 km, where the protonosphere may be defined to begin. Soft X-rays in the 200 to 900 Å range ionize the atmosphere in this altitude range, and the principal ions are NO^+ and O_2^+ near the lower boundary, gradually giving way to O^+ at greater altitudes, with small concentrations of N^+. A transition to lighter ions He^+ and H^+ takes place at the top of the F-region.

Because of the great difference in recombination rates of monotonic and diatomic ions, the lower F-region (known as the F_1-region) behaves very differently from the upper (F_2) region. At altitudes below ~ 200 km, in the F_1-region where NO^+ and O_2^+ predominate, the recombination rate is $\sim 10^{-7}$ $cm^3 sec^{-1}$, and the ionization density follows a solar zenith angle dependence similar to that of the E-region. At greater altitudes (F_2-region) where monochromatic species predominate, recombination proceeds much more slowly, with a representative value for the recombination rate being $\sim 10^{-10}$ $cm^3 sec^{-1}$. The electron density in the

F_2-region is determined principally by diffusion and convection, rather than by photochemistry.

1-1.4 Particle Produced Ionosphere

Charged particles, principally electrons and protons, travel from the sun to the vicinity of the earth in a plasma flow regime known as the "solar wind". Since the earth possesses a strong (astrophysically speaking) magnetic field, complex interaction processes take place between these charged particles and the quasi-thermal plasma which surrounds the earth. In order to understand the mechanism of particle injection into the ionosphere, it is first necessary to appreciate magnetospheric processes. Recent progress in this field has been rapid, but several key problems remain unsolved, notably the identification of the process responsible for local acceleration of charged particles in the magnetosphere.

Solar wind particles have direct access to the magnetosphere and ionosphere through the neutral points of the magnetosheath. Actually these are not "points" at all but two-dimensional surfaces defined by a mathematical singularity in the topology of the magnetosheath, which is brought about by the viscous-like interaction between solar wind plasma and the cooler magnetospheric plasma contained within the earth's magnetic field. The energy spectrum of charged particles observed at all altitudes in this singular region (also known as the magnestospheric "cleft") is characteristic of the solar wind, with energies in the tens to hundreds of eV range carrying the bulk of the energy. Particles in this energy range deposit their energy mainly above the peak of the F-region, resulting in excess ionization on the topside ionosphere and an enhanced vertical temperature gradient. The ionospheric projection of the cleft is a crescent shaped area on the sunward side of the earth, extending from roughly the 0600 meridian around to the 1800 meridian. Although its latitudinal extent is, topologically speaking, only about 1/2 degree, various physical processes combine to increase this extent to several degrees, in terms of observable ionospheric effects.

On the nightside of the earth, very complex particle deposition effects are observed at high latitudes. Due to the optical emissions from atoms excited by energetic particle collisions, these regions of particle precipitation were first studied by optical techniques. These studies eventually enabled a major advance in knowledge to be achieved with the discovery of the "auroral oval" by Feldstein. This oval shaped region roughly coincides with the ionospheric projection of the boundary between open and closed field lines in the magnetosphere, and remains fixed with respect to the sun, while the earth rotates under it. Because of the angle between the earth's magnetic and spin axes, this results in a rather complex variation of particle precipitation from the magnetosphere, when viewed from any single location on the earth's surface. The auroral oval concept, however, has

allowed order to be achieved in describing many diverse observations and its validity may be extended, with certain limitations, well beyond its original intent—that of describing optical emissions.

Energetic particle precipitation takes place around the auroral oval in a fairly well defined manner, although there are many localized irregularities and exceptions. The basic mechanism of particle injection is the auroral substorm, which is actually the ionospheric manifestation of a complex sequence of events involving the entire magnetosphere. Auroral substorms, accompanied by particle precipitation, usually begin in the midnight sector of the auroral oval, and then propagate around towards the morning and noon sectors. The energy of the precipitated particles is typically in the range from several keV to tens of keV, and particles with these energies are stopped by collisions with neutrals at D- and E-region altitudes. The effects upon ionization distribution in the ionosphere are extremely complex, and have not yet been completely understood. Among the most obvious, however, are the production of an intensely concentrated D-region and the presence of abnormal ionization in the E-region. Substorms also release a great deal of heat at ionospheric heights, principally due to Joule heating by the intense current systems which accompany them. This heating of the thermosphere, localized around the auroral zone, has a profound influence upon the distribution of neutral and ionized species alike, especially in the topside ionosphere.

Within the polar cap, the magnetic field lines do not terminate in the conjugate hemisphere, and are said to be "disconnected". The physical processes which govern energetic particle precipitation into this region are even more poorly understood than for the auroral region. Nevertheless a great deal of particle precipitation is observed to take place within the polar cap, most of it at relatively low energy (tens to hundreds of eV) and very erratic in space and time, giving rise principally to ionization in the F-region and above. At rare intervals—perhaps two to three times per year on the average—solar protons in the tens of MeV energy range precipitate into the polar cap ionosphere, where they produce remarkably high levels of ionization in the D-region. These "solar proton" events have been studied at great length, but the polar cap ionosphere, for the most part, remains a region of considerable mystery.

1-1.5 Special Features of the High Latitude Ionosphere

1-1.5.1 TROUGH

The high latitude trough is a complex feature whose location coincides roughly with the ionospheric projection of the plasmapause. Although the physical processes which operate to produce the trough are not fully understood, it is probably due to a combination of the effects of the polar wind, auroral particle

precipitation, and thermal conduction from the magnetosphere. The trough is principally a topside feature, where it appears to be formed by the combined effects of an outflow of light ions in the polar wind, and an ionization enhancement associated with particle precipitation around the auroral oval. It is frequently observed that the electron density decreases sharply across the plasmapause projection, from low to high latitudes, and remains at a low level all the way to the magnetic pole. In these cases, a "trough" in the strict sense, cannot be said to be formed, although at least one of the relevant physical processes is operative.

Another common observation, especially near solar minimum, is that the trough extends downwards from the topside to the F-peak and below. Some mechanism other than the polar wind must be operating to produce this effect, since the light ion concentration at these altitudes is negligible. A possible cause of these observed extensions down through the F-layer maximum is a reduction of the downward diffusion flux, which normally maintains the ionization density near the peak, brought about by heat conduction from the magnetosphere. The frequent observation of SAR arcs in this geographical region indicates the presence of ions with temperatures in excess of 4000 ^{o}K. Such high temperatures would certainly increase the linear loss coefficient. Thus the combination of decreased diffusion and enhanced loss would cause the height of the layer to increase and its maximum density to decrease, in the region of excess heating. This is what is observed in practice, although this agreement should not necessarily be taken as confirmation of the mechanism suggested here.

The problem of modeling the trough region of the ionosphere is complicated by the effects of magnetic activity, which not only cause the relative importances of the several operative physical processes to vary, but also alter the geographical location and extent of the trough. There appear to be strong longitudinal influences involved, so that no true magnetic time frame can be established, although this can be done approximately if the application permits. All phenomenological aspects of the trough (position, depth, etc.) are random variables, although certain deterministic features apparently exist. The presence of the trough near the F-peak may have a significant dependence on the phase of the solar cycle. The data from ground based ionosondes during IGY do not show strong evidence of the trough. Even allowing for possible misinterpretation of ionograms before the discovery of the trough in 1965, the result cannot be explained reasonably. Certainly, the trough is clearly in evidence in ground based ionosonde data in 1964. However, it is not well established how the pertinent solar-geophysical processes involved in trough formation vary throughout the solar cycle. Indeed, there is some evidence that solar wind pressure decreases with increasing sunspot number, which would suggest that the plasmapause actually grows towards solar maximum. The location and intensity of the auroral zone precipitation do not show a simple correlation

with sunspot number, so that it is quite possible that, in 1958 (IGY), the trough was very narrow or mostly nonexistent, at least in its conventionally observed form. That it was, at least occasionally, present in the Southern Hemisphere during IGY was shown by Bowman (1967).

1-1.5.2 DAYSIDE CLEFT REGION

The ionosphere at the projection of the magnetospheric cleft differs remarkably from the ionosphere elsewhere in the polar region. The solar wind particles, which find their way down the cleft, have energies in the range of hundreds of eV and lower. These particles lose their energy in ionizing collisions at F-region heights and above. In summertime, a clearly delineated particle-produced layer can often be discerned, embedded within the solar EUV-produced ionosphere. This layer, which exists in isolation in winter, is very irregular and is situated, for the most part, above the normal solar F-layer peak, sporadically penetrating below the peak as the solar wind fluctuates. The plasma temperature in the solar wind is several thousand degrees Kelvin, so that a large vertical temperature gradient exists in the cleft region, and heat is continually being conducted downwards. The topside scale height is substantially greater than in the adjacent ionospheric regions and the shape of the vertical profile is correspondingly different.

The cleft region extends roughly from the dawn to the dusk meridians, and its latitudinal extent is typically 2 to 4 degrees. There is some indication of a diurnal dependence of this latitudinal extent as well as a dependence upon interplanetary magnetic conditions, but this must be substantiated by further observations. The location of this region has a rather well defined dependence upon geomagnetic activity, when viewed in geomagnetic coordinates. The cleft moves towards the magnetic equator as magnetic activity increases, in response to increased pressure of the solar wind on the sunward side of the magnetosphere.

1-1.5.3 POLAR CAVITY

In winter, when the sun is well below the horizon at high latitudes, a noticeable but irregularly shaped depression in the ionosphere is observed, centered roughly over the magnetic pole. This is sometimes referred to as the "polar cavity". This feature appears to be caused by the outflow of light ions in the polar wind, causing a general reduction in the ionization level at all altitudes. Under sunlit conditions, the ion production rate is sufficient to compensate for this loss, but in winter the convective motions which transfer ions laterally cannot make up for this vertical loss. Sporadic particle precipitation events are observed in the polar cavity region, and the plasma is normally in a highly irregular state.

1-1.5.4 NIGHTSIDE AURORAL OVAL

The nightside auroral oval region is highly complex, and virtually never in equilibrium. Intense fluxes of energetic particles are continually being injected from the geomagnetic tail, which produce large quantities of ionization in the E-region and above. Intense electric fields and neutral winds are observed, which contribute strongly to the ionization distribution. One feature, which seems to occur fairly regularly, is a concentration of F-region ionization along the equatorward edge of the auroral oval. The F-region within the oval itself is highly irregular, and is often observed to disappear almost completely. A predictive model for this region has little meaning, except in a purely statistical sense, since equilibrium must exist only very rarely. Figure 1-8, taken from a paper by Craven (1970), illustrates the spatial distribution of precipated auroral electrons (with energy greater than 5 keV). The peak fluxes occur at 0 to 3 magnetic time at about 65° geomagnetic latitude, and the precipitation region is sharply bounded at both high and low latitudes.

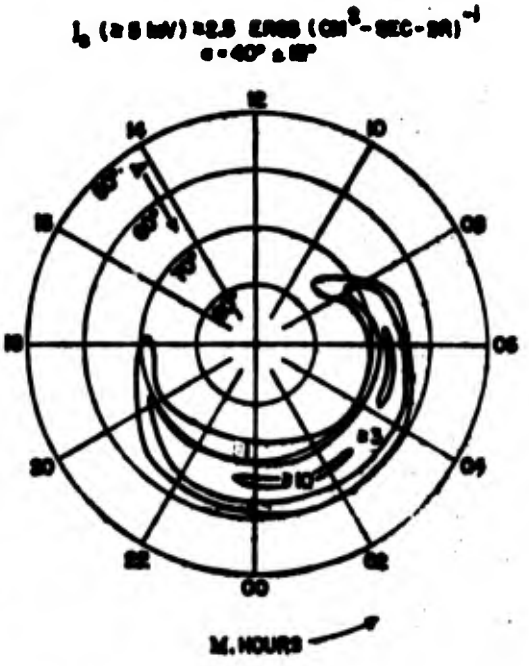

Figure 1-8. Contours of Electron Precipitation in Magnetic Coordinates; Electron Energies ≥ 5 keV (Craven, 1970)

1-2. NORMAL D-REGION MODEL

The normal (quiet) D-region ionization is produced by two principal sources: (1) Cosmic rays, at altitudes below 65 km, and (2) solar X-rays in the wavelength range 2 ~ 8 Å, and Hydrogen Lyman alpha radiation, in the height interval 65 to 100 km.

The cosmic ray ionization source is essentially constant in time, but is modulated by variations of interplanetary magnetic field, so that the lower D-region has a detectable solar cycle variation. Seasonal and diurnal variations in the lower D-region are very small, due to the near constancy of the neutral density there. At high latitudes, however, solar cosmic rays with energies greater than about 10 MeV produce additional ionization in this altitude region during PCA events.

Major magnetic storms which are not accompanied by solar protons may, however, have the opposite effect of reducing ionization in the lower D-region. Increased turbulence in the interplanetary magnetic field lowers the rate of diffusion of galactic cosmic rays through the interplanetary medium, so that their flux at the earth's surface is reduced—a phenomenon known as the "Forbush decrease".

The solar X-ray source is strongly dependent on solar activity and the number, size, and type of flares on the solar disc. The vertical ionization profile in this region (65 to 100 km) is significantly dependent upon solar zenith angle, season, and solar activity. In addition, the ionization in this region is sensitive to changes in the composition and temperature of the neutral atmosphere, so that meteorological influences are observed which give rise, for example, to the so-called "winter anomaly". Solar protons in the energy range $0.1 \sim 10$ MeV produce excess ionization in the upper D-region during PCA events. More frequently, the high energy tail of the auroral electron spectrum ($10 \sim 50$ keV) produces excess D-region ionization around and in the vicinity of the auroral oval.

A model of the normal D-region is assumed to represent the effects of ionization due to galactic cosmic rays (CR) and solar X-rays only, with separate models being required to include the effects of solar PCA protons and auroral particles. Such a model has been formulated by Nestorov (1972). The CR layer is represented by

$$N_1(z) = N_o \exp\left\{b_1 (z - z_o)\right\}$$

where N_o is the electron density at height z_o, and b_1 is the logarithmic height gradient. It was shown by Nestorov that, at solar maximum conditions in summer, at Sofia

$$b_1 = 0.12 \text{ km}^{-1}$$

$$N_o = 5 \text{ cm}^{-3} \text{ at } z_o = 40 \text{ km}.$$

The solar cycle variation of cosmic ray intensity (with energy less than 4 BeV) is such that the minimum value occurs at sunspot maximum. This is due to the fact that galactic cosmic rays must diffuse through the turbulent interplanetary magnetic field, which allows a lower diffusion rate when the sun is disturbed than for the quiet solar conditions. Those cosmic rays which are most effective in ionizing the D-region (the lower energy ones) find easiest access to the atmosphere at high geomagnetic latitudes, so there is a pronounced latitude effect superimposed on the solar cycle modulation. Above about 60^o geomagnetic

latitude, however, the incident primary cosmic ray intensity may be regarded as essentially constant (Lingenfelter, 1963).

As an approximate measure of the magnitude of the solar cycle modulation, the results of A.N. Charakhchyan and T.N. Charakhchyan (1967) may be used. They found that the cosmic ray intensity was approximately proportional to the logarithm of sunspot number. At high latitudes (above 60° geomagnetic), their results would imply a relationship like

$$N_c = 3.2 - 0.8 \log R$$

for R in the range 30 to 200, where N_c is the cosmic ray flux, in arbitrary units, taken to be unity at R = 560. In the lower D-region, the principal loss process for electrons is by formation of negative ions, so that the loss rate is linear. Thus the electron density changes over a solar cycle are proportional to the CR flux. The constant N_o may therefore be expressed approximately as

$$N_o = 14 - 3.5 \log R$$

where an additional factor of 1.45 has been multiplied into the equation to adjust the value of N_o for the different geomagnetic latitudes (Sofia: 41°; model: $> 60^{\circ}$).

The upper part of the normal D-region may be represented by another exponential function of the form

$$N_2(z) = N_t \exp\left[b_2 (z - z_t)\right]$$

where N_t is the electron density at z_t = 65 km, being the upper boundary of the CR region; $N_t = 20.0855\ N_o$ and the logarithmic height gradient, b_2, is chosen so that the profile merges into the normal E-region, for solar zenith angles less than 90°. This merging with the E-region may be assumed to take place at one scale height below the E-region maximum; that is, at an altitude of $90 + 20 \log_e (\sec \chi)$ km, and at an electron density of $0.866 \times 10^4 \times (f_o E)^2$ cm^{-3}.

Thus

$$b_2 = \frac{3.0333 + \ln (f_o E)}{12.5 + 10 \ln \sec \chi} \quad \text{km}^{-1}$$

in the case where the profile is modeled up to the E-layer maximum only. When an F-layer is included, this matching condition may be modified.

1-3. MODEL OF THE E- AND F1-LAYERS

1-3.1 Critical Frequencies

Hourly values of f_oE and f_oF_1, for the months March, June, September and December, in 1958 and 1964 were analyzed for the high latitude observatories indicated in Table 1-1. The five quiet days for each month were selected initially, in order to minimize the effects of ionospheric disturbances, and to isolate the direct solar controlled component of f_oE and f_oF_1. The average hourly values of f_oE and f_oF_1 for eacı station, month and year were computed for these quiet days. The solar dependence was assumed to take the form

$$f_o(E, F_1) = A(\phi, R, M) \left\{\cos(\chi - \delta\chi)\right\}^{m(\phi, R, M)} \qquad (1\text{-}2)$$

where

ϕ = geographic latitude

R = sunspot number

M = month

χ = solar zenith angle

$\delta\chi$ = phase lag in zenith angle dependence

The variables A and m were determined by regression analysis, using the quiet day data. The functional form chosen is very sensitive to data values at large zenith angles; in particular, m was found to be more susceptible to small variations in data values for $\chi > 80^o$ than was A. For this reason, it was decided to weight the data in such a way that values at large zenith angle were deemphasized. The weighting scheme used was to ignore all data values for $\chi > 85^o$, and to perform separate regression analysis for $\chi_{min} < \chi < 80^o$ (case 1), and $\chi_{min} < \chi < 85^o$ (case 2). The values of A and m thus found were used to compute separate latitudinal dependences for each case, and these latitudinal dependences were then averaged to arrive at the final result.

The assumed latitudinal dependence was a linear one in which

$$A(M, R) = a(M, r) + b(M, r)\,\phi \qquad (1\text{-}3)$$

and

$$m(M, R) = c(M, R) + d(M, R)\,\phi\,. \qquad (1\text{-}4)$$

Table 1-1. Stations Used in Data Analysis (1958)

Station Name	ϕ	λ(east)	Φ
REYKJAVIK	64.1	338.3	66.5
FT. MONMOUTH	40.3	285.9	53.9
ST. JOHNS	47.6	307.3	58.3
FT. CHIMO	58.1	291.6	70.3
NARSSARSSUAQ	61.2	314.6	69.0
FROBISHER BAY	63.8	291.4	75.3
GODHAVN	69.2	306.5	77.6
CLYDE RIVER	70.5	291.5	81.1
THULE	76.6	291.3	86.0
ALERT	82.6	297.4	86.5
DOURBES	50.1	4.6	47.6
LINDAU	51.4	10.1	48.3
*SLOUGH	51.5	359.4	49.9
DE BILT	52.1	5.2	49.6
JULIUSRUH	54.6	246.7	62.5
INVERNESS	57.5	355.7	56.8
KJELLER	60.0	11.1	57.2
MIEDZESZYN	52.2	21.2	48.2
MOSCOW	55.5	37.3	51.0
GORKY	56.2	44.3	51.6
UPPSALA	59.8	17.6	56.4
*NURMIJARVI	60.5	24.6	56.6
LENINGRAD	60.0	30.3	55.8
*LYCKSELE	64.6	18.8	61.2
LULEA	65.6	22.1	62.0
*SODANKYLA	67.4	26.6	63.4
*KIRUNA	67.8	20.5	64.3
*MURMANSK	68.9	33.0	64.6
TROMSO	69.4	19.0	66.0
LONGYEARBYEN	78.2	15.5	74.5
*SALEKHARD	66.6	66.6	61.8
*HEISS ISLAND	80.6	58.0	71.3
*DIXON	73.5	80.4	67.9
YAKUTSK	62.0	129.8	56.4
TIXIE BAY	71.6	129.0	65.6
*PROVIDENYA	64.4	186.5	60.3
ARCTICA (NP6)	82.4	9.5	77.6
ANCHROAGE	61.2	210.1	60.8
COLLEGE	64.9	212.2	64.9
BARROW	71.3	203.2	69.7
VICTORIA	48.4	236.6	53.9
MEANOOK	54.6	246.7	62.5
YELLOWKNIFE	62.5	245.5	69.9
WASHINGTON	38.7	282.9	52.3
*OTTAWA	45.4	284.3	58.9

Table 1-1. Stations Used in Data Analysis (1958) (Contd.)

Station Name	ϕ	λ(east)	Φ
*WINNIPEG	49.9	262.6	61.1
CHURCHILL	58.8	265.8	70.3
BAKER LAKE	64.3	264.0	75.1
*RESOLUTE BAY	74.7	265.1	84.3
EUREKA	80.0	274.0	89.1
FLETCHERS ISLAND	75.9	235.7	78.0

* Indicates data also available for 1964.

1-3.2 Results

The values of a, b, c and d and the standard deviations of A and m are listed in Table 1-2, for the combinations of M and R for which data were available. (Standard deviations are divided by the monthly mean and averaged over the year).

Table 1-2.

$$(foE: f_oF_1) = A \cos^m \chi$$
$$A = a + b\phi$$
$$m = c + d\phi$$

Parameter	Year	Month	a	b	c	d
f_oE	58	3	4.93	-0.014	0.471	-0.0035
		6	4.50	-0.009	0.339	-0.0010
		9	5.07	-0.015	0.490	-0.0032
		12	4.50	-0.009	0.339	-0.0010
f_oE	64	3	3.83	-0.007	0.377	-0.0014
		6	3.43	-0.002	0.288	0
		9	3.83	-0.007	0.377	-0.0014
		12	3.67	-0.002	0.289	0
f_oF_1	58	All	6.25	-0.008	0.122	0.0012
f_oF_1	64	All	4.27	0	0.107	0.0008
f_oE	58	$\sigma_A = 0.052$; $\sigma_m = 0.250$				
f_oE	64	$\sigma_A = 0.065$; $\sigma_m = 0.175$				
f_oF_1	58	$\sigma_A = 0.034$; $\sigma_m = 0.321$				
f_oF_1	64	$\sigma_A = 0.014$; $\sigma_m = 0.333$				

It is clear that:

(1) The standard deviations are larger at sunspot maximum (1958) than at sunspot minimum (1964)

(2) The uncertainty in the determination of m is substantially greater than that for A .

(3) Latitudinal gradients are relatively small, as judged by comparison with the standard deviations.

(4) There is a strong sunspot dependence, but a weaker seasonal dependence.

It should be noted that the relatively large residual spread in the value of m is not as severe a problem as it might seem. The computed value of the critical frequency is quite insensitive to the computed spread in m for several hours on either side of noon (f_oE typically differs by less than 0.1 MHz between $(m + \sigma_m)$ and $(m - \sigma_m)$). Only at large zenith angles (approaching 80^o) does the difference begin to be significant. Another point to be noted is that the method of analysis, which was used, did not permit any possible correlations between the residuals of each parameter to be determined. The statistical distributions of each of the parameters must tentatively be assumed to be independent.

Although the original functional dependence assumed contained a possible lag ($\delta\chi$), it was found that the inclusion of this term did not improve the accuracy of the fit for f_oE. In the case of f_oF_1, an average time lag of 12 min gave the best fit. The manner in which this lag was included was to locate the local time at which the critical frequency maximized, and then to compute the difference in solar zenith angles between this time and local noon, calling this difference $\delta\chi$. It should be remarked that in all of this parameter estimation, true local time was used rather than the time on the standard meridian, in which the data are tabulated. Ignoring this correction from standard to true local time was found to increase the residuals significantly. In an attempt to further reduce the residuals, the geographic latitude in Eq. (1-2) was replaced by corrected geomagnetic latitude. The residuals, however, were insignificantly affected by this procedure.

1-3.3 Sunspot Number Dependence

Although values of the parameters at the two extremes of a solar cycle would by themselves be insufficient to determine any sunspot number dependence, it is possible to use the results of other studies to supplement the present findings. Unpublished work of Knecht, reproduced in Davies' (1965) book, shows that the noon values of f_oE and f_oF_1 over two solar cycles followed a closely linear law, which, upon examination, was found to be

$$(f_oE)_{noon} = 2.95 + 0.0045\,R \qquad (1\text{-}5)$$

$$(f_oF_1)_{noon} = 4.00 + 0.0087\ R\ . \qquad (1\text{-}6)$$

By assuming a similar linear dependence for the high latitude data (at a latitude of 65°), the following relations were derived for summer:

$$\text{E-layer:} \quad A_{o(M=6)} = A_{o(M=6,\,R=o)} + 0.0041\ R$$

$$F_1\text{-layer:} \quad A_{o(M=6)} = A_{o(M=6,\,R=o)} + 0.0095\ R\ .$$

The dependences thus found agree quite well with the results of Knecht (to within 10 percent). When the E region data were averaged over summer and the two equinoxes, with winter being omitted because of an anomalously low value, the result

$$A_o = A_{o_{(R=0)}} + 0.0043\ R \qquad (1\text{-}7)$$

was obtained.

1-3.4 First Order Corrections to the Models

As already noted, a small time lag (relaxation) was needed in order to bring the simple cosine (solar zenith angle) dependence into better agreement with the data, at least in the case of the F_1-layer. It was noted, however, that both f_oE and f_oF_1 exhibit a small residual asymmetry about local noon (hysteresis), as depicted in Figure 1-9. This hysteresis was adequately taken into account by the inclusion of a term linear in local time, with the coefficients for both layers being determined by regression analysis.

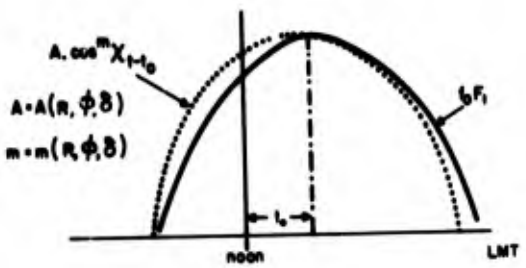

$$f_oF_1 = A\cos^m\chi_{t-t_o}\left\{1-0.005(12-T)-0.0011\,\alpha_p\right\}$$

$$f_oE = B\cos^n\chi\left\{1-0.0038(12-T)-0.00013\,\alpha_p\right\}$$

Figure 1-9. Model of f_oF_1 and f_oE

Following the hysteresis correction, the modeled value for f_oE and f_oF_1 was generated, corresponding to every available hourly data value. There were, in all, 19,967 f_oF_1 values and 30,925 f_oE values available. A set of normalized residuals was then constructed by subtracting the modeled value from the measured value in the following manner:

$$\Delta N = \frac{N-N_m}{N} \qquad (1\text{-}8)$$

where

$$N = (f_oE)^2 \text{ or } (f_oF_1)^2$$

$$N_m = (f_oE)^2_m \text{ or } (f_oF_1)^2_m \ .$$

Each of these residuals was then associated with an index of magnetic activity recorded at the time the measurement was made. The magnetic indices used were:

K_p (3 hourly planetary index)

a_p (3 hourly arithmetic planetary index)

AE (1 hourly auroral electrojet index)

D_{st} (1 hourly storm index).

Regression analyses were then performed using each magnetic index separately. It was found that a_p, AE, and D_{st} were about equally effective in terms of standard deviation from the mean. This was true both when all data were combined in a single large group, and when a subdivision was made into 10^o strips of geomagnetic latitude. A more detailed analysis showed that the linear correlation was valid only for low to moderate magnetic activity, but "saturated" at high levels of magnetic activity.

Figure 1-10 shows the dependence of the normalized residual on a_p. This dependence was approximated by a simple linear expression, however, which was then used as another first order term in the basic solar model. The complete solar model, including the magnetic activity correction, is summarized in Section 1-3.6 and in Figure 1-9. The analysis was completed by examining the statistical distribution of deviations from the resultant first order model. These were found to be closely Gaussian distributed, with a standard deviation of 2 to 3 times the nominal measurement accuracy. Considering the effects of localized disturbances (such as TID), this indicates that the modeling accuracy is approaching a practical limit.

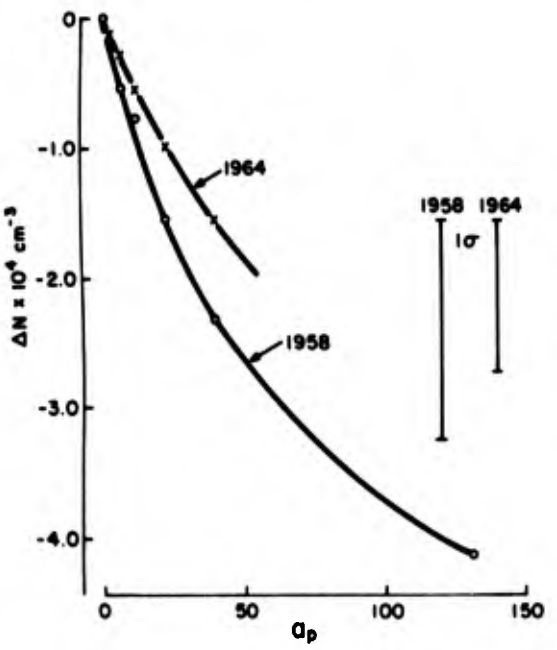

Figure 1-10. Average Depression of F_1-Layer Ionization Density Versus Planetary Magnetic Index (June 1958, 1964)

1-3.5 Auroral E-layer

In addition to the solar E-layer, it has been realized in recent years that a stable E-layer is produced, by auroral particle ionization, around the auroral oval. This layer resembles the solar E-layer in many respects, but is considerably weaker and occurs on both day and nightsides of the earth. It is differentiated from sporadic-E by exhibiting pronounced retardation (indicating that it is a thick layer) and by varying much more slowly in time and space. Nevertheless, the parameters of the auroral-E layer are random variables, since the intensity and height of the layer depend on the incident auroral particle flux and energy spectrum, which are highly variable and largely unpredictable. The critical frequency of the auroral E-layer (f_oE_a) was modeled mainly on the basis of aircraft ionosonde observations (Wagner, 1973), together with a limited amount of published data (King, 1965). The critical frequency f_oE_a is found to be approximately normally distributed with a median value of 1.1 MHz and standard deviation of 0.7 MHz. The height of the auroral E-layer ($h'E_a$) is given by the following approximate relationship:

$$h'E_a = 200 - 45 \log_{10}(f_oE_a)^4 . \qquad (1\text{-}9)$$

A special problem arises on the dayside of the auroral oval, when the combined effects of particle precipitation and solar eUV produce a composite E-layer. A crude attempt was made to synthesize this composite layer by assuming it to be the combination of two parabolic layers (solar and auroral) having identical 20-km semithicknesses. This technique is not satisfactory under certain conditions, particularly when the auroral E-layer is at heights greater than about 130 km, since a deep minimum appears between the two layers. The assumption of parabolic layers is, of course, an unrealistic one although it has been found to be satisfactory in certain radio propagation applications.

An alternative solution to the problem of the combination of the solar and auroral E-layers was to examine the residuals from the solar E-layer model for data points measured in the dayside auroral oval. On the average, these residuals were 0.2 MHz, showing that the average effect of dayside aurora is to increase f_oE by this amount. A more rigorous treatment of this problem requires the modeling of actual energy inputs (particularly the energy spectrum of the auroral particles) followed by solution of the physical governing equations. This is regarded as being beyond the scope of this model.

Figure 1-11 shows the result of synthesizing f_oE over the entire polar region for the particular set of parameters indicated. The strong solar-zenith-angle control is clearly in evidence, while the auroral E-layer is observed in isolation

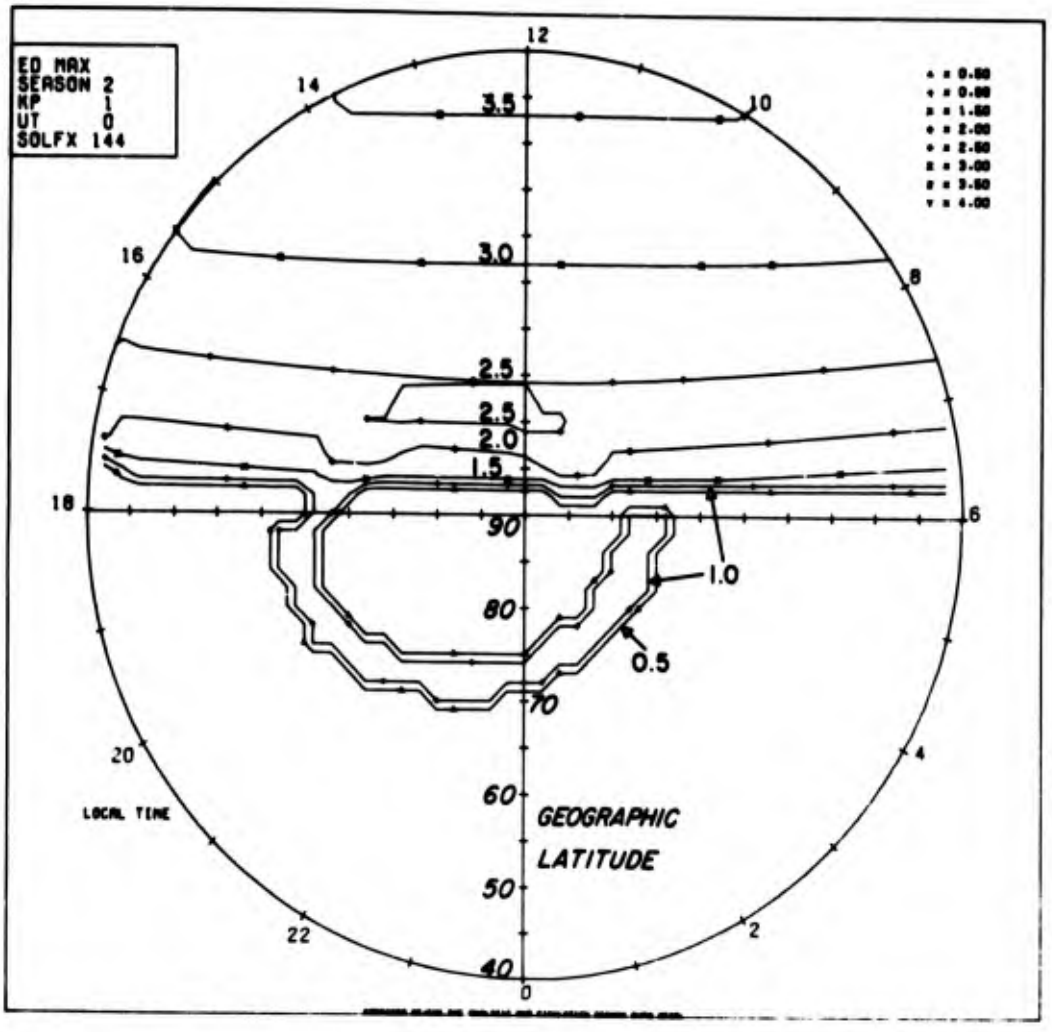

Figure 1-11. Contours of Median f_oE (MHz) for March 21; Sunspot No. 50; K_p = 1, UT = 0

on the nightside, and as a perturbation of the solar layer on the dayside. The model is a median model in the sense that the median value of the random variable (f_oE_a) is represented. The model for the solar component is essentially deterministic.

1-3.6 f_oE Solar Component

Let:

D = day number

R = sunspot number

χ = solar zenith angle

a_p = arithmetic planetary magnetic index

T = local time (hr)

ψ = $2\pi/365$ (D - 100)

ϕ = geographic latitude (deg)

Then $(f_oE)_o = A \cos^m \chi$, where:

$A = a + b\phi$

$m = c + d\phi$

$a = \alpha + \beta \cos \psi$

$b = \gamma + \delta \cos \psi$

$c = \varepsilon + \xi \cos \psi$

$d = \mu + \eta \cos \psi$

$\alpha = 3.62 + 0.00596\ R$

$\beta = 0.143 + 0.000567\ R$

$\gamma = -0.0041 - 3.90 \times 10^{-5}\ R$

$\delta = -0.00195$

$\varepsilon = 0.293 + 0.00045\ R$

$\xi = 0.01$

$\mu = -0.00062 - 0.81 \times 10^{-5}\ R$

$\eta = -0.000668 - 2.5 \times 10^{-6}\ R$

Hence:

$$f_oE = (f_oE)_o \left\{ 1 - 0.0038\ (12 - T) - 0.00013\ a_p \right\}.$$

Standard deviation of the residuals from the mean is 7.4 percent of the mean, averaged over all available data.

1-3.7 f_oF_1 Model

Let

$(f_oF_1)_o = A \cos^m \chi_{T-0.2}$, where:

$A = \alpha + \beta\phi$

$$m = \gamma + \delta \phi$$

$$\alpha = 4.13 + 0.0111\ R$$

$$\beta = 0.00057 - 0.000044\ R$$

$$\gamma = 0.106 + 0.000083\ R$$

$$\delta = 0.0007714 + 2.23 \times 10^{-6}\ R$$

Hence:

$$f_oF_1 = (f_oF_1)_o \left\{ 1 - 0.005\ (12 - T) - 0.0011\ a_p \right\}.$$

Standard deviation of the residuals from the mean is 6.3 percent of the mean, averaged over all available data.

1-3.8 Heights of E- and F1-layers

From true height analysis of polar ionograms (see Section 1-4.4), the following relationships have been deduced, based on the theoretical Chapman formulation:

$$hE = 100 + 20 \ln \sec \chi$$

$$hF_1 = 156 + 0.15\ R + 45 \ln \sec \chi$$

where the units are in km.

The scale heights in these expressions (multipliers of ln sec χ) are shown as being independent of sunspot number, R. This is certainly reasonable in the case of the E-layer, since neutral atmosphere variations at this altitude are known to be negligible. In the case of the F_1-layer, significant variations of neutral temperature and density do occur with varying sunspot number, at the altitude of hF_1. However, the indicated independence of scale height is apparently due to a much less pronounced solar cycle dependence of electron temperature, as evidenced in work by Freyzon and Shapiro (1972).

1-3.9 Total Electron Content of E- and F1-layers

Let the E- and F_1-layers be represented by alpha Chapman layers of the form

$$N(z) = N_m \exp \frac{1}{2}(1 - z - e^{-z})$$

where

$$z = \frac{h-h_{max}}{H}$$

H = scale height

h_{max} = height of maximum ionization for overhead sun.

This representation is an accurate description of the F_1-layer only up to its peak, and will be used only in this range of validity.

The integrated electron content of the Chapman layer is

$$\int_{-\infty}^{h} N(z)\, dz = \sqrt{2\pi e}\ H N_m \left\{ 1 - P(x) \right\}$$

where

$$P(x) = \frac{2}{\sqrt{\pi}} \int_0^x e^{-u^2}\, du$$

and

$$x = \frac{1}{\sqrt{2}} \exp\left(-\frac{1}{2} z \right) .$$

Thus the total electron content of the E-layer and the lower half of the F_1-layer is

$$T_B = 4.133\, H_1 N_1 + 1.312\, H_2 N_2$$

where H_1 and H_2 are scale heights of E- and F_1-layers respectively, and N_1 and N_2 are maximum electron densities of E- and F_1-layers. On substituting the expressions for $N_{1,2}$ in terms of f_oE and f_oF_1 and taking values

H_1 = 20 km

H_2 = 45 km

then

$$T_B = 7.32 \times 10^{10} (f_oF_1)^2 + 1.03 \times 10^{11} \times (f_oE)^2 .$$

1-3.10 Probability of F1-Stratification

The basic model for the F_1-layer contains only a solar zenith angle dependence, with small corrections for relaxation, hysteresis, and the effects of magnetic activity. There is, however, another important factor which remains to be included in the model. It is well known that the F_1-layer is seldom observed in winter and

virtually always present in summer, despite the fact that the solar zenith angle dependence already discussed would predict an F_1-layer in winter whenever the sun is above the horizon. This effect is apparently due to seasonal changes in the composition of the neutral atmosphere, which are associated with the seasonal ionospheric "anomaly", of which several other manifestations are well known. In particular, the seasonal variation of the linear loss coefficient at F_1-layer heights seems to be very large, and this can explain the absence of F_1-stratification in winter, at a zenith angle at which this stratification would be observed in summer or equinox.

In order to complete the model of the F_1-layer, the seasonal variation of the probability of F_1-stratification was determined from the available data. The hourly soundings—for which F_1-layer measurements were impossible because of total absorption, sporadic-E blanketing, equipment failure or interference—were first excluded from the analysis. The remaining numerical values were sorted into 5^o intervals of solar zenith angle for each station and month; that is, the number of $f_o F_1$ values in each month were counted for which the solar zenith angle was within a particular 5^o range of solar zenith angle. The stations were then grouped in 10^o intervals in geographic and geomagnetic latitude, and the results expressed as a percentage of the total possible counts. Figures 1-12 through 1-15 show these percentage probabilities for the 10^o geographic latitude intervals. In all cases the probability of F_1-formation falls to zero as the solar zenith angle approaches 90^o. However, there is a pronounced seasonal variation in the probability of formation for a fixed zenith angle, with summer values being highest and winter values lowest (almost always zero). Two other results of interest are noted:

(1) The two equinoxes are not identical—September always has higher probability of F_1-formation than March.

(2) Sunspot maximum year (1958) consistently shows a lower probability of formation than sunspot minimum year (1964).

Both of these results are in accordance with the theory of F_1-layer formation (for example, Rishbeth, 1967). The first is related to the asymmetry, with respect to the solstices, of the changeover of the atmosphere from winter to summer conditions and vice versa. These changes occur rather abruptly in April and October, respectively. Thus March is a winter-like month and September is a summer-like month. The solar cycle dependence is due to the large variations in ion-pair production rate brought about by the similarly large variations in solar eUV flux, and are explained in Rishbeth's review.

Another aspect of the probability of F_1-stratification is the diurnal dependence exhibited by this analysis; that is, the zenith angle dependence for a fixed solar declination. Figure 1-16 shows the probability of F_1-formation in summer of 1958,

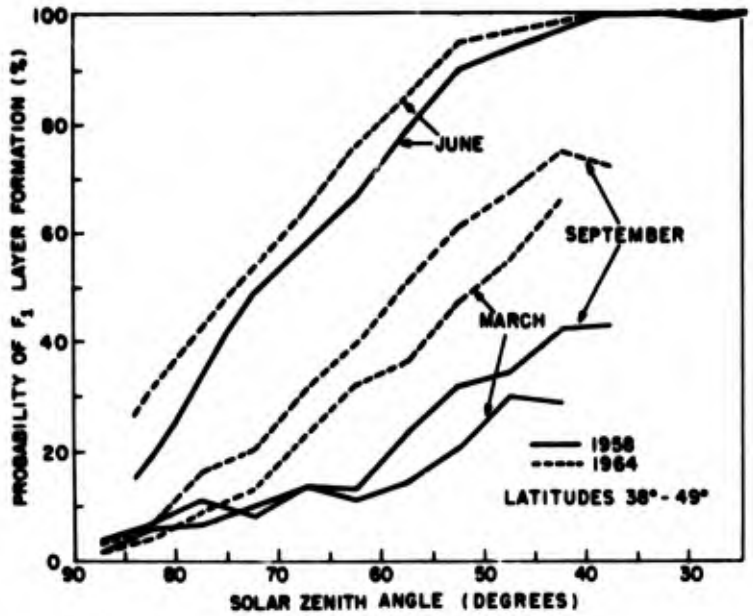

Figure 1-12. Probability of F_1-layer Formation as a Function of Solar Zenith Angle (latitudes 38^{o}-49^{o})

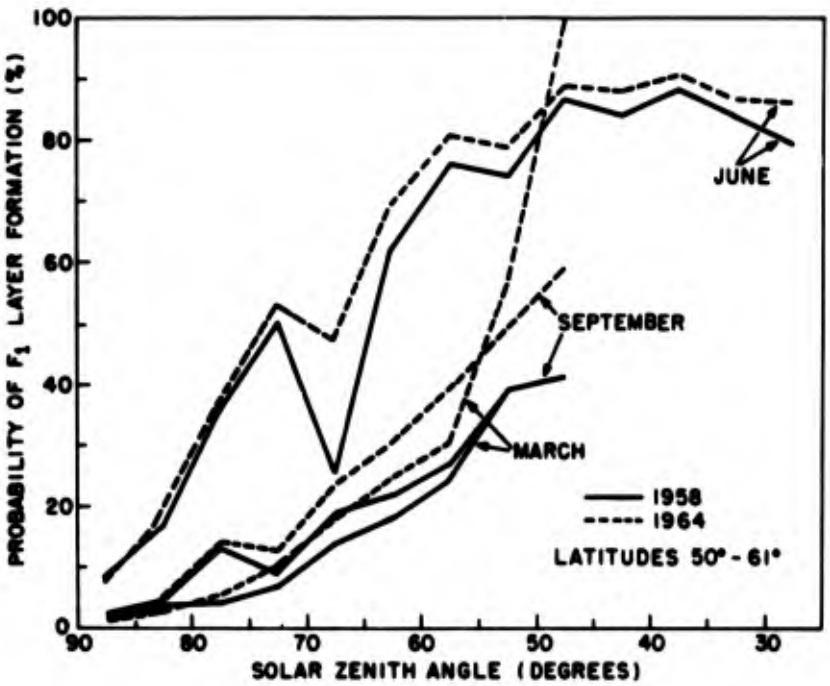

Figure 1-13. Probability of F_1-layer Formation as a Function of Solar Zenith Angle (latitudes 50^{o}-61^{o})

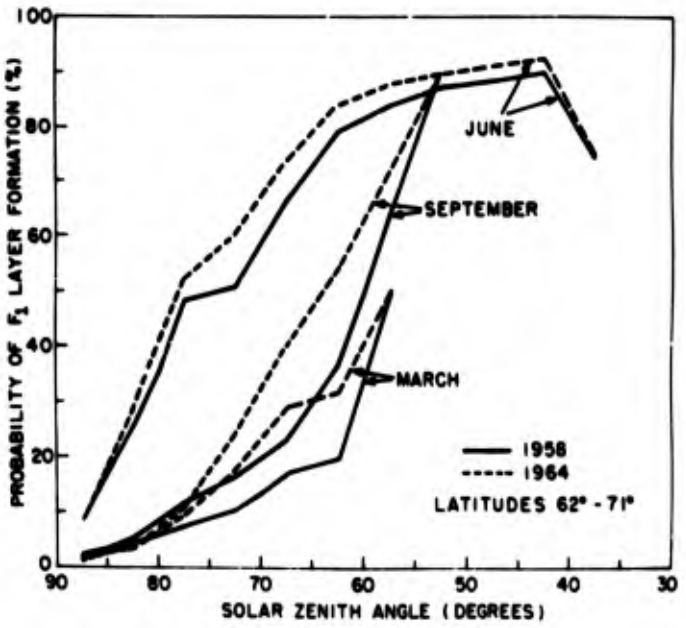

Figure 1-14. Probability of F_1-Layer Formation as a Function of Solar Zenith Angle (latitudes 62^{o}-71^{o})

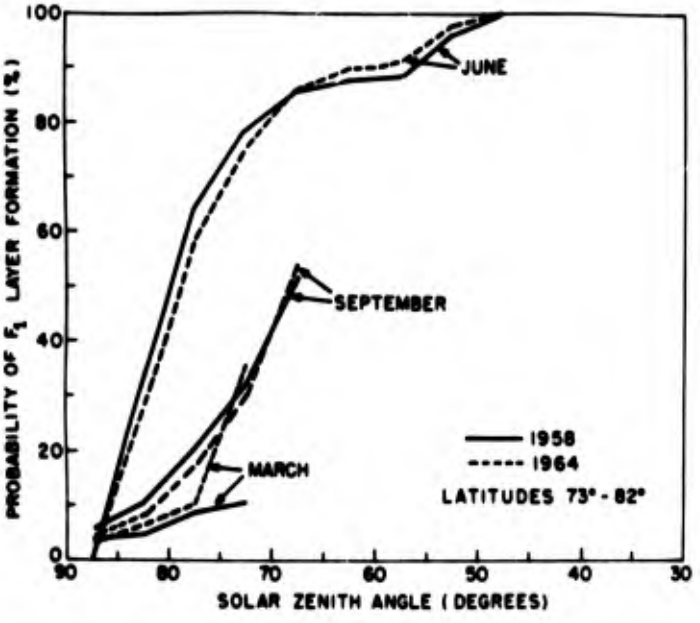

Figure 1-15. Probability of F_1-layer Formation as a Function of Solar Zenith Angle (latitudes 73^{o}-82^{o})

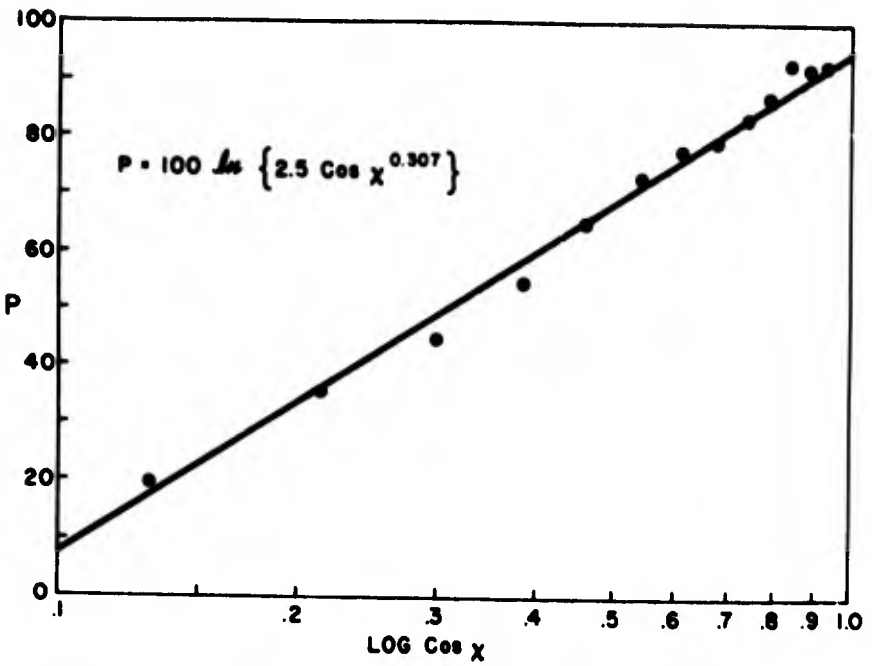

Figure 1-16. Probability of F_1-layer Formation Versus Log Cosine (zenith angle); June 1958 for Magnetic Latitudes 56°-66°

for a particular range of magnetic latitude, plotted as a function of the log cosine of the solar zenith angle. The relationship is approximately linear and may be written

$$\exp\left(\frac{P}{100}\right) = L_o \cos^q \chi$$

where the probability of formation with the sun at the local zenith is 100 ln L_o percent. L_o is thus seen, from the previous remarks, to be a function of solar declination (season) and, less notably, a function of phase of the solar cycle. This function may be written as

$$\ln L_o = 0.5 + 0.49 \cos\left[(D - 105)\frac{2\pi}{365}\right].$$

The value of the exponent, q, may be taken to be 0.3, as a reasonable average. There is no marked systematic difference between the results as expressed in geographic or geomagnetic latitude.

I-4. F_2-LAYER

In contrast to the lower layers, the F_2-layer is not in photochemical equilibrium. Diffusion and convection dominate the distribution of electron density in the region of the F_2-peak and above, with photochemical processes playing a secondary role. Although the present knowledge of the relative magnitudes of the winds and temperature gradients in the F-region is inadequate to permit a mathematical formulation of its parameters, some preliminary study of the basic physics of this region can lead to an optimum approach in constructing a theoretical model. Under equilibrium conditions, the F_2-layer is formed by the combined effects of photoionization and loss processes on the bottomside, and downward ambipolar diffusion on the topside. The diffusion flux decreases with decreasing altitude and disappears at about 1 to 2 scale heights below the F-layer peak. At the peak, it may be shown that, for daytime equilibrium conditions (Rishbeth and Barron, 1960)

$$N_m \sim \frac{q_m}{\beta_m}$$

where

N_m = electron density at the peak

q_m = ion pair production rate at the peak

β_m = linear loss rate at the peak

and

$$\beta_m \sim \frac{D_m}{H^2} \sin^2 I$$

where

D_m = ambipolar diffusion coefficient at the peak

H = density scale height

I = local magnetic inclination.

The ambipolar diffusion coefficient, D, is given by the expression

$$D = \frac{2kT}{m\nu_{in}}$$

where

k = Boltzmann's constant

ν_{in} = ion-neutral collision frequency

T = absolute temperature.

Thus it might be anticipated that N_m should have a tendency to be ordered in the geomagnetic coordinate system, because of the magnetic inclination factor. On the other hand, the solar production function, q, is clearly a function of geographic latitude and local time. Thus the spatial dependence of N_m is seen to be a complex entity. If an attempt is made to order experimental data in geographic latitude and local time, the magnetic inclination term will result in inconsistencies, which may be viewed as a longitude dependence of N_m.

At night, when the solar production function, q, is zero, the F-layer gradually assumes a shape established by the relatively rapid loss of electrons on the bottomside, with the electron density below the peak being partially sustained by downward diffusion from the topside where losses are negligible. This shape happens to resemble that of the Chapman layer (Dungey, 1956), and the F-region electron density decays exponentially with time until sunrise, preserving this characteristic shape as it does so.

1-4.1 Bottomside Total Content–Slab Thickness

The shape of the underside of the F-layer and its integrated electron content are quantities of interest in certain applications. It may be shown that the following relationship holds, under equilibrium conditions:

$$S_B = \frac{(TEC)_B}{N_m} = C H_i = C \frac{kT_i}{m_i g}$$

where S_B is a quantity having units of length, known as the bottomside slab thickness, $(TEC)_B$ is the bottomside total electron content, H_i is the ion scale height, and C is a dimensionless quantity which depends on the shape of the layer and the ratio of electron temperature to ion temperature.

Various mathematical profiles have been proposed to describe the F-layer electron density distribution, since as has been pointed out, it usually does not conform to a standard Chapman profile. In general, all of these profiles contain a parameter having units of length which may be associated with the layer thickness, usually denoted by y_m. This parameter is usually simply related to $(TEC)_B$. For example, for a parabolic profile

$$N = N_m \left[1 - (z-h_{max})^2 \Big/ y_m^2 \right],$$

it is easily shown that

$$y_m - 1.5 \frac{(TEC)_B}{N_m} = 1.5 S_B .$$

1-4.2 Height of the F-layer Maximum (hmax)

The height of the maximum F-layer density is an important parameter, especially in HF propagation applications. The layer maximum forms near the level at which the solar ion production rate (q) is equal to the chemical loss rate. This altitude varies during the day due to the varying solar zenith angle. An increase in q causes a decrease in h_{max} and vice versa. Thus the layer is generally at its lowest height near noon, and solar flares and other disturbances also cause a lowering of the layer.

The height of the maximum is somewhat more sensitive to variations in electron temperature than is the maximum electron density, which is determined primarily by chemical loss processes. Disruption of thermal equilibrium in the plasma upsets the condition of diffusive equilibrium which establishes the stable F-layer. Thus, at sunrise, the layer height drops rapidly by 40 to 50 km, due to a large increase in the downward diffusion flux, while the peak density changes only slightly. After sunset, the rapid cooling of the electrons again enhances diffusion, so that despite the very high loss rate, which causes N_m to drop rapidly, h_{max} remains near its daytime equilibrium level for several hours after sunset. The layer then begins to rise and continues until it reaches a level where diffusion and loss processes are equal, which usually occurs around midnight. The nighttime F-layer is maintained principally by ambipolar diffusion downwards from the upper ionosphere and protonosphere, which act as reservoirs. In certain localized regions—notably the auroral oval and, at times, the polar cap—precipitation of magnetospheric particles produces ionization by collision with neutrals, at F-region altitudes. Under these circumstances, the nighttime F-region profile may differ markedly from the "normal" nighttime profile.

1-4.3 f_0F_2 Model

The empirical model for f_0F_2 is based upon analysis of the following data:

(1) 320,000 hourly values of f_0F_2 from the ionosondes listed in Table 1-1, for each day of 1958 (average sunspot number 189).

(2) 35,000 hourly values of f_0F_2 from the ionosonde stations in Table 1-1 which are marked with an asterisk, for each day of March, June, September and December of 1964 (average sunspot number 10).

(3) 180,000 topside f_0F_2 values measured by Alouette 1 during the complete year 1963, and an additional 80,000 values for various months of the years 1966 to 1968. These values are not uniformly distributed, with the bulk being measured over the Western Hemisphere.

The analysis of this data was based on the assumption that the data are ordered in two prime coordinate frames:

(1) Geographic latitude and local time.

(2) Geomagnetic latitude and geomagnetic time; the magnetic coordinates are those described by Hakura (1965) and updated by Gustaffson (1970), and known as "corrected geomagnetic coordinates".

It was nevertheless recognized that—due to the effects of winds, nonsymmetry of the geomagnetic field, and other factors—there is no unique time coordinate which is orthogonal to these latitude parameters. Consequently, the possibility of true longitude variations is allowed for in modeling f_0F_2. Because attention is confined to latitudes greater than about 40°, it was not considered necessary to use a spherical geographical coordinate system. Instead, cylindrical coordinates are used, with latitude as the radial and time as the azimuthal coordinates.

Figure 1-17 shows the data for the five geomagnetically quietest days of December 1958, averaged in 5° increments of geographic latitude. The characteristic

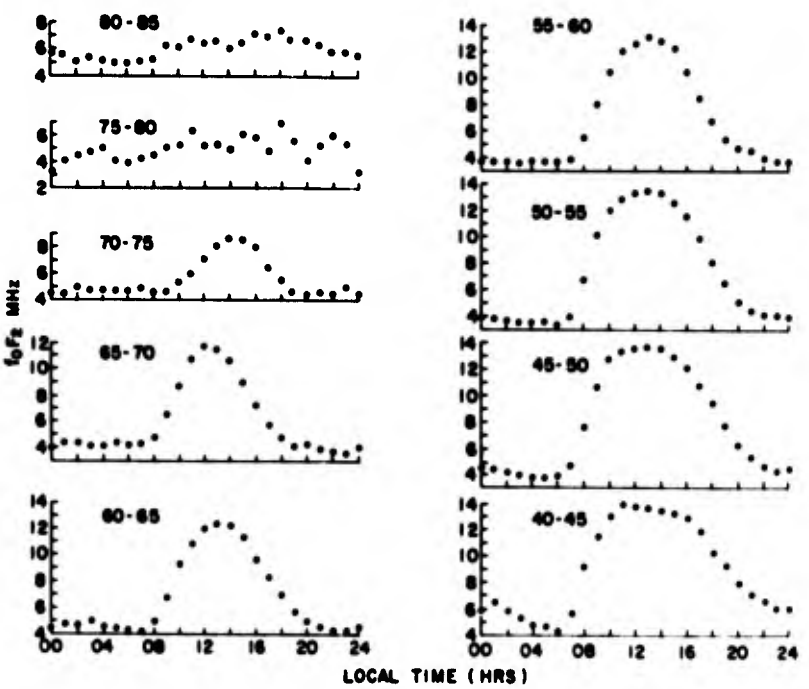

Figure 1-17. Diurnal Variation of f_0F_2 in 5° Latitude Intervals; Quiet Days, December 1958

diurnal variation of f_oF_2 is apparent for all latitudes at which the sun rises at some time during the day. At the highest latitudes, where the sun does not rise at all in December, the value of f_oF_2 is fairly constant, displaying only small irregular fluctuations. Figures 1-18 and 1-19 show the median contours for the months January 1958 and January 1964, plotted in corrected geomagnetic coordinates. It must be pointed out that such a display inevitably smears out the local time effects at high latitudes on the dayside of the earth, but of course brings out clearly any magnetically ordered effects, such as the trough and the auroral oval. These are more apparent on the nightside, and more so in 1964 than in 1958, and are clearly smaller than the local time ordered effects associated with solar UV irradiation.

It was decided to represent the diurnal variation of f_oF_2 by a Fourier expansion

$$f_oF_2(t) = a_o(\phi) + \sum_{n=1}^{N} a_n(\phi) \cos\left(\frac{2\pi nt}{24} + \theta_n\right)$$

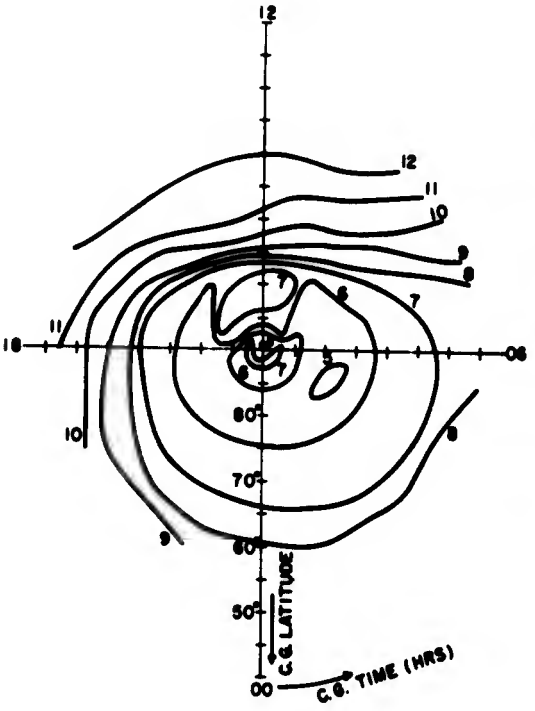

Figure 1-18. Median f_oF_2 Contours for January 1958, Synthesized by a 12-harmonic Time Series; Corrected Geomagnetic Coordinates

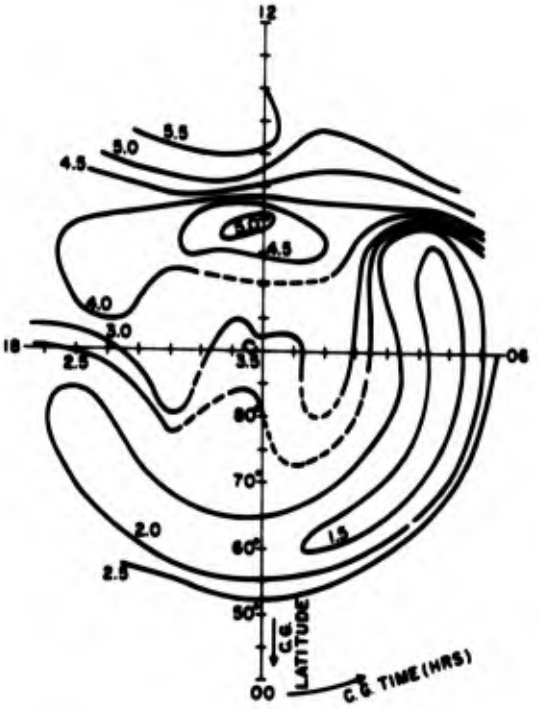

Figure 1-19. Median f_oF_2 Contours for January, 1964, in Corrected Geomagnetic Coordinates

where ϕ equals geographic latitude, and t equals local time. The choice of the highest order harmonic (N) to be used was based on the conflicting requirements of accuracy and simplicity of the model. It was found that, in the majority of cases, N = 3 provided sufficient accuracy and this was chosen as the compromise value. Figure 1-20 shows how the magnitude of the harmonics, a_n, varies with n for several high latitude ionosonde stations. For the purpose of comparison, the magnitude of 0.05 times the monthly median value is also shown. Figure 1-21 shows a typical diurnal variation of f_0F_2, together with a 2-harmonic approximation and a 3-harmonic approximation. This figure reveals a noteworthy point. Although the overall fit of the 3-harmonic approximation is tolerably good, the maximum discrepancy occurs near sunrise, when the value of f_0F_2 rises abruptly. It was found necessary to include harmonics up to order 6 in order to reduce this discrepancy to a value compatible with the remainder of the fit, and this additional complexity in the model was not considered to be warranted. The obvious point to be taken from this is that the Fourier harmonics, while a convenient set of orthogonal coordinates, are not the optimum ones. Nevertheless, none of the other conventional orthogonal coordinate systems is likely to be superior in representing the diurnal f_0F_2 variation, and the proper approach, which should be employed in a future model is to develop an empirical orthogonal coordinate system, using statistical analysis of the data itself.

The data for the five magnetically quietest days of each month for each ionosonde station were averaged, and the resultant "composite day" was then Fourier analyzed. These quiet days are assumed to represent the solar contribution with a minimum of complications due to energetic particle precipitation, Joule heating, and other less obvious effects. Of course, these effects are always present in the high latitude ionosphere, but they are presumably stable and have their smallest magnitude on quiet days. The amplitude and phase of each of the Fourier harmonics were then plotted as functions of geographic latitude. The overall results may be summarized as follows:

(1) a_0 exhibits a steady decrease from low latitudes towards the geographic pole, and is adequately represented by a linear fit

$$a_0 = m_0\phi + I_0$$

where m_0 is the slope, and I_0 is the (fictitious) intercept at the equator (the model is defined only in the range $90^\circ > \phi > 40^\circ$).

(2) a_1 shows a more complicated behavior, in that it is relatively constant in the range $40^\circ < \phi < \sim 58^\circ$, and then falls to a value near zero at the pole. This term is represented by a piecewise linear approximation

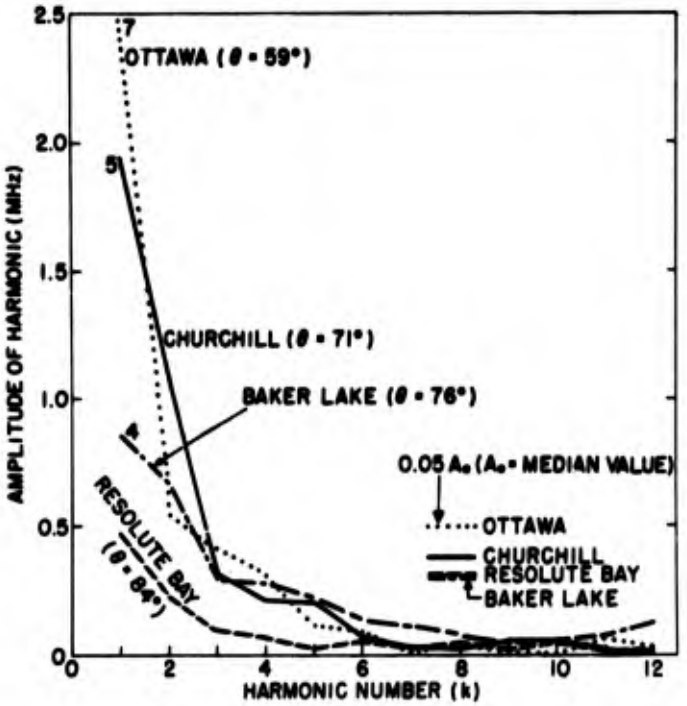

Figure 1-20. Amplitude (MHz) of the k^{th} Harmonic of the f_0F_2 Variation for Several Selected Stations (December, 1958)

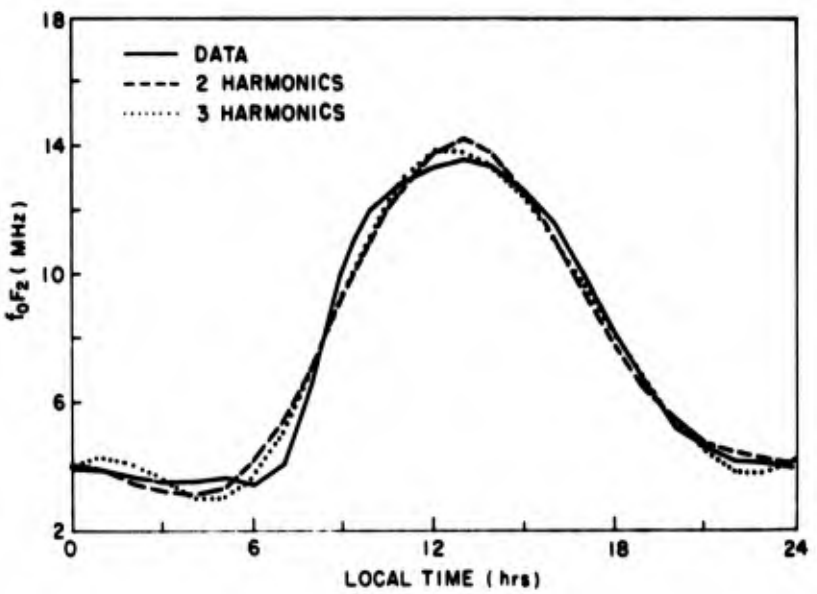

Figure 1-21. Comparison of 2- and 3-harmonic Fits With Diurnal Variation of f_0F_2; Average of Stations in Latitude Range 45^o-50^o (December, 1958)

$$a_1 = I_{11} \qquad (40^\circ < \phi < 58^\circ)$$
$$a_1 = m_1\phi + I_1 \qquad (58^\circ < \phi < 90^\circ).$$

I_{11} varies with season, but since the sloping line is assumed to pass through zero at the pole, I_{11}, I_1 and m_1 are interrelated.

(3) θ_1 shows little latitude dependence and is adequately represented by a constant value for a given month.

(4) a_2, a_3, θ_2, θ_3 are all sufficiently small that, even for magnetically quiet days, the "noise" inherent in the data precludes a determination of their latitude dependence, except to note that any such dependence, if present, is quite small. All of these parameters are represented by constants for a given month.

By plotting a_o and a_1 as contours in geographic coordinates, for the various months, it was noted that there was a clear tendency for symmetry to be displayed about both geographic and geomagnetic poles. It was also apparent, however, that other longitude effects were present which could not be explained as simply as this. It was clear that the latitude dependences $a_o(\phi)$ and $a_1(\phi)$, which have been derived, are averages over longitude, and some correction term must be applied.

The next step in constructing the model consists of deriving the seasonal dependence of the three Fourier harmonics for 1958. The parameters m_o, I_{11}, I_1, a_2, a_3, θ_1, θ_2, θ_3 were fitted with Fourier series of the form

$$\xi(D) = h_o + \sum_{n=1}^{3} h_n \cos\left(\frac{2\pi nD}{365} + \alpha_n\right)$$

where D = day number in the year. In this way, a closed-form model was derived for the geographically ordered term, for the magnetically quiet days of 1958. The next step was to analyze the residuals from the model and to attempt to order them in the geomagnetic coordinate system. An initial attempt was made to repeat the above procedure, as follows:

The "geographic" term just derived was substracted from each data point for the individual quiet day averages for each station,

$$(f_oF_2)_R = \left((f_oF_2)^2 - (f_oF_2)_G^2 \right)^{1/2}$$

where the subscripts R and G refer to "residual" and "geographic" respectively. These residual values were then Fourier analyzed with corrected geomagnetic time as the appropriate coordinate, and the values of the Fourier expansion coefficients plotted against corrected geomagnetic latitude, in a manner analogous to the analysis in geographic coordinates. In this case, however, no clear latitude

dependence could be discerned, with the results being noiselike in character. This is likely a result of the fact that geomagnetically ordered effects are not rotationally symmetric in the geomagnetic coordinate system. As a consequence of this failure to order the residuals in this way, it was decided to omit geomagnetic time as a prime variable. The compromise solution was to allow for a longitude correction term for a_o, together with a geomagnetic latitude correction term for both a_o and a_1.

The longitude term was examined by grouping the ionosonde stations in two sectors; the "American" and "European" sectors. The Fourier coefficient a_o was plotted as a function of geographic latitude for each month and each sector. There was an apparent seasonal dependence in the deviation from rotational symmetry about the geographic pole, and the deviation from the quiet "geographic" model was maximum at a geographic latitude of $\sim 55^o$. The model, therefore, contains a piecewise linear correction term which is a function of longitude (λ), latitude (ϕ), and day number (D). The station density did not permit a complete representation of the longitude dependence, which is therefore expressed as a separate function of ϕ and D for three longitude sectors:

$-15^o < \lambda < 165^o$ (East positive)

$165^o < \lambda < 195^o$

$195^o < \lambda < 345^o$.

A set of residual Fourier coefficients Δa_o and Δa_1 were then formed by subtracting the geographic model and the above longitude effect from the actual Fourier coefficients a_o and a_1. The coefficients Δa_o and Δa_1 were then plotted as functions of corrected geomagnetic latitude (Φ), for each month. The plots show a characteristic "S" shape with a maximum in the vicinity of $\Phi = 80^o$ and a minimum in the vicinity of $\Phi = 58^o$, although these values differ between Δa_o and Δa_1 and also exhibit seasonal variations. It was decided to model these variations with a cubic equation, constrained to have a maximum at Φ_{max} and a minimum at Φ_{min}, where these maxima and minima are functions of season for a_o and a_1. The coefficients of these cubic equations were determined by least square fitting to the data, and are contained within the model as functions of season. In this way, the original Fourier expansion in local time has been amended so that its coefficients are functions of ϕ, Φ, λ, D.

At this point it is necessary to consider the effects upon f_oF_2 of varying magnetic activity. The index of magnetic activity which was used was K_p, which is available in 3-hr intervals of UT. The range of K_p values was divided into seven increments, so that, except for the lowest and highest, all increments had

approximately the same population. Then, the f_oF_2 data for each station-month combination were sorted so that seven "composite days" were constructed for each station and for each month, each one corresponding to a different K_p level. Then, using the basic quiet day model in geographic coordinates, and the longitude correction, the geomagnetic latitude correction term was evaluated, as before, for each of the seven composite days. The result of this analysis showed that a_o has a K_p-dependent term which is also seasonally dependent, having maxima at the equinoxes, and also that Φ_{max} and Φ_{min} are functions of K_p.

1-4.3.1 MULTIPLE REGRESSION ANALYSIS

At this stage, the basic structure of the f_oF_2 model had been determined for a year of very high sunspot number (1958). It remained to "fine tune" the model, and to determine the solar cycle dependence, to the extent possible with the limited data available. For this purpose, a multiple regression analysis procedure was used in which each of the terms was introduced separately in closed form. The program then provided regression coefficients for the data against each variable separately. In the course of this analysis, it was found necessary to add another term to a_o to account for a solar cycle dependence of the seasonal variation in the overall mean amplitude of f_oF_2. It is interesting that this term maximizes in the winter in 1958, thus reinforcing the seasonal anomaly which exists in f_oF_2. However, in 1964 the additional seasonal term maximizes in summer, thereby reducing the magnitude of the seasonal anomaly. Inspection of the data for quiet days does, in fact, show that the seasonal anomaly is much reduced in 1964, with summer and winter noon values of f_oF_2 being about equal, whereas in 1958 they differ by a factor of about 1.8.

The solar cycle dependence was determined from all of the available data, and found to be of the form

$$f_oF_2 = 4.8 + 0.42\,(a_o+a_1+a_2+a_3) \times (1.0+0.012R-2.6\times10^{-5}R^2)$$
$$\pm\, 0.6 \cos\frac{2\pi}{365}(D+11)$$

where the + sign in the last term is used for $R > 100$ and the - sign for $R < 100$. This rather crude procedure is all that the available data warranted, and clearly requires improvement at some future time.

The model was then used to attempt to reconstruct the original data, and a detailed comparison was made between the predicted model values and the data from the "composite days". In general, the results were acceptable, with deviations from the data about the modeled values being fairly randomly distributed. However, there were found to be two regions in which significantly nonrandom deviations occurred; these deviations were maximum in winter and diminished to

zero in summer. On the dayside, in the cleft precipitation region, the modeled values were too high, typically by 2 to 4 MHz in winter 1958. On the nightside, at the low latitude boundary of the auroral oval, a band of values were found to be too low by about 1 MHz in winter 1958. A final correction term was therefore added to the model, having the following form:

$$(f_oF_2)_{corr} = f_oF_2 + 0.25\ K_p \cos\frac{\pi H_M}{12} \exp -\frac{(\Phi - \beta)^2}{6} \qquad H_M > 18;\ H_m < 6$$

where

$$\beta = 72 - 1.8\ K_p + 5.1 \cos\frac{\pi}{12}(H_M - 1)\ \text{deg.}$$

Also

$$(f_oF_2)_{corr} = f_oF_2 \left[1 - (1 - \eta) \exp -\frac{(\Phi - \alpha)^2}{6}\right] \qquad 6 < H_M < 18$$

where

$$\alpha = 80 - 1.2\ K_p\ \text{deg,}$$

$$\eta = 1 - 0.35 \cos\frac{\pi}{12}(H_L - \phi) \cdot \left[1 + \cos\frac{2\pi}{365}(D+8)\right] \Big/ 2,$$

and ϕ is the phase term in the diurnal Fourier expansion of f_oF_2. The value of η was truncated so that $\eta \leq 1$ always. Thus this correction can never increase the originally modeled f_oF_2 value on the dayside of the auroral oval. The Gaussian functions were chosen arbitrarily on account of their desirable asymptotic characteristics, and have no physical significance. The nightside correction term is additive, so that its influence is proportionately smaller at solar minimum than at solar maximum, which appears to be consistent with the data. Conversely, the dayside correction term is multiplicative, implying proportionately equal influence throughout the solar cycle. This dayside correction term is located at the ionospheric projection of the magnetospheric cleft and has a magnitude which is largest in the early afternoon during winter. It is apparently associated with a modification of the vertical diffusion flux by changes of the vertical temperature gradient caused by particle precipitation through the cleft.

1-4.1 True Height Ionogram Analysis

The parameters h_{max}, hF_1 and $(TEC)_B$ must be obtained from true height analysis of bottomside ionograms. For this reason, the following true height profiles were assembled:

(1) Composite profiles (profile derived from the average ionogram for a given hour for an entire month) for stations:

Reykjavik
Godhavn
Thule
Ottawa
Winnipeg
Churchill
Resolute Bay

These profiles were obtained for the hours 00, 06, 12, 18 LMT in March, June, September and December of 1958 and 1964.

(2) Composite profiles at 00 and 12 LMT only in March, June, September and December at the following stations, where the existence or absence of data in 1958 and 1964 is indicated:

Station	1958	1964
Point Barrow	X	X
Lulea	X	
Victoria	X	
Anchorage	X	X
Washington	X	
Baker Lake	X	
Eureka	X	
Fletcher's Island	X	
Meanook	X	
Narssassuak	X	
Gorky	X	X

(3) Composite profiles for all 24 hr local time for the months September, October and November of 1962 and 1963 at Adak, Narssassuak, Thule, and Godhavn.

(4) Individual profiles for every hour in April, May, June and July of 1970 at:

Godhavn
Narssassuak
College
Churchill
Winnipeg
Ottawa
St. Johns
Hanover
Boston

(5) Published data for January, June and September, 1958 at:

Tikhaya Bay

Tixie Bay

Alert

North Pole 6

North Pole 7

Eureka

by Astakov et al (1970).

An example of several composite profiles is shown in Figure 1-22. The available body of true height analysis was sufficient to permit construction of a reasonably accurate model of the bottomside ionosphere. Further analysis is in progress which will provide an even more complete estimate of day-to-day variability, and of temporal and spatial variations associated with the rotation of the earth beneath the auroral oval. The solar cycle dependence, of course, is not very well defined by analysis of data at the extremes of a solar cycle, where the bulk of the available data is located. The solar cycle dependence has been deduced partly from the available data at moderate sunspot number and partly, in the case of the scale height, by noting the strong dependence upon neutral atmosphere parameters for which a well tested model exists. Further, the results of Becker and Stubbe (1963) have been extrapolated from midlatitudes and found to be satisfactory for some purposes.

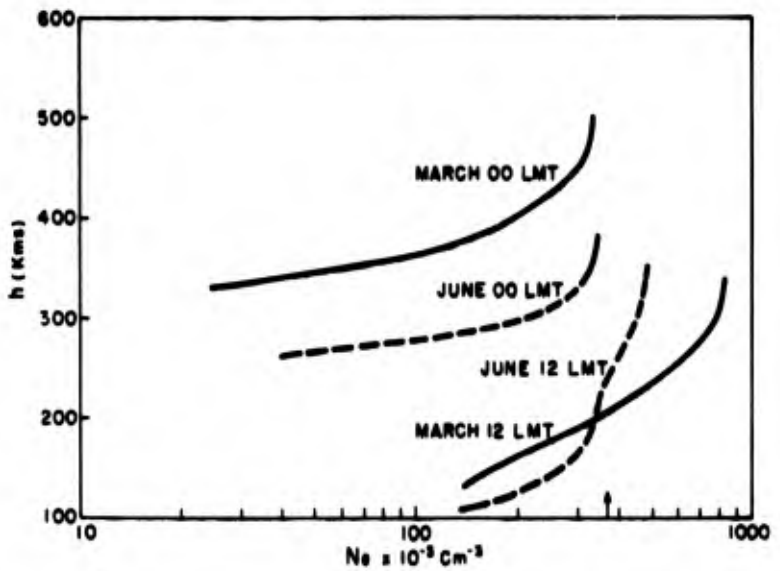

Figure 1-22. Example of True Height Profiles From Anchorage, 1958. The vertical arrow shows the value of f_0F_1 which is predicted by the model (Figure 1-9)

1-4.4.1 TOPSIDE TRUE HEIGHT PROFILES

True height profiles deduced from topside soundings taken by Alouette 1 were made available by Dr. G. Lockwood (CRC, Canada), spanning the years 1963 to 1967. The bulk of the data, however, was concentrated in the 1963 to 1965 period. The analysis of this data is the subject of a separate report, but some results of that analysis have been included in this report. The original data were first interpolated so as to form an array of uniformly spaced (in altitude) electron density samples. The profiles were then sorted and a new data file constructed, consisting of all profiles taken at geomagnetic latitudes greater than 40^{o}, together with such additional information as solar flux, planetary magnetic activity, and magnetic time. This data file, consisting of 38, 000 profiles spaced at 100 km in the vertical from 350 to 950 km, formed the basis of the topside profile in the present model.

1-4.5 Model for the Height of F-Layer Maximum (h_{max})

A model for h_{max} was devised which reproduces the principal diurnal, seasonal and solar cycle dependences, while being very simple and economical in terms of computation requirements.

The diurnal variation chosen was a piecewise linear combination based upon solar zenith angle and therefore containing most of the seasonal and latitudinal dependences as well. The work of Penndorf and Katz (1969) was taken as a guide, and while this was developed for midlatitudes, it was found to be also a reasonably close approximation to reality at high latitudes. The height h_{max} remains at its nighttime equilibrium level until sunrise at the level of substantial ion production, which occurs at a solar zenith angle of 101^{o}. Then h_{max} falls linearly until $\chi \sim 87^{o}$ is reached, when it becomes constant, and remains so until $\chi \sim 78^{o}$. Finally, h_{max} begins to rise linearly, and this rise can be taken to continue until midnight, when nighttime equilibrium is again achieved. This behavior is illustrated in Figure 1-23.

The diurnal variation is completely specified when the values of h_{max} at two points on this piecewise linear approximation are established. For convenience, these "calibration" points are taken to be the values at midday and midnight—h_{12} and h_{00}, respectively. It is now necessary to establish the latitudinal and seasonal dependences of h_{12} and h_{00}, exclusive of the solar zenith angle dependence, and also their solar cycle dependence. In connection with the solar cycle dependence, it should be noted that the critical solar zenith angles—at which the slope of the h_{max} - t curve changes—probably should also be functions of solar activity since the density of the neutral atmosphere at a given altitude exhibits a very pronounced dependence on solar flux and, therefore, the altitude of maximum ion production

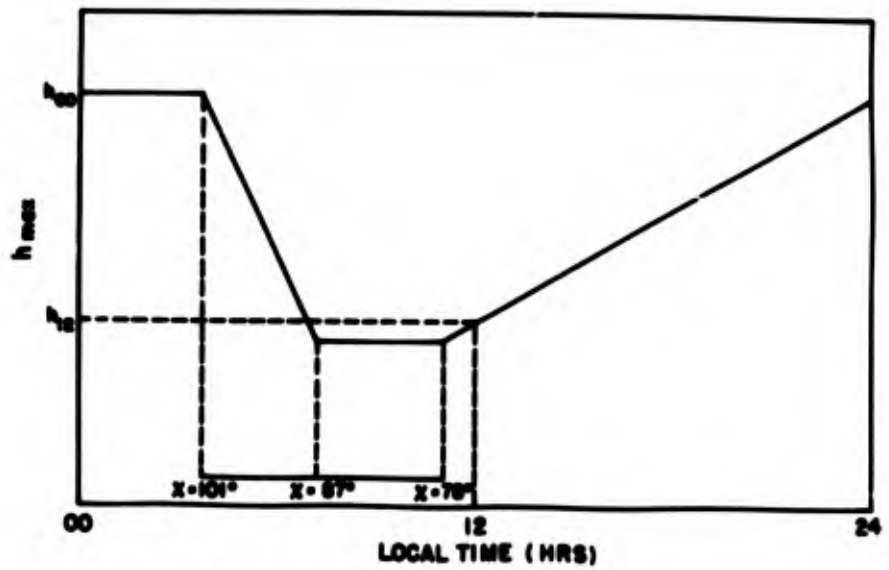

Figure 1-23. Idealized Diurnal Model for the Height of the F-layer Maximum

should also be expected to vary over a solar cycle. Indeed, it is clear from work of Rishbeth and Setty (1961) that such a solar cycle trend in these angles is observable, but it is not yet clear what this dependence should be. This is an area which requires further refinement, but should not produce very substantial errors in modeling.

The values of h_{12} and h_{00} were taken from the true height profile analysis, described in Section 1-4.4, and plotted as functions of both geomagnetic and geographic latitude for March, June, September and December of 1958 and 1964 (see Figures 1-24 through 1-27). The results were consistent with the diurnal variation assumed, with the exception that a substantial increase in h_{max} is observed at night near 65^{o} geomagnetic latitude, which is presumably associated with the auroral oval. From these plots the seasonal variation (exclusive of zenith angle variation) is seen to be insignificant, and there is a small geomagnetic latitude gradient which can be represented by 0.55 km increase in h_{max} per degree of geomagnetic latitude at midday, and a decrease of about 1.0 km per degree at midnight.

The solar cycle dependence can be estimated approximately from the true height profiles available. A more accurate representation of the solar cycle dependence, however, requires a more uniformly distributed data sample. Becker and Stubbe (1963) have published the results of careful true height analysis of ionograms taken at Lindau. Although this is not a high latitude station, the solar cycle dependence at this location is found to be similar to that at

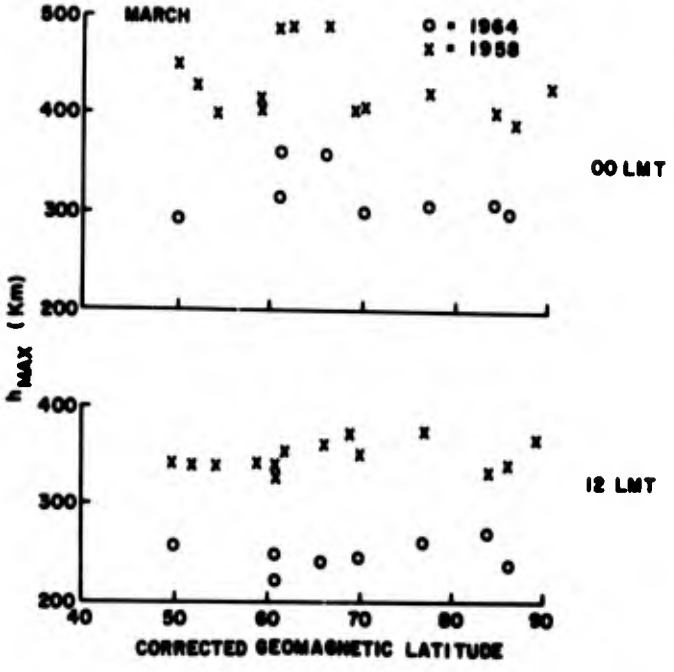

Figure 1-24. Variation of h_{max} for Composite Profiles, as a Function of Corrected Geomagnetic Latitude, at Midnight and Midday (March, 1958 and 1964)

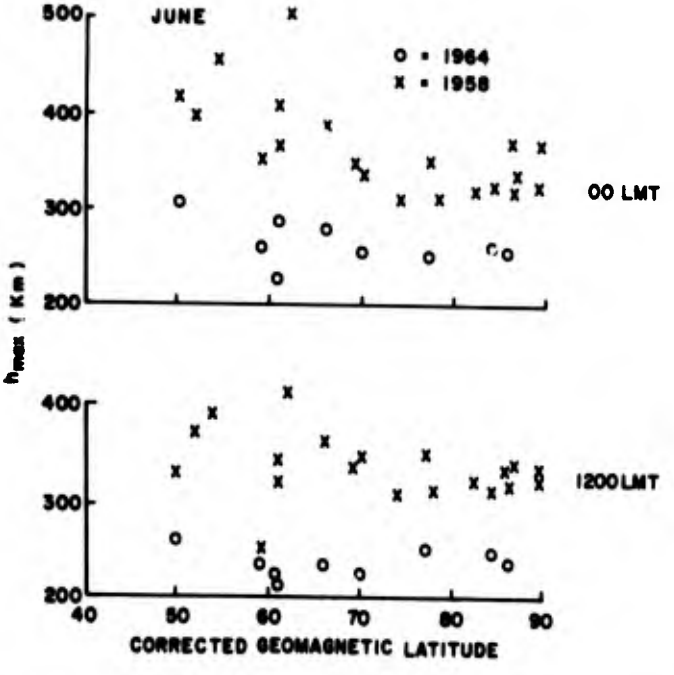

Figure 1-25. Variation of h_{max} for Composite Profiles, as a Function of Corrected Geomagnetic Latitude, at Midnight and Midday (June, 1958 and 1964)

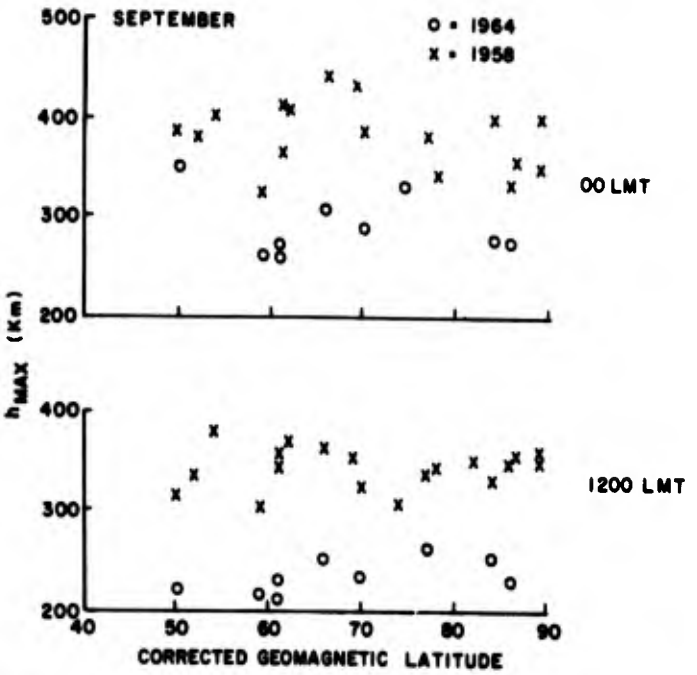

Figure 1-26. Variation of h_{max} for Composite Profiles, as a Function of Corrected Geomagnetic Latitude, at Midnight and Midday (September, 1958 and 1964)

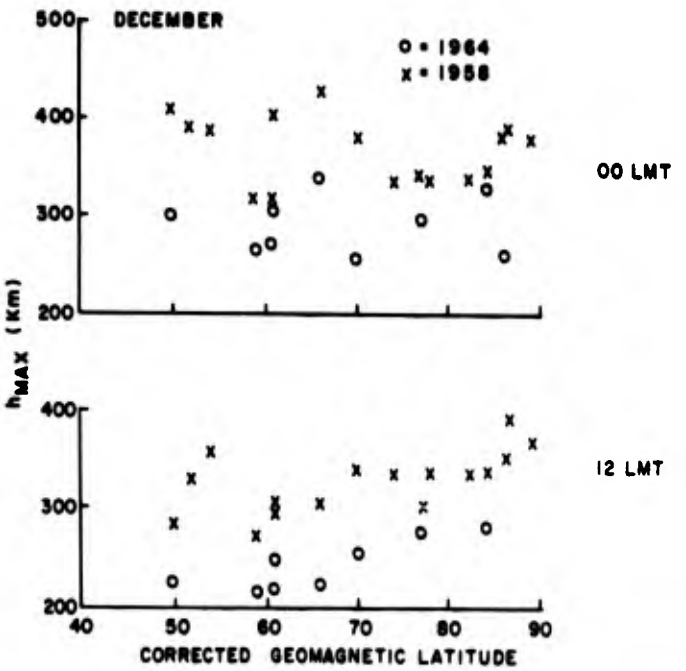

Figure 1-27. Variation of h_{max} for Composite Profiles, as a Function of Corrected Geomagnetic Latitude, at Midnight and Midday (December, 1958 and 1964)

high latitudes, to within the limits of accuracy set by the available data. The solar cycle dependence assumed for the high latitude model is

$$h_{00} = 297 + 0.603\ R - 1.0\ (\Phi - 45^{o})\ \text{km}$$

$$h_{12} = 197 + 0.79\ R - 1.1 \times 10^{-3}\ R^{2} + 0.55\ (\Phi - 45^{o})\ \text{km}.$$

Thus except for the region of the auroral oval at night, the h_{max} variations are fully modeled. The increase in h_{max} at the auroral oval amounts to about 100 km at sunspot maximum (1958), and about half this amount in 1964. This increase may be assumed to be proportional to the nighttime exospheric temperature, which varies by a factor of about 1/2 from 1958 to 1964. Note that since these data are for composite profiles, the results are probably close to those for average levels of magnetic activity. The median height, h_{max}, in the nighttime auroral zone region may be estimated as

$$h_{00} + 0.08\ T_{N} \left\{ \exp - \frac{(\Phi - \beta)^{2}}{20} \right\}$$

where T_N (^{o}K) is the minimum nighttime temperature, and $\beta = 67 - 2\ K_p$ deg. Examples of the diurnal variation of h_{max} are presented in Figures 1-28 and 1-29, for the stations Godhavn, Narssassuak, College, and Churchill, for the months April and May in 1970. In spite of the rather erratic behavior exhibited by these monthly mean variations, the diurnal effect is clearly seen, as is an apparent latitude dependence.

1-1.6 Total Bottomside Electron Content

The total integrated electron content below the peak of the F-layer may be represented approximately by

$$(TEC)_B = C\ H_n(N_m F_2)$$

where

H_n = neutral density scale height at the layer peak

= kT/mg, and

where

T = absolute temperature at the peak

m = mean molecular weight at the peak

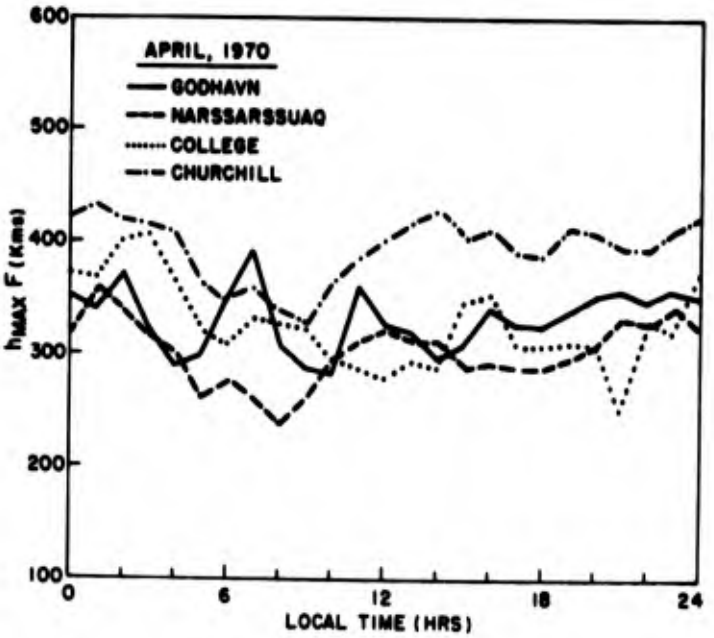

Figure 1-28. Diurnal Variation of h_{max} for Four High Latitude Stations in April, 1970 (average of all days in the month)

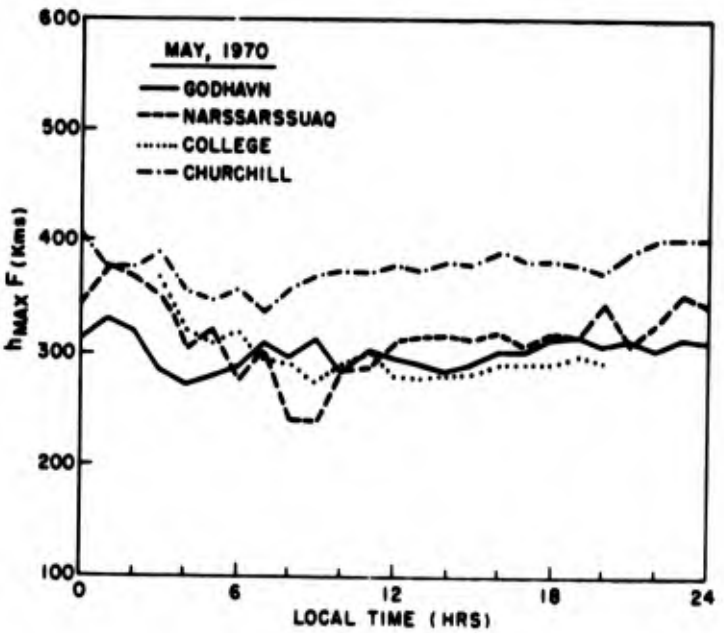

Figure 1-29. Diurnal Variation of h_{max} for Four High Latitude Stations in May, 1970 (average of all days in the month)

g = acceleration of gravity at the altitude of the peak

k = Boltzmann's constant.

The quantity C in the above expression is dependent on the electron temperature and, therefore, on the solar zenith angle. It is also weakly dependent upon the shape of the layer vertical profile, so that its experimental determination is only an approximate means of determining electron temperature. Figure 1-30 shows the average diurnal variation of bottomside total electron content for the months September, October and November in 1962 and 1963, at Adak, Alaska. Also shown is the diurnal variation of bottomside slab thickness, and the diurnal variation of C, which was obtained after computing the neutral scale height. The range of sunrise and sunset times during this period are shown on the time axis. The sharp rise in C immediately following sunrise is obvious, and reflects the rapid increase in electron temperature in this unstable period. The decrease in C around sunset is more gradual, but many cases were observed in which the diurnal variation of C was more symmetrical about noon than in this example. Furthermore, the rapid rise near sunrise was observed to commence at a solar zenith angle of 101°, corresponding to sunrise at the level of maximum ion production with grazing incidence on the ozone layer. The value of C generally was observed to continue to rise for about 4 hr before leveling off. The diurnal variation of C has therefore been assumed to be that shown in Figure 1-31. No doubt further refinement is possible with a larger data base.

The midday and midnight values of C (C_{12} and C_{00} respectively) are expressed as variables having a seasonal dependence. The midday value has an annual variation with an amplitude (minimum to maximum) of about half the average value. The midnight value has a semiannual dependence with amplitude about 60 percent of the average value. From the limited amount of true height data analyzed, it seems clear that the semiannual variation in C has its maxima in April and October, as does the neutral atmospheric density. It has been assumed that the annual variation in C_{12} is similarly asymmetric with respect to the solstices.

The diurnal variation of C requires that the ratio of electron to ion temperatures varies by a factor of ~ 2 from nighttime conditions to midday. Such a diurnal variation is consistent with incoherent backscatter measurements (for example, Gordon, 1967).

The model for $(TEC)_B$, and therefore also for y_m, is based upon a numerical model for the neutral atmosphere (Jacchia, 1970). This model requires as its input parameters, the location and altitude of the point in question, the date, magnetic activity and the 10.7-cm solar flux for the particular day as well as the 10.7-cm solar flux averaged over three solar rotations. In the absence of

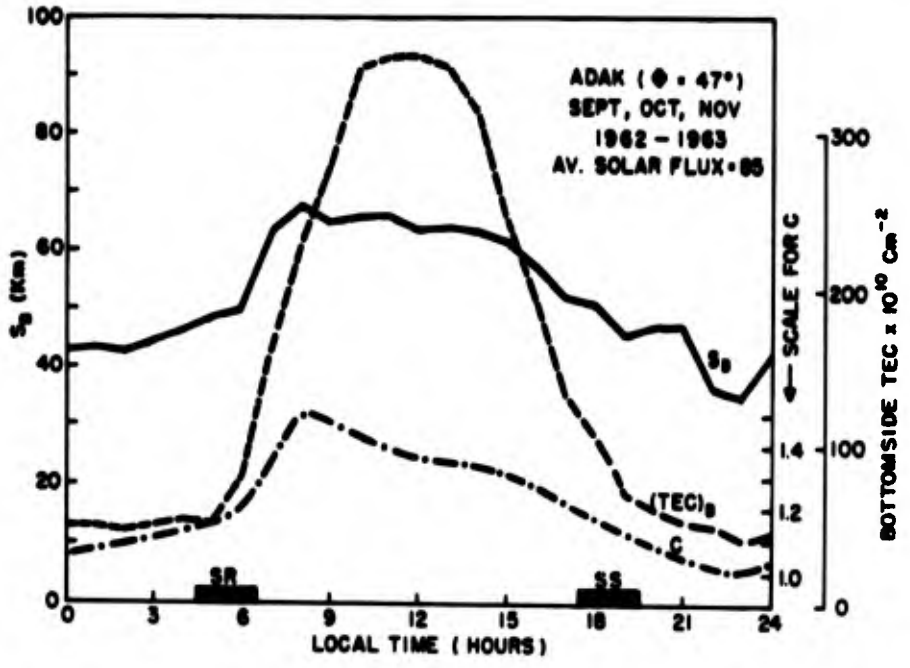

Figure 1-30. Average Diurnal Variation of Total Bottomside Electron Content and Slab Thickness for Adak, September - November, 1962 and 1963. Also shown is the diurnal variation of the ratio (C) of slab thickness to neutral scale height. The ranges of sunrise and sunset times for this period are indicated on the horizontal axis.

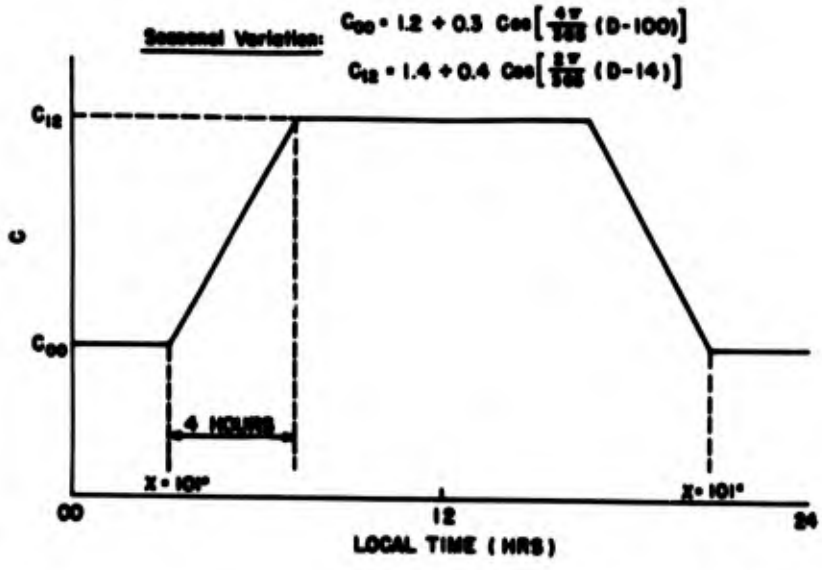

Figure 1-31. Model for C, Ratio of Bottomside Slab Thickness to Neutral Scale Height

actual data (for example in prediction applications), these two solar flux quantities may be taken as equal. If solar flux is not known, but sunspot number is known, the statistical relationship between these two quantities (Section 1-1.2) can be used to provide an input to the neutral atmosphere program. The computed output from the neutral atmosphere program consists of the following parameters: (1) Altitude variation of temperature, (2) altitude variation of neutral density, and (3) altitude variation of molecular weight. This program is called following computation of h_{max}, which is then passed as an input parameter to the subroutine "JACCHIA".

Figures 1-32 and 1-33 further illustrate the variation with local time of the bottomside slab thickness ($S_B = CH_n$), for the month of April 1970. Figure 1-32 shows the average slab thickness for four high latitude stations while Figure 1-33 shows the slab thickness for a midlatitude station, together with the standard deviation for the month. The effects of difference in the length of the day can be seen clearly, even for April, which is close to the equinox.

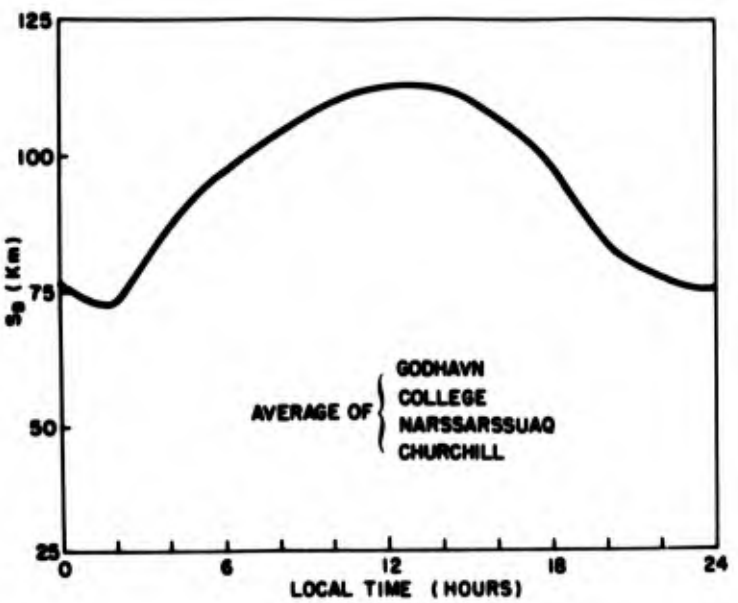

Figure 1-32. Average Diurnal Variation of Bottomside Slab Thickness for Four High Latitude Stations (April, 1970)

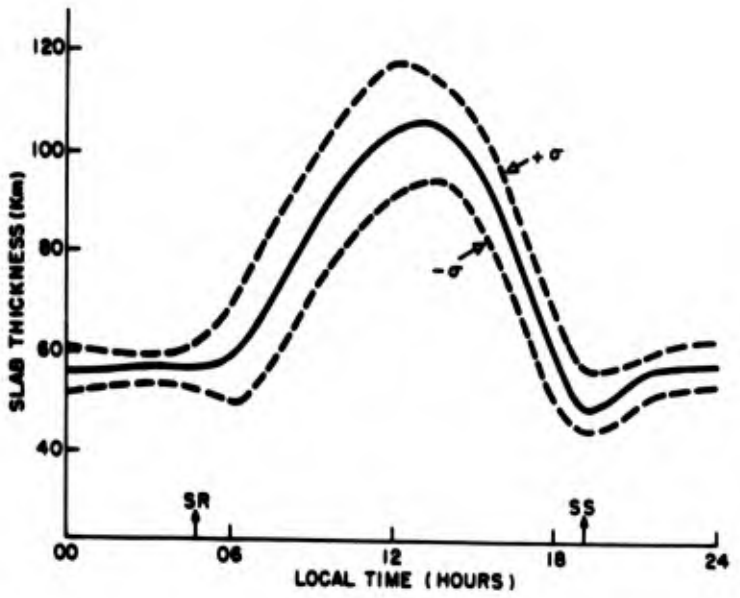

Figure 1-33. Bottomside Slab Thickness for Hanover, New Hampshire. Mean for April 1970 is shown, together with standard deviation of all values observed for the month. Sunrise and sunset times for April 15 are shown

1-4.7 Comparison of f_oF_2 Model With ITS-78 Model

The most widely used model for the worldwide distribution of f_oF_2 values is the so-called "ITS-78 Model" (Barghausen et al, 1969), which is basically an empirical mapping of monthly median ionosonde data on to a spherical coordinate system. This model contains a great deal of information on the statistical distribution of several ionospheric parameters, as well as a simple point-to-point ray tracing procedure, and is principally designed for HF communications usage. It is of interest to compare the values of f_oF_2 generated by the present model with comparable estimates for ITS-78, recognizing that the objectives and framework of these two models are, in some respects, rather different.

Figures 1-34 through 1-44 illustrate this comparison for a number of cases, which may be described as typical, although they have been selected to illustrate certain essential features of the two models. These figures show the diurnal variation of f_oF_2 for the particular month, year, and K_p index shown, at the locations of some of the ionosondes in use at that time. Also shown is the diurnal composite day variation for the same station and K_p value, which may be taken to represent "reality", in the sense that it constitutes at least part of the data from which both models were derived. These comparisons illustrate several features which are readily apparent on examination of more data of this kind:

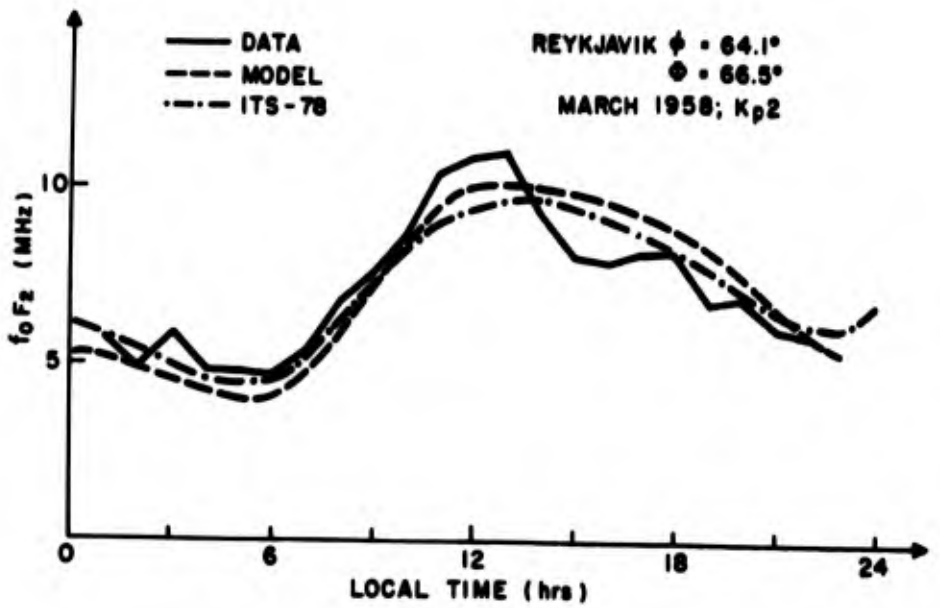

Figure 1-34. Comparison of f_oF_2 Model and ITS-78 Model With Data (Reykjavik, March 1958)

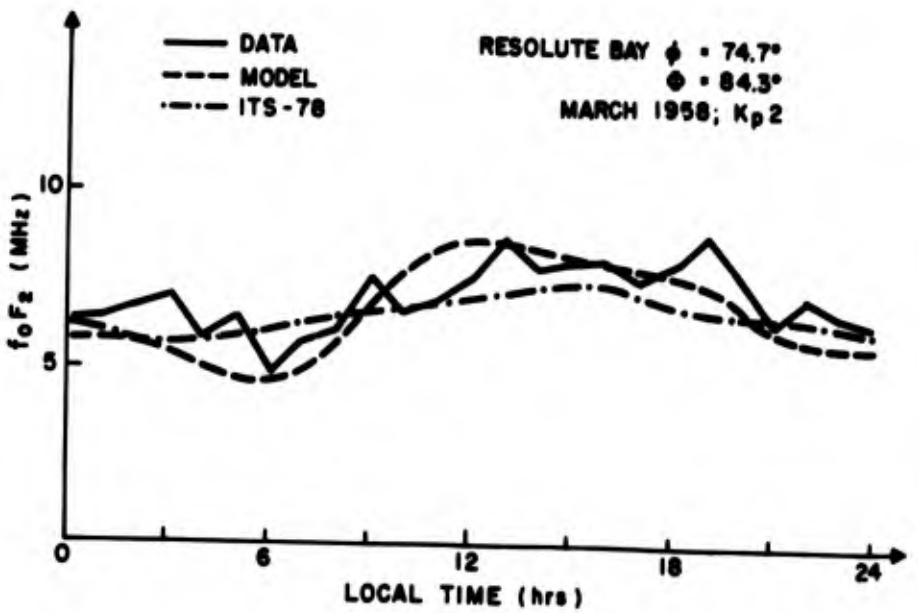

Figure 1-35. Comparison of f_oF_2 Model and ITS-78 Model With Data (Resolute Bay, March 1958)

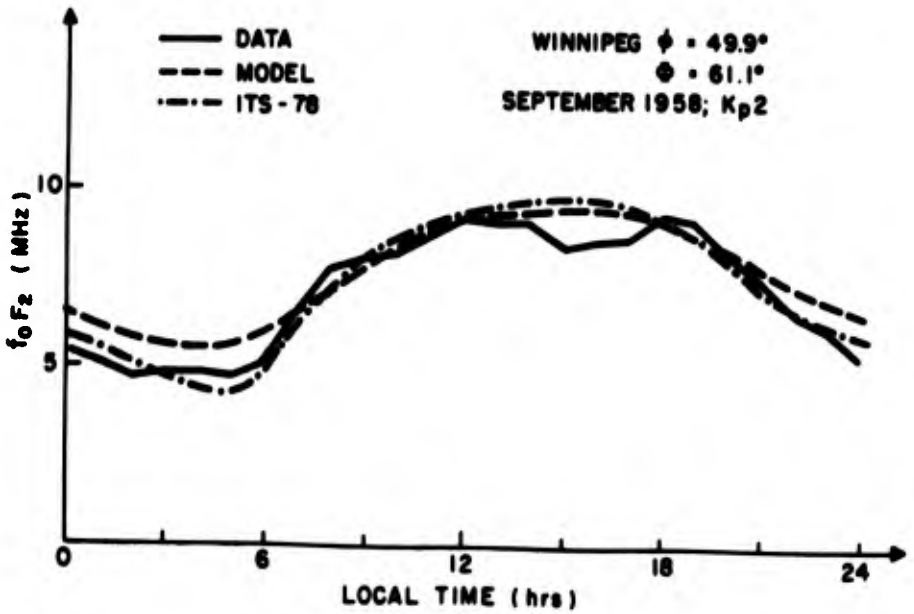

Figure 1-36. Comparison of f_oF_2 Model and ITS-78 Model With Data (Winnipeg, September 1958)

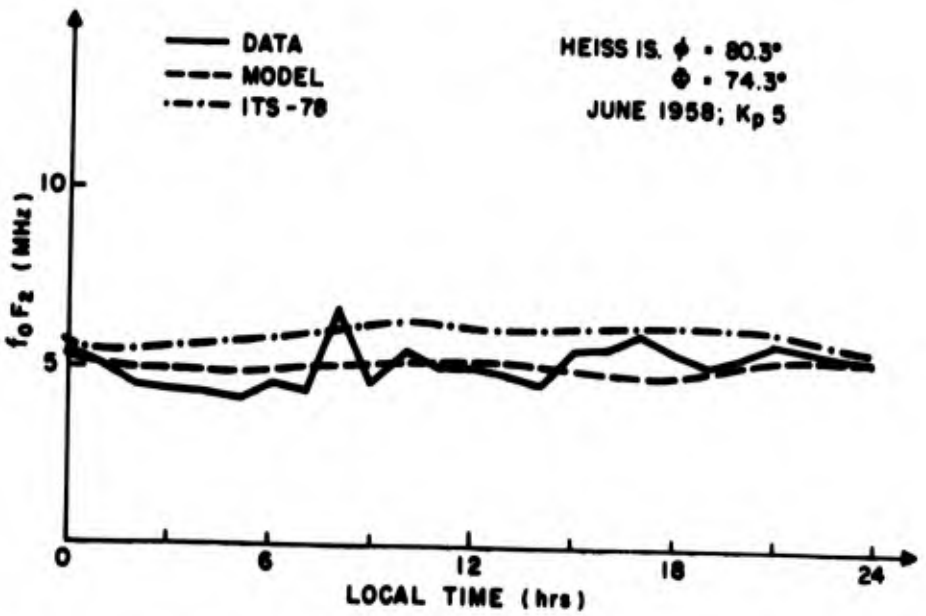

Figure 1-37. Comparison of f_oF_2 Model and ITS-78 Model With Data (Heiss Island, June 1958)

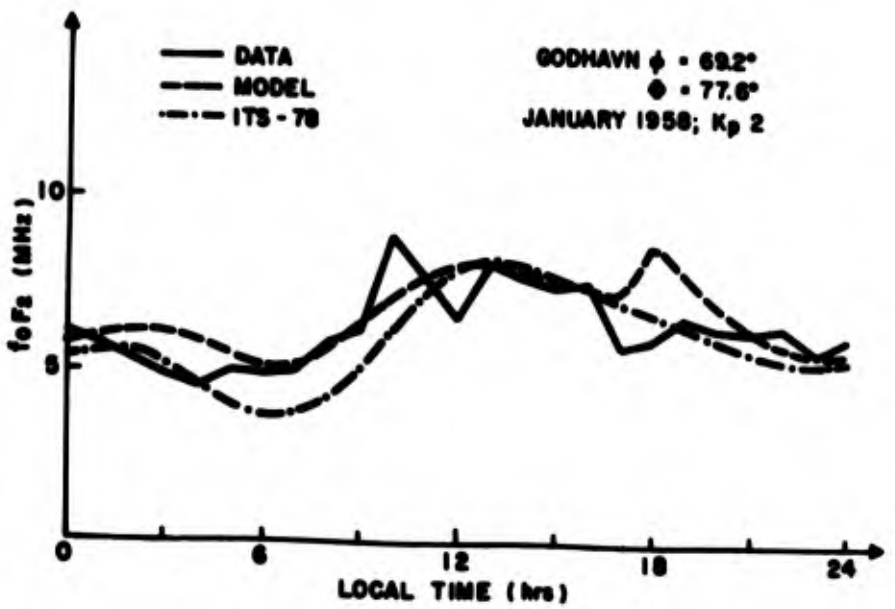

Figure 1-38. Comparison of f_oF_2 Model and ITS-78 Model With Data (Godhavn, January 1958)

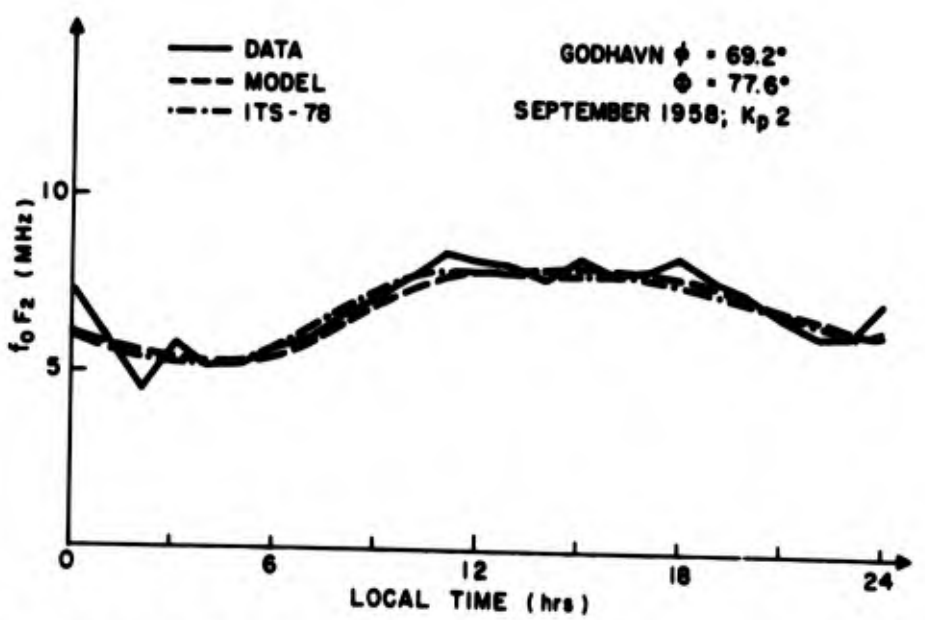

Figure 1-39. Comparison of f_oF_2 Model and ITS-78 Model With Data (Godhavn, September 1958)

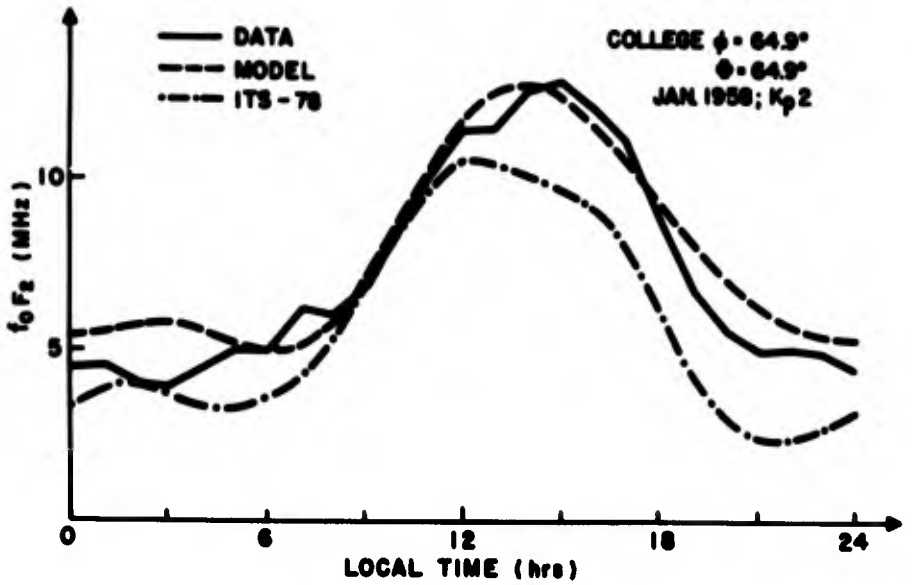

Figure 1-40. Comparison of f_oF_2 Model and ITS-78 Model With Data (College, January 1958)

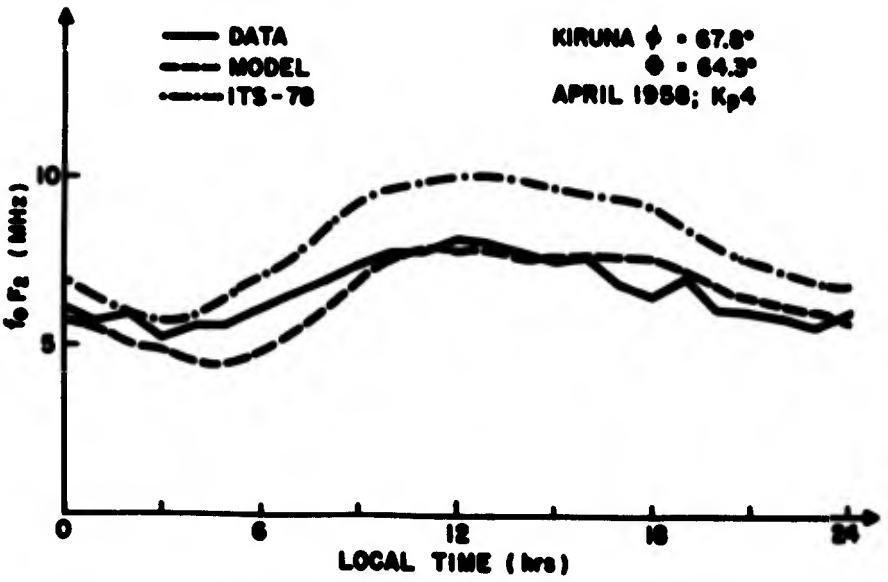

Figure 1-41. Comparison of f_oF_2 Model and ITS-78 Model With Data (Kiruna, April 1958)

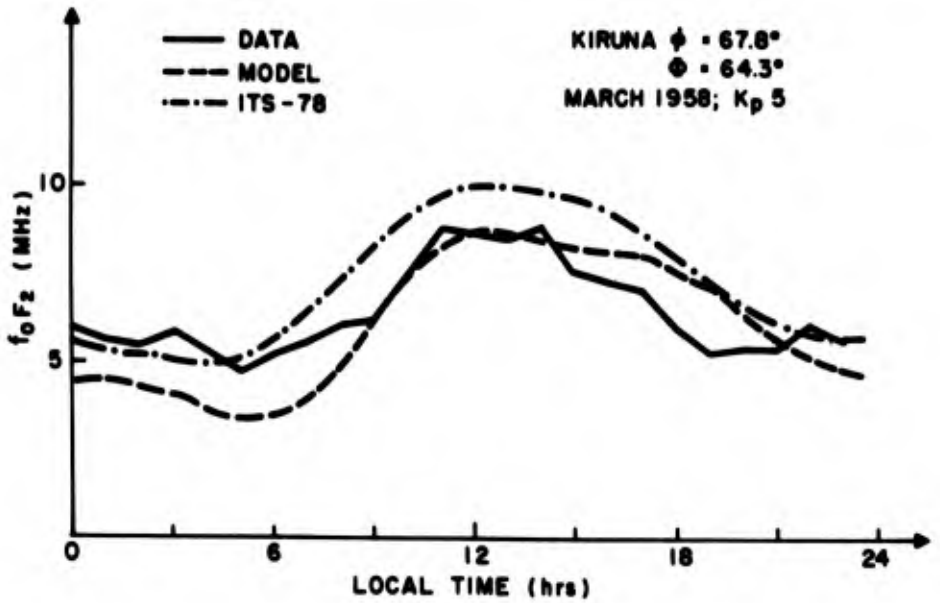

Figure 1-42. Comparison of f_oF_2 Model and ITS-78 Model With Data (Kiruna, March 1958)

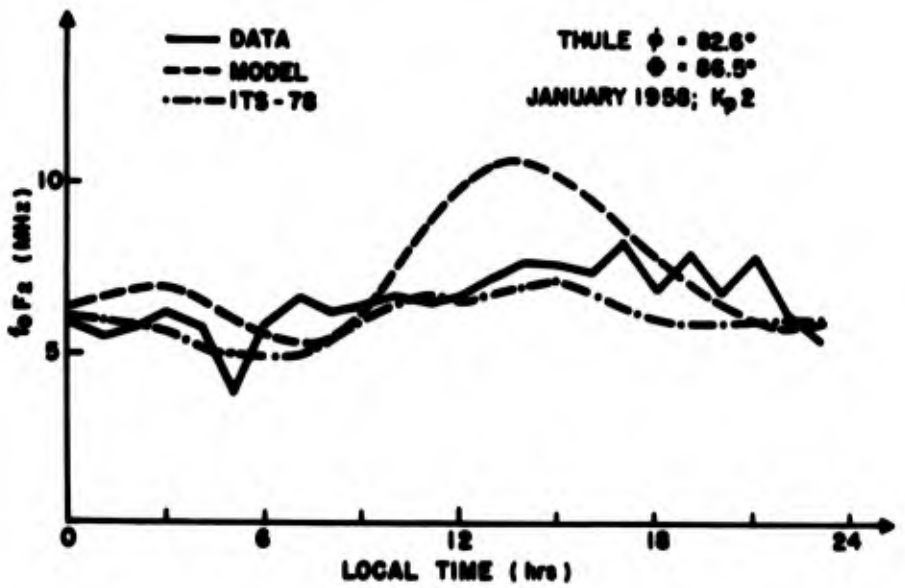

Figure 1-43. Comparison of f_oF_2 Model and ITS-78 Model With Data (Thule, January 1958)

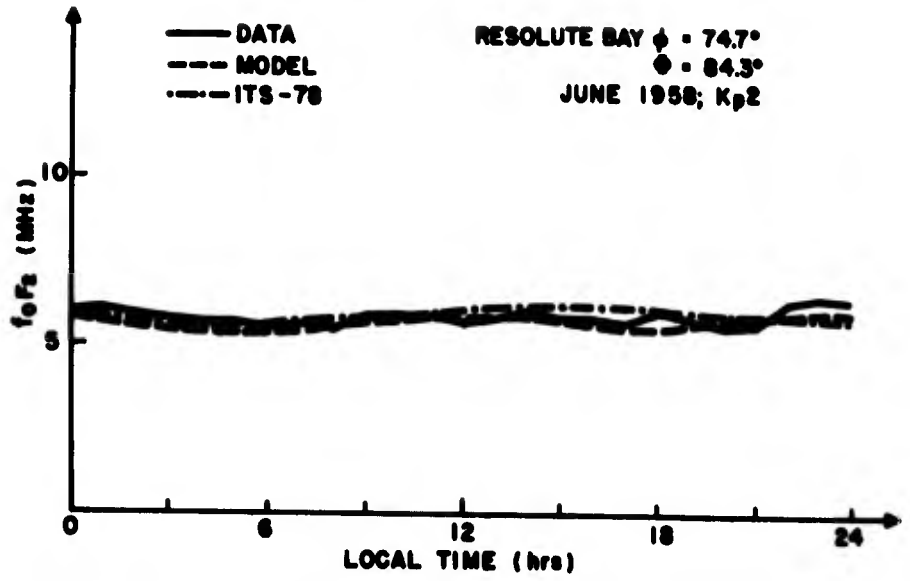

Figure 1-44. Comparison of f_oF_2 Model and ITS-78 Model With Data (Resolute Bay, June 1958)

(1) In summer, both models are very good representations of the data.

(2) In winter, the present model is generally a better estimator of the amplitude of the diurnal variation of f_oF_2, while ITS-78 generally reproduces the shape of the diurnal variation better. The latter is a result of the use of a large number of terms in the diurnal representation by ITS-78. Both models are least "accurate" in winter, when the variability of f_oF_2 is much greater than in summer.

(3) As K_p increases, the present model performs better with respect to the data than does ITS-78. This is due to the fact that ITS-78 is based on median data, and the median magnetic index for which data were obtained in 1958 was probably less than 2 (median K_p was slightly greater than 2 in 1958, but considerable data are lost for high magnetic indices).

Figures 1-45 and 1-46 show, respectively, contours of f_oF_2 from the present model and for ITS-78 for the month of January 1958, when the magnetic index is 5, and UT = 8. The projection used here is a cylindrical one, with the cylinder tangent to the earth at the geographic pole. Figure 1-47 shows the earth in this same projection, and Figure 1-48 shows the latitude-longitude grid at UT = 8, all on the same scale. The location of the ionosonde stations used in this analysis are shown in Figures 1-47 and 1-48 as triangles. The present model is seen to exhibit considerably more small scale structure than ITS-78. Figure 1-49 shows the result from the present model for June 1958, at OUT and for K_p = 3. The strong solar control is evident in Figure 1-49, where the sun is above the horizon for the entire day at latitudes above about 67^o.

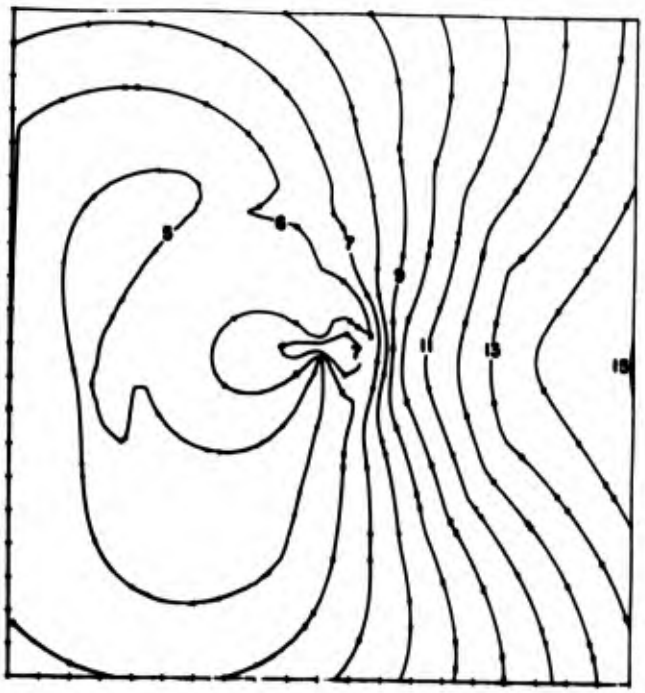

Figure 1-45. Contours of Modeled f_oF_2 (MHz) for January 15; K_p = 4; Sunspot No. = 189; UT = 8. See Figures 1-47 and 1-48 for clarification of the projection

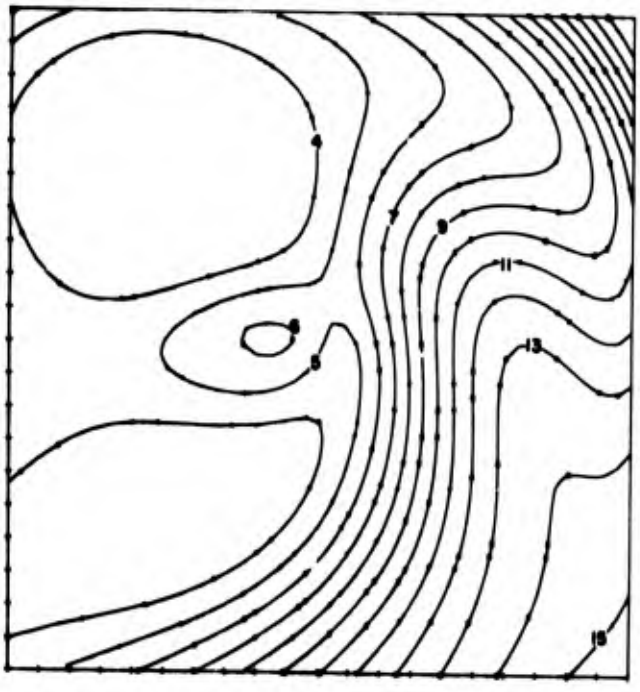

Figure 1-46. Contours of f_oF_2 (MHz) Modeled by ITS-78 Model

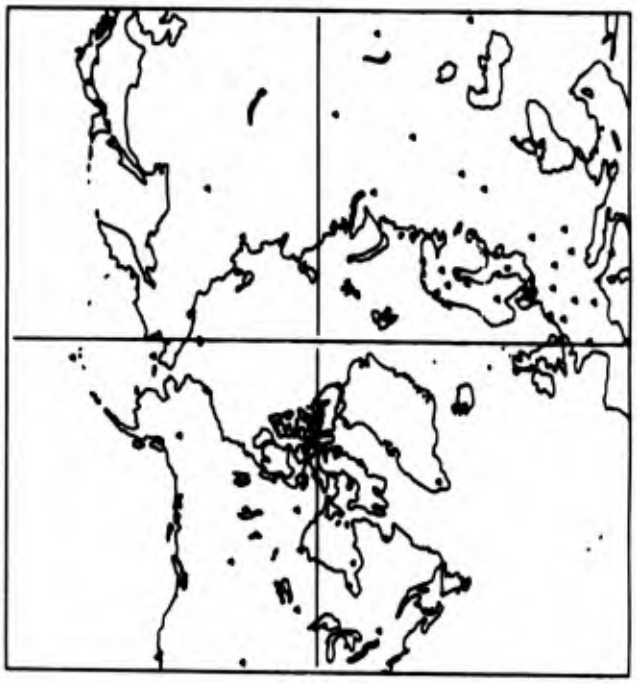

Figure 1-47. Top of the World Projected Onto a Cylinder Tangent to the Earth at the Geographic Pole. Triangles represent ionosonde locations (1958)

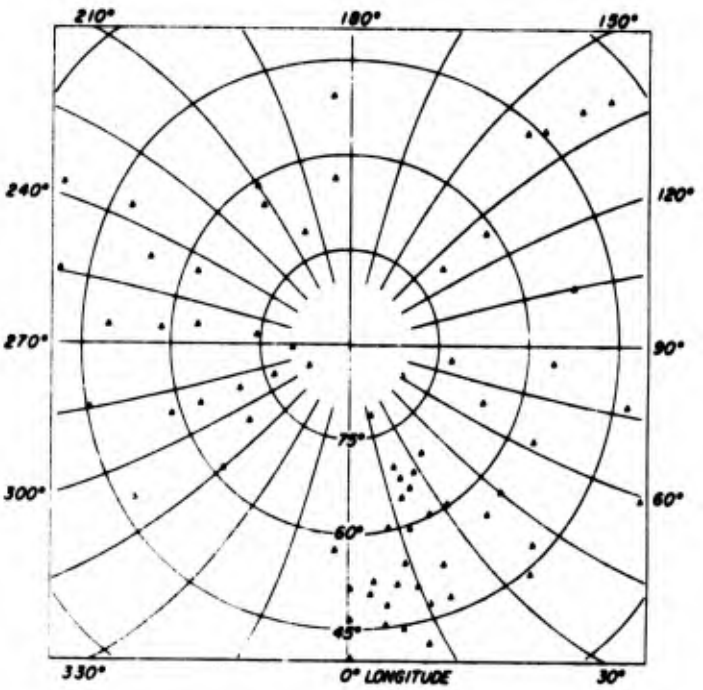

Figure 1-48. Latitude-longitude Grid at OUT for Figures 1-45, 1-46, and 1-47. Triangles represent ionosonde locations (1958)

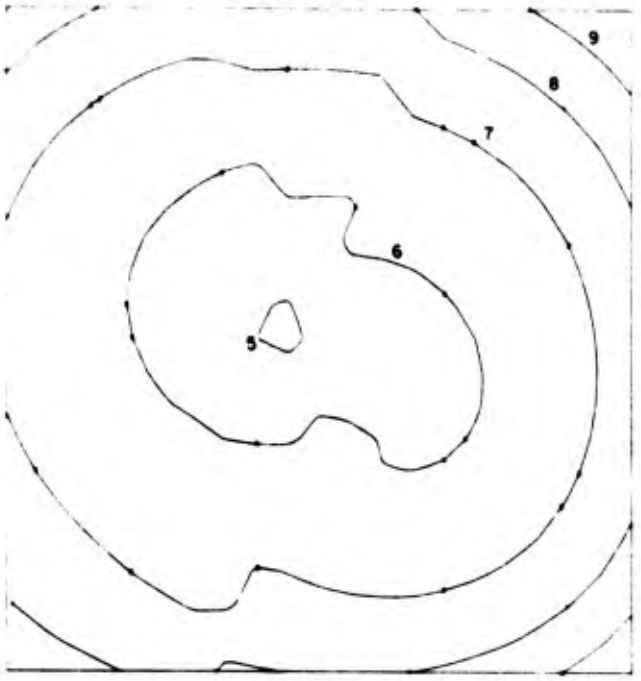

Figure 1-49. Contours of Modeled f_0F_2 (MHz) for June 15; K_p = 3; Sunspot No. = 189; UT = 0. See Figures 1-47 and 1-48 for clarification of the projection

1-5. VERTICLE PROFILE–E- AND F-REGIONS

The shape of the vertical electron density distribution is accurately represented by a superposition of two Chapman layers with a quadratic loss process, at least up to the F_1-peak. At the F_1-peak and above, the linear loss process rapidly begins to dominate the ionization balance. The alpha-Chapman profile is represented by

$$N = N_o \exp \frac{1}{2} (1 - z - e^{-z} \sec \chi)$$

where N_o is the electron density at the peak of the layer at $\chi = 0$;

$$z = \frac{h-h_{max}}{H}$$

where h = altitude (h_{max} = height of the maximum ion production), and H = scale height. H is a function of altitude such that

$$H = 10 + 0.4 (h-100) \text{ km}$$

$$= 0.4h - 30 \text{ km}$$

in the altitude range 100 - 200 km (where h is measured in km). N_o is obtained, for each layer, from the individual models for f_oE and f_oF_1, with the levels z = 0 in each case being chosen to match the modeled heights of these layers.

The profile from the F_1-peak up to the F_2-peak does not conform to a simple Chapman layer shape, since convection, diffusion and electromagnetic drift effects are present in addition to photochemical production and loss processes. The shape of the profile in this interval has been represented by an analytic function which possesses the following specific properties:

(1) Electron densities at hF_1 and hF_2 are those given by the respective f_oF_1 and f_oF_2 models.

(2) The vertical gradient of electron density at hF_1 and at hF_2 = 0.

(3) The height integral of the profile equals the bottomside total electron content, obtained from the appropriate model for that parameter, minus the contribution below the F_1 peak.

(4) The profile is monotonically increasing with altitude.

These requirements can be met by a function of the form

$$N(h) = A + B \cos^M \frac{\pi}{2}\left\{\frac{h - h_1}{h_2 - h_1}\right\}$$

where

$h_1 = hF_1$, and

$h_2 = hF_2 = h_{max}F_2$.

Condition (3) above may be applied, to a first approximation, as follows:

Assume that the E- and F_1-layers have constant scale heights of 20 and 45 km, respectively. Then it can be shown, by integrating the Chapman profiles, that the total electron content below the peak of the F_1 layer is

$$T_B = 4.133 \times 20 \times 10^5 \times N_{max}E + 1.312 \times 45 \times 10^5 \times N_{max}F_1$$

$$= 7.32 \times 10^{10} \times (f_oF_1)^2 + 1.03 \times 10^{11} \times (f_oE)^2 \ .$$

Thus the value of

$$\int_{h_1}^{h_2} \left[A + B \cos^M \frac{\pi}{2}\left\{\frac{h-h_1}{h_2-h_1}\right\} \right] dh$$

must equal the total bottomside content, $(TEC)_B - T_B$.

1-5.1 Nighttime Profile

The above formulation is, of course, only valid when E- and F_1-layers are present; that is, for solar zenith angles less than 90^o. In this case, it is found in practice that the contribution of the total content of the E- and F_1-layers is about 10 to 15 percent of the total bottomside content, in typical cases. At nighttime, another and simpler procedure may be used. It has been found in practice that the nighttime profile can be represented reasonably accurate by a "biparabolic" profile of the form

$$N(h) = N_m \left\{ 1 - \frac{(h-h_{max})^2}{y_b^2} \right\}^2 .$$

This is a convenient expression for certain applications, since it avoids an artificial discontinuity at the base of the layer which is obtained, for example, with a parabolic layer.

The semithickness of the biparabolic layer is related to the total electron content on the bottomside by the expression

$$y_b = 1.875 \frac{(TEC)_B}{N_m} .$$

1-5.2 Topside Vertical Profile

It is a readily observable fact that the electron density variation, over a small altitude range in the topside ionosphere, may be represented quite accurately by a function of the form

$$N(z) = N(z_o) \exp - \frac{z-z_o}{H} . \qquad (1-10)$$

This profile is to be expected on the basis of the theory of an isothermal ionosphere in diffusive equilibrium. If the electrons and ions are in thermal equilibrium, the parameter H may be identified with twice the scale height of the mean ionic constituent:

$$H = \frac{2kT_i}{m_i g} \qquad (1-11)$$

where

k = Boltzmann's constant

T_i = ionic kinetic temperature

m_i = ionic mean mass

g = acceleration due to gravity.

More generally, if the plasma is not in thermal equilibrium, but $T_e = BT_i$ where T_e is the electron kinetic temperature, then

$$H = \frac{k(1+B)T_i}{m_i g} \quad . \tag{1-12}$$

In the real ionosphere, of course, none of the above assumptions regarding diffusive and thermal equilibrium are satisfied. In particular, conditions in the polar ionosphere will often be far from equilibrium, with large convective motions and thermal energy inputs constantly changing. Nevertheless, the above theoretical considerations are helpful in arriving at a reasonably simple empirical specification of the topside profile of the polar ionosphere.

Since the true height data file is reduced to electron density values at 100-km intervals, from 350- to 950-km altitude, it would be possible to construct a series of models for each 100-km interval, of the type satisfying Eq. (1-10), resulting in a sequence of slab models of the ionosphere. This procedure may give the best fit model to the actual data, but is undesirable for three reasons:

(1) It allows discontinuities at the slab boundaries, which may be undesirable for certain applications (for example, ray tracing).

(2) It tends to ignore the correlation between fluctuations in electron density at different altitudes.

(3) It results in a large number of numerical coefficients.

Therefore, a method was devised for constructing a smooth analytic function which best fits the data over the entire range 350 to 950 km. This model, while overcoming the above difficulties, is somewhat limited in the sense that it cannot accurately reproduce large changes in the vertical gradient, such as are observed at the altitude where the major ionic constituent changes from atomic oxygen to helium. Therefore, a second model has been introduced as an alternative, in which the actual profile is approximated, over the entire altitude range, by two exponential functions of the type in Eq. (1-10)—one extending from 350 to 650 km, and the second from 650 to 950 km. These profiles will now be discussed.

1-5.2.1 ANALYTIC PROFILE

It is assumed that the electron density distribution at 350 km is available from a suitable model, similar to that described in Section 1-4.3, for f_oF_2. Alternatively, the electron density at 350 km, or at any other convenient height above the F-layer peak can be determined from the f_oF_2 model or from an ionosonde measurement, by analytic extension around the peak; for example, using a Chapman function or a parabolic function, or as shown in Section 1-5.1, a biparabolic function. Then it is required to find an analytic function, possibly containing several geophysical parameters, to "extrapolate" this model to any other altitude between 350 and 1000 km. The first step was to take the 38,000 profiles on the data file and fit functions of the type in Eq. (1-10) between every adjacent pair of points at 100 km-intervals. Having done this, the average "scale height" H(z) was determined as a function of altitude. This vertical profile of effective scale height may be approximated by a linear altitude function, or more accurately, by a parabolic function. In either case, the actual vertical electron density profile may be reconstructed by integrating Eq. (1-10) in the form

$$N = N_o \exp \left\{ \int_{z_o}^{z} \frac{d\xi}{H(\xi)} \right\} . \tag{1-13}$$

If

$$H(z) = az^2 + bz + c \tag{1-14}$$

then Eq. 1-13 gives

$$N = N_o \exp - \zeta \left\{ \tan^{-1} \left[\zeta \left(az+\tfrac{b}{2}\right) \right] - \tan^{-1} \left[\zeta \left(az_o+\tfrac{b}{2}\right) \right] \right\} \tag{1-15}$$

where

$$\zeta = \frac{2}{\sqrt{4ac-b^2}} . \tag{1-16}$$

If

$$H(z) = fz + g, \tag{1-17}$$

then Eq. (1-13) gives

$$N = N_o \left\{ \frac{z - z_{H=0}}{z_o - z_{H=0}} \right\}^{1/f} \qquad (1\text{-}18)$$

where

$$z_{H=0} = -g/f .$$

Analysis of the Alouette data shows that Eqs. (1-14) and (1-15) are valid over the height range $350 < z < 1000$ km, at least near solar minimum conditions, while Eqs. (1-17) and (1-18) are valid over the range $550 < z < 1000$ km. The expression in Eq. (1-15) will henceforth be taken to represent the topside vertical profile. This representation has a number of built-in advantages. It is apparent that, as $z \to \infty$, N approaches a constant value $\sim N_o e^{-\zeta}$, which reproduces the observed profile, at least qualitatively, at great altitudes. The degree of curvature of the profile at relatively small distances above the peak density may be controlled by varying the two parameters, a and ζ.

These variable parameters have been examined in an attempt to model the shape of the topside profile in terms of the usual geophysical variables. The average values for the Alouette profiles are

$$\zeta = 5.285 \pm 1.1$$

$$a = 3.14 \times 10^{-4}$$

$$b \simeq 0 .$$

By means of multiple regression analysis, however, the variance of these parameters can be reduced. A suitable model may be expressed by writing ζ in the form

$$\zeta = 5.88 - 0.015\,\Phi \cos\chi + 0.41 \cos\frac{2\pi}{365}(D + 11) \sin\phi$$

$$- 0.14\,K_p \quad (\pm 0.93)$$

which is valid over the range 350 to 950 km, with the variables arranged in decreasing order of significance.

An alternative expression which is more accurate, but valid only over the restricted altitude range 350 - 650 km, is as follows:

$$\zeta = 6.40 + 0.47 \cos\frac{2\pi}{365}(D+11) \sin\phi - 0.19\,K_p$$

$$- 0.013\,\Phi \cos\chi - 0.0062\,F_c \quad (\pm 0.88) .$$

Note that the constants in these two expressions are evaluated with Φ measured in degrees. Similar expressions for "a" have been developed, but this parameter apparently is less variable than ζ and in the interests of simplicity of the model, it can be assumed to have its average value, as indicated.

Figure 1-50 shows the comparison of the profile (Eq. 1-15) with an exponential approximation. The profiles are representative of the average of all available high latitude Alouette profiles, and are the best least squares fits to the data, in each case. The electron density scale is normalized to unity at 350-km altitude for the profile obtained with the parabolic scale height variation with altitude.

1-5.2.2 EXPONENTIAL VERTICAL PROFILES

In many cases the formulation based on a parabolic variation of scale height with altitude may be satisfactory. This constraint, however, obscures some significant features which can be brought out by other approximations, at the expense

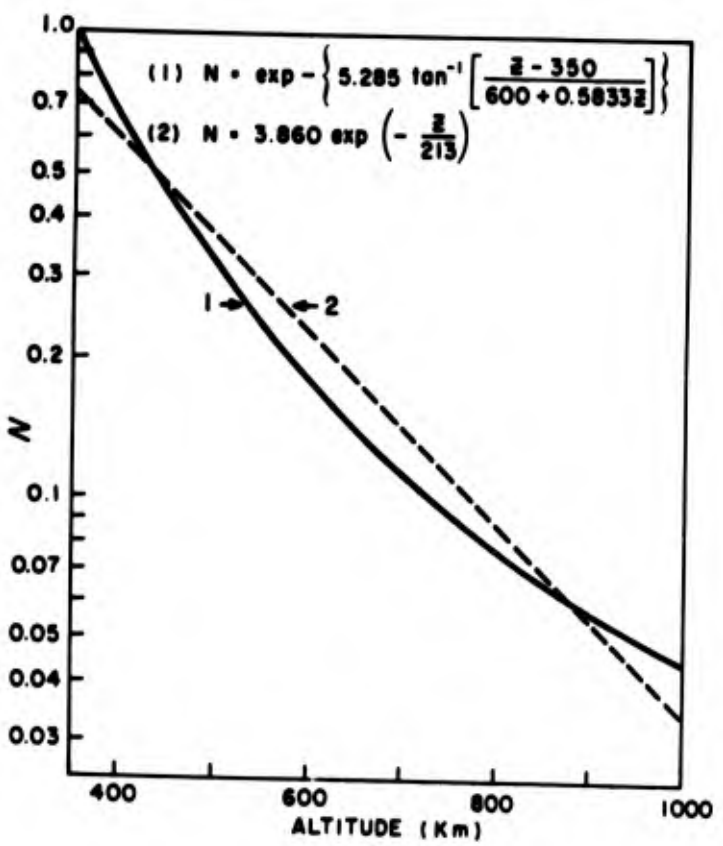

Figure 1-50. Comparison of Normalized Topside Profile for Parabolic Scale Height Variation With Altitude, With Simple Exponential Profile

of losing some of the advantages of the "parabolic" approximation. In particular, a representation of the vertical profile in terms of two exponential functions is useful, although it introduces a discontinuity, which is generally small (1 to 2 percent of the ambient density).

Let the N (z) profile be represented by

$$N(z) = N_{350} \exp k_1 (z - 350) \quad \text{for } 350 < z < 650\text{km}$$

and

$$N(z) = N_{650} \exp k_2 (z - 650) \quad \text{for } 650 < z < 950 \text{ km} .$$

Note that the assumption of an exponential profile extending down to 350 km is only valid for low to moderate solar flux conditions, upon which data the model is based. At solar maximum, particularly at night, this assumption cannot be made.

By using a multiple regression technique with the Alouette true height profiles and experimenting with various forms for the independent variables, the following expressions for k_1 and k_2 were found:

$$k_1 = -0.00779 + 0.0000248\,F + 0.00016\,K_p + 0.00032 \cos \tfrac{\pi}{12}(H_L - 14) - 0.00020 \sin (\tfrac{\pi}{12} H_L) \cos \tfrac{2\pi}{365}(D+11) \qquad \pm 0.001 \text{ km}^{-1}$$

$$k_2 = -0.00350 + 0.00021 \cos \tfrac{\pi}{12}(H_L - 14) + 0.0000123\,F - 0.0000131\,\bar{F} \qquad \pm 0.001 \text{ km}^{-1} .$$

Neither exponential "decay" factor is seen to be significantly dependent on latitude (geomagnetic or geographic). The parameter k_1 is insensitive to $\bar{F}$, the solar flux averaged over the preceding three solar rotations, but is strongly dependent on the current solar flux, F. The shape of the upper half of the range is insensitive to K_p, at least in the range $K_p < 4$, for which this analysis was performed. The profile in the upper range is more variable, by a factor of about 2 in normalized standard deviation, than the lower range. This may be partly due to the lower electron densities in the higher altitudes, with consequently higher experimental "noise" levels.

1-5.2.3 TOPSIDE VERTICAL PROFILES IN TROUGH AND CLEFT REGIONS

The electron density at the lower altitudes in the trough is generally considerably lower than that on either side of the trough, and the scale height is also

smaller, implying a faster vertical rate of decrease with altitude within the trough. The average scale height in the central trough region, for low to moderate levels of magnetic acticity ($K_p < 4$) at the equinox, is given by

$$H(z) = 124.1 - 0.111\ z + 0.000377\ z^2 \quad \text{km}.$$

Thus $\zeta = 4.78$, and $(a\ \zeta)^{-1} = 555$ km.

There does not appear to be a significant diurnal variation in the average shape of the topside trough profile. The electron density in the region immediately surrounding the ionospheric projection of the magnetospheric cleft appears to decrease more slowly with altitude, on the average, than elsewhere. The variability in this region, however, is also much greater than elsewhere, particularly at the higher altitudes. The standard deviation (normalized to the mean) is 2 to 3 times greater in this region, and the scale height in the vertical direction is usually not well represented by a parabola. A rough approximation to the vertical variation of average scale height for the cleft projection is

$$H(z) = 144 + 0.31\ (z-350) + 0.00028\ (z-350)^2 \quad \text{km}.$$

Thus $\zeta = 7.8$, and $(a\ \zeta)^{-1} = 455$ km.

It is important to note that both the trough and cleft features are magnetic field aligned, and thus the geomagnetic latitude of the vertical projection of each varies with altitude. This can amount to several degrees variation over 1000-km height range for the nightside trough, but is considerably less on the dayside where the field lines are more nearly vertical.

1-5.3 Topside Slab Thickness (S_T)

The topside slab thickness is defined as

$$S_T = \frac{(TEC)_T}{N_m}$$

where

$(TEC)_T$ = total electron content between h_{max} and 1000 km

N_m = peak electron density

h_{max} = height of peak electron density.

For $K_p < 5$, S_T may be represented by

$$S_T = 184 - 32 \cos \frac{2\pi}{365}(D+11) \sin \phi - 120 \cos \Phi + 1.4 \times 10^{(K_p/4+0.4)} + 0.50\, F_c - 5.8 \cos \frac{\pi H_L}{12} \pm 39$$

where the units of S_T are in km.

Note that this result is derived from data which is heavily concentrated around solar minimum. In this case, as in all other results following from the Alouette data analysis, the solar flux dependence is determined over a restricted range and becomes more uncertain as solar maximum is approached. The topside slab thickness is seen to decrease with solar flux and with magnetic activity. The variables are arranged in the expression as decreasing order of influence, the most significant being the combined seasonal and geographic latitude variable, which implies that the slab thickness is minimum in winter at the geographic pole. The magnetic latitude term implies that the topside slab thickness is greatest over the magnetic pole (all other things being equal). Finally, the diurnal variation is seen to be very weak, with a maximum at local noon.

As is the case for the bottomside slab thickness, the most significant physical variable which influences the topside slab thickness, as well as the shape of the topside profile, is the plasma scale height. The computation of this parameter based on a neutral atmosphere model, however, is not considered to be sufficiently accurate to warrant the additional complexity involved. It is known that the polar wind enhances the mean molecular weight over the polar cap above the value predicted by neutral models, and this fact is borne out by the magnetic latitude term in the expression for S_T. Furthermore, at latitudes below the equatorward edge of the auroral oval, thermal coupling to the conjugate hemisphere causes the topside electron temperature—and therefore the scale height of the plasma—to deviate from values predicted from neutral models. Some analysis has been performed to explore this question, but the results are not yet sufficiently well developed for modeling purposes. As an example of what can be expected, however, the following expression can be used to represent topside slab thickness for geomagnetic latitudes less than 60°:

$$S_T = 0.64\, T_{inf} - 0.33\, (T_{inf})^{*} - 2.1\, N_m \pm 41$$

where N_m is the (modeled) peak F-layer density ($\times 10^{-4}$ cm^{-3}), T_{inf} is the "exospheric" temperature in Jacchia's model ($^{\circ}$K), and $(T_{inf})^{*}$ is the "exospheric temperature" at the magnetically conjugate point. Further analysis of this kind is planned.

1-5.4 Continuity of the Vertical Profile Above the F-layer Maximum

For a bottomside profile given by

$$N_B = N_m \left(1 - \frac{z_1^2}{y_b^2}\right)^2 \tag{1-19}$$

where z_1 is the height measured from the altitude of maximum electron density (N_m) and a topside profile given by

$$N_T = N_o \exp - \left\{\zeta \tan^{-1}\left[\frac{\beta(z-z_o)}{\gamma+z\ z_o}\right]\right\} \tag{1-20}$$

the complete vertical profile is obtained by matching the two profiles with the contraints

$$N_B = N_T \qquad \text{at } z = z_c$$

$$\frac{dN_B}{dz} = \frac{dN_T}{dz} \qquad \text{at } z = z_c$$

where z_c is the altitude at which the profiles match. Thus, z_c is given by the solution of

$$z_c^3 + \frac{\zeta\beta}{4} z_c^2 + \gamma z_c - \frac{\zeta\beta y_b^2}{4} = 0 \tag{1-21}$$

where

$$z_c = z - h_{max}\,.$$

The solution of this equation, for the values of ζ, β and γ which produce the average vertical profile, may be approximated by the following parabolic expression

$$z_c = 0.0007504\ y_b^2 + 0.3257\ y_b - 20.445. \tag{1-22}$$

In the range $100 \le y_b \le 300$, this approximation is accurate to better than 1 km in z_c.

Using Eqs. (1-19) and (1-20), together with the matching condition of Eq. (1-22) guarantees an accurate vertical profile having no discontinuities.

Equation (1-21) expresses the condition that a continuous vertical profile is obtained, subject to the constraint that the topside profile is determined once the electron density at the layer peak (N_m) is fixed. If, however, by some means the electron density at some reference height above the peak (z_o) is known so that the topside model is independent of the N_m model, the matching conditions require that z_c must satisfy

$$z_c^3 \left\{4(z_o^2 + \beta^2)\right\} + z_c^2 \left\{\zeta\beta z_o^2 + 8 z_o (\gamma - \beta^2) + \zeta\beta\gamma\right\}$$

$$+ z_c \left\{4 (\gamma^2 + \beta^2 z_o^2)\right\} - \zeta\beta y_b^2 (\gamma + z_o^2) = 0. \qquad (1\text{-}23)$$

For example, if the reference height, z_o, in terms of which the topside model is expressed (Eq. (1-20)), is set at 350 km, then the parabolic approximation analogous to Eq. (1-22) in this case is

$$z_c = 0.0005864\, y_b^2 + 0.3377\, y_b - 20.293. \qquad (1\text{-}24)$$

1-6. SPORADIC-E MODEL

Sporadic-E in the polar regions is produced primarily by the influx of charged auroral particles. Although the morphology of E_s displays considerable regularity in some respects, the great variability in space and time of the incident particle fluxes requires that E_s be treated as a random variable. In this section the properties and synopsis of E_s will be summarized, and some of its effects upon HF propagation assessed.

Sporadic-E is of primary interest in HF propagation applications, although it is of occasional interest in some more exotic applications, such as VHF forward scatter propagation. The sporadic-E layer is often thin and patchy, causing abrupt, mirror-like reflection as well as partial transmission. The latter phenomenon may result in the "blanketing" condition, in which a sporadic-E layer may shield the overlying ionosphere against transmission from below. This shielding usually occurs at frequencies lower than the "blanketing" frequency (f_bE_s). This frequency (f_b) may be interpreted in terms of a crude model in which the sporadic-E layer consists of patches of enhanced ionization, with small vertical extent, whose average separation is of the order of the wavelength corresponding to f_bE_s.

Sporadic-E is classified into a number of different categories, according to its appearance on vertical incidence ionosonde records. In the polar regions, the principal varieties are:

(1) Auroral E_s (E_{sa})—generally consisting of an amorphous spread of reflections in range and frequency, with the amount of range spread diminishing towards higher frequencies. E_{sa} is usually completely blanketing.

(2) Flat E_s (E_{sf})—consists of a reflection showing uniform height as a function of frequency. E_{sf} is usually blanketing.

(3) Retardation E_s (E_{sr})—shows an increase in virtual height with frequency, similar to group retardation. E_{sr} is usually nonblanketing.

All three types of E_s are usually associated with the presence of visible aurora somewhere in the sky, although E_{sr} may often be associated with quiet diffuse auroras, while E_{sa} and E_{sf} are associated most often with active auroras. If E_s occurrence of all magnitudes is considered, E_{sr} is the most commonly observed variety, being observed approximately twice as frequently as the other types combined. For intense E_s events ($f_oE_s \geq 5$ MHz), however, E_{sa} occurs about as frequently as the other types combined (Eather and Jacka, 1966).

Other types of E_s (Cusp - E_{sc}; high - E_{sh}; low - E_{sl}; slant - E_{ss}) are apparently related to different physical phenomena, such as wind shear. These other types of E_s are similar to sporadic-E occurrence at midlatitudes, and occur usually during the daytime, with relatively low frequency compared to a, f, r types.

1-6.1 Temporal Coherence of E_s

A parameter of considerable interest in HF propagation applications is the distribution of the duration of sporadic-E events of different types. Zherebtsov and Kurilov (1971) found that during disturbed periods the standard ionosounding interval of 15 min is too long to permit this parameter to be estimated accurately from most existing data. If one assumes an exponential differential probability distribution for the duration of E_s events, their data—which was derived from 1-min sounding intervals when aurora was visible in the sky—results in the following "median-lifetimes" of different varieties of E_s:

E_{sa} - ~4 min

E_{sr} - ~4 min

E_{sf} - ~3 min

1-6.2 Spatial Distribution

The great variability of E_s, together with the demonstrated inadequacy of the standard ionosounding schedules, makes the study of spatial distribution of E_s complicated. It was deduced by Sukhorukova (1964), on the basis of hourly data, that the spatial dimension of typical E_s patches corresponded to an area of

3×10^5 to 4×10^5 km^2. This result, however, must be regarded with some caution for the reason mentioned, as well as the variations in the sensitivities of different ionosondes. Nevertheless, the demonstrated high correlation (Montalbetti and McEwen (1962)) between E_s and visible aurora makes for a reasonable assumption that the morphology of E_s is similar to that of visible aurora and may therefore be characterized by the "auroral oval". As demonstrated by Sukhorukova (1964), E_s has a greater characteristic spatial scale than absorption regions, which are known from other studies to have typical dimensions of ~ 1000 km along the auroral oval. Thus we may assume that, on the average at least, E_s occurs continuously around the oval.

1-6.3 Sporadic-E Data Analysis

The parameters of principal interest to radio propagation systems are:

(1) Amplitude probability distributions of f_oE_s, f_BE_s and hE_s.

(2) Correlations between f_oE_s and hE_s and between f_oE_s and f_BE_s. It is required to determine these parameters as functions of time, season, sunspot number, geomagnetic latitude and magnetic activity.

Using hourly scaled values from 50 high latitude stations which were operating during 1958 and 1964, the months March, June, September and December were reduced to digital form and grouped according to the following classifications:

(1) Six K_p Intervals:

0 - 1
1 - 2
2 - 3
3 - 4
4 - 6
6 - 9

(2) Four Magnetic Latitude Intervals:

48^o - 54^o (11 stations)

56^o - 66^o (20 stations)

66^o - 75^o (12 stations)

77^o - 89^o (6 stations)

1-6.3.1 DISTRIBUTION OF f_oE_s

The probability distribution of f_oE_s was determined by sorting the available data into 192 subdivisions (2 years; 4 seasons; 4 latitude ranges; 6 K_p ranges). Within each subdivision, a histogram of f_oE_s was obtained with class intervals:

0 - 2 MHz
2 - 4 MHz
4 - 6 MHz
6 - 8 MHz
>8 MHz

The total number of data points used in the analysis was approximately 20,000.

The distributions for all three parameters were found to be approximately log-normal, with the median and decile range being functions of K_p. No substantial seasonal or solar cycle effects were detected, although there have been isolated reports of these in the literature. The possibility of small effects of this kind cannot be excluded, however, and might be revealed with a larger data base. The latitude dependence of the parameters of the probability distributions was complex, and was observed to be a nonlinear function of K_p. Much of this complexity was eliminated, however, when the data were viewed within the framework of the auroral oval concept. It was found that a considerable degree of order was established by considering separately three different regions:

(1) Polar Cap Region —interior to the auroral oval.

(2) Auroral Region—contained within the high latitude and low latitude boundaries of the auroral oval.

(3) Subauroral Region—exterior to the auroral oval.

The inner boundary of the auroral oval may be represented, for this purpose, by the following analytic expression:

$$\Phi_1 = 70 - 1.8\ K_p \cos \frac{\pi}{12}(H_M - 1)$$

where Φ_1 is the magnetic latitude of the inner boundary at magnetic time H_M (hours). The outer boundary of the auroral oval is similarly represented approximately as

$$\Phi_2 = \Phi_1 + 4\ (1 + 0.25\ K_p)\ .$$

The model for f_oE_s may then be summarized as follows:

Region (1) $\Phi > \Phi_1$

Median = $3.9 - 0.1\ K_p$

Upper Decile = $7.8 - 0.4\ K_p$

Lower Decile = 2.0

Region (2) $\Phi_1 > \Phi > \Phi_2$

Median = $4.0 + 0.05\ K_p$

Upper Decile = $6.6 + 0.2\ K_p$

Lower Decile = $2.2 + 0.03\ K_p$

Region (3) $\Phi > \Phi_2$

Median = 3.0

Upper Decile = 5.3

Lower Decile = 1.6

All units are in MHz.

In the above model, no local time dependence of the parameters of the probability distribution has been indicated. This was found to be supported by the data in regions (1) and (2), but in region (3) there appears to be a noticeable local time effect. This could not be well determined from the data, however, and remains to be established by subsequent analysis with a larger amount of data.

Although the parameters f_bE_s and hE_s were treated independently when determining the probability distributions, rather than model these distributions separately, a simpler procedure was used. It was observed that both parameters are fairly well correlated with f_oE_s, so that simple linear regression analyses were performed for the pairs

f_oE_s - f_bE_s

f_oE_s - hE_s

The regression analyses were performed as a function of geomagnetic latitude (in 10^o ranges), and for sunspot maximum and sunspot minimum separately. However, the results of these analyses are not considered to show any statistically significant latitude or solar cycle effects in the correlation observed, so an average was taken of all of the observed data. The best fit regression lines were found to be

$$f_bE_s = 1.3 + 0.30\, f_oE_s \quad (\pm 0.6)\ \text{MHz}$$

$$hE_s = 117 - 1.13\, f_oE_s \quad (\pm 14)\ \text{km}$$

The numbers in parentheses are the standard errors of the residual distributions.

1-7. PROBABILITY DISTRIBUTION FOR N_mF2 and f_oF2

The peak electron density of the F-layer is a highly variable parameter, and very sensitive to geomagnetic disturbance, solar flares, and charged particle precipitation. The attempts to formulate a deterministic model, which have been described in Section 1-4.3, account for only a part of this variability. The residual variations must be regarded, for the present, as a random quantity, whose properties remain to be specified if the model is to have maximum practical utility. A question which arises here is the time scale on which significant fluctuations in f_oF_2 take place. The ionosonde data was available only at hourly intervals, and it is believed that changes in f_oF_2 occur more rapidly than this in certain regions under certain conditions. Some limited use can be made of the Alouette data in resolving this problem, and an attempt has been made to use both data sets in determining the residual distributions. Some differences have been observed, and this area of the model must presently be considered as incomplete, pending further study.

Figure 1-51 shows the probability distributions for N_mF_2 after subtracting a first order model from Alouette data. The distributions are for the 1200 - 1500 magnetic time sector, and for 10^o intervals of geomagnetic latitude from 40^o to 90^o. Note that the distributions depart significantly from Gaussian for some latitude ranges (a Gaussian distribution on these axes forms a straight line).

In order to specify the actual probability distribution of the residuals, it was decided to express this in terms of an asymptotic expansion of the normal (Gaussian) distribution. Thus if the normal distribution is written as

$$\phi(x) = \frac{1}{\sqrt{2\pi}} e^{-x^2/2}$$

then the actual distribution may be expressed as

$$f(x) = \phi(x) - \frac{\gamma_1}{3!}\phi^{(3)}(x) + \frac{\gamma_2}{4!}\phi^{(4)}(x) + \ldots\ldots$$

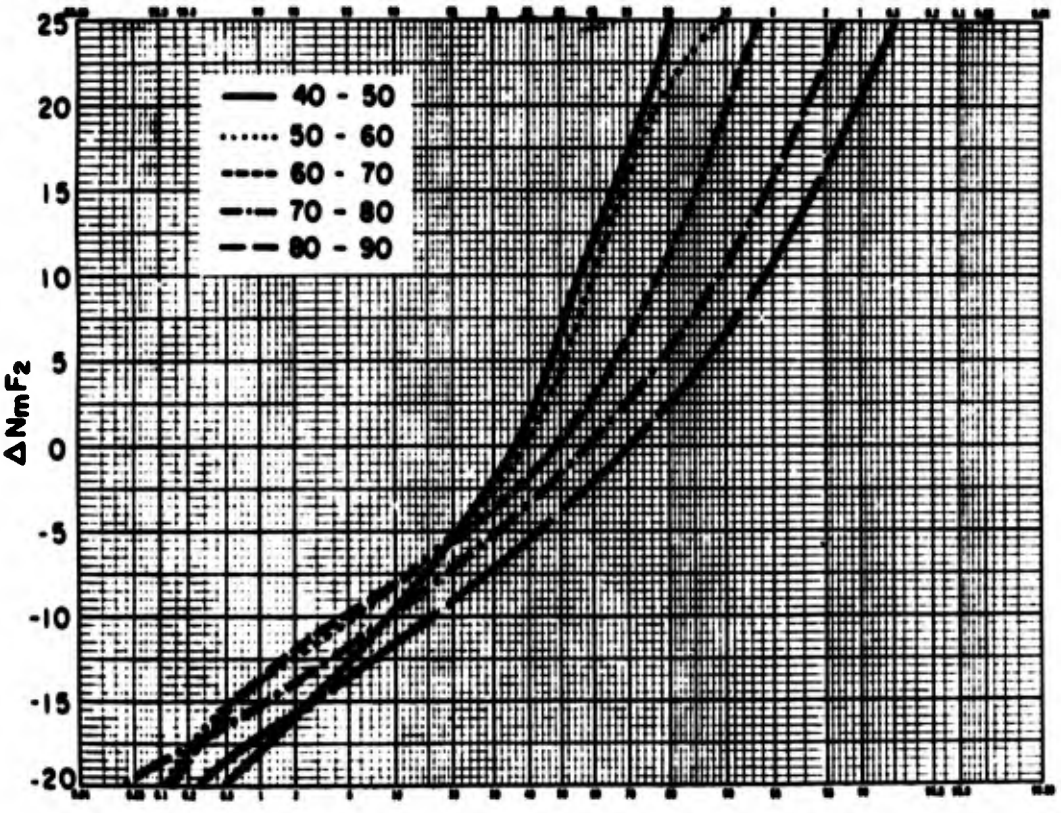

Figure 1-51. Probability Distribution of Deviations of N_mF_2 From a First Order Model for 1200-1500 Magnetic Time, at 10^o Intervals of Magnetic Latitude. Ordinate is the deviation ($\times 10^{-4}$ cm^{-3}); abscissa is the probability (percent) that ordinate is exceeded

where the superscripts denote order of differential coefficient, and γ_1 = coefficient of skewness, γ_2 = coefficient of excess (kurtosis). γ_1 and γ_2 may be expressed in terms of the central moments of the distribution as

$$\gamma_1 = \frac{\mu_3}{\sigma^3}$$

$$\gamma_2 = \frac{\mu_4}{\sigma^4} - 3$$

where σ = standard deviation.

The central moments of the distribution (ν_n) are related to the moments about the origin (μ_n) by

$$\mu_1 = 0$$

$$\mu_2 = \nu_2 - \nu_1^2$$

$$\mu_3 = \nu_3 - 3\nu_2\nu_1 + 2\nu_1^3$$

$$\mu_4 = \nu_4 - 4\nu_3\nu_1 + 6\nu_2\nu_1^2 - 3\nu_1^4$$

For each of the latitude-time intervals used, $\nu_n (n=1, 4)$ was determined from data residuals as

$$\nu_n = \frac{1}{N} \sum_{i=1}^{N} \chi_i^n$$

and the coefficients of skewness and excess were then computed using the above relationships. The results were then fitted with smooth contours, resulting in Figures 1-52 through 1-54. Note that Figure 1-52 is a representation of the interdecile range, rather than standard deviation, as this is a more commonly used radio propagation parameter. The standard deviation is related to the interdecile range by

$$\sigma = 0.3906 \text{ (UD-LD)}.$$

The ionosonde data was treated similarly to the Alouette data, except that the monthly mean f_oF_2 value was subtracted from the hourly values at each station before computing the distributions of the residuals. Figures 1-55 through 1-58 show examples of the skewness of the distributions, contoured on a grid of geomagnetic latitude and geomagnetic time. Geographic coordinates were also tried, but it was noted that several features (such as the nightside auroral oval) show up clearly in the presentation selected. The distribution is seen to be much more asymmetric and more variable over the polar cap in winter than in summer, which is borne out in other analyses.

It should be pointed out that this analysis should properly be done with K_p as a variable, since the deterministic model is defined with K_p as a parameter. Presumably, the distribution would show less variance and be less skewed if this were done. The available data were insufficient to permit this, however, and the results shown should be used only in relation to median conditions, with no magnetic activity effect included. This statistical analysis is continuing, and will be the subject of a further report.

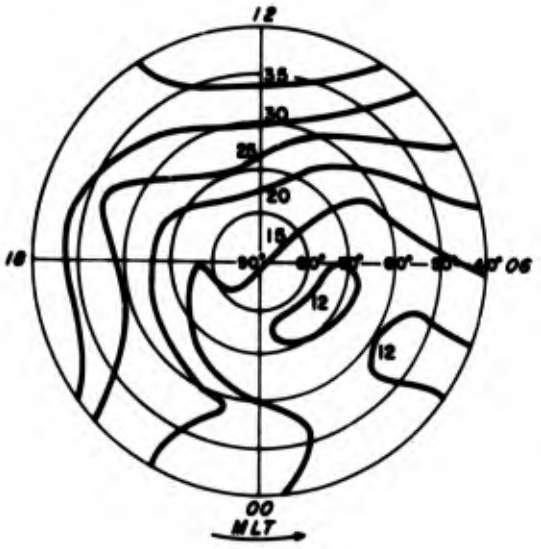

Figure 1-52. Decile Range of the Residual Distribution in Figure 1-51 (Alouette 1, 1963)

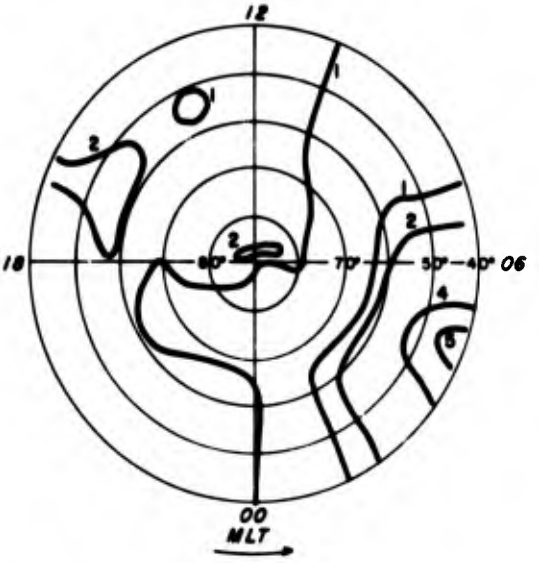

Figure 1-53. Skewness Coefficient for Distribution in Figure 1-51

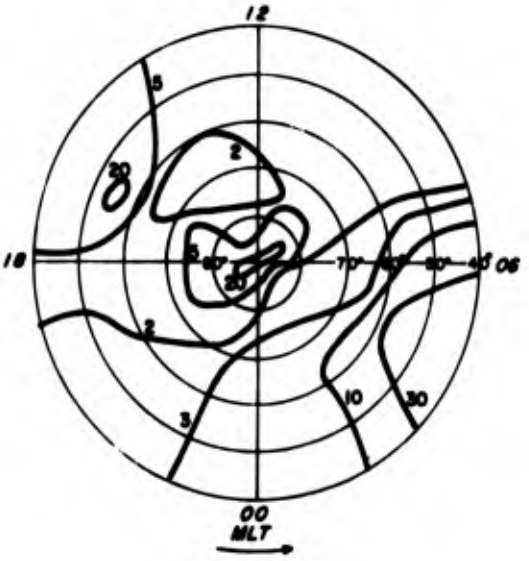

Figure 1-54. Excess Coefficient for Distribution in Figure 1-51

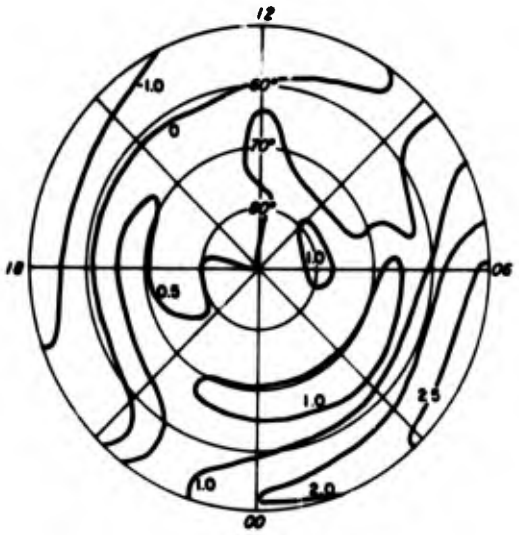

Figure 1-55. Skewness for Distribution of Hourly f_oF_2 Values, in Corrected Geomagnetic Coordinates (March, 1958)

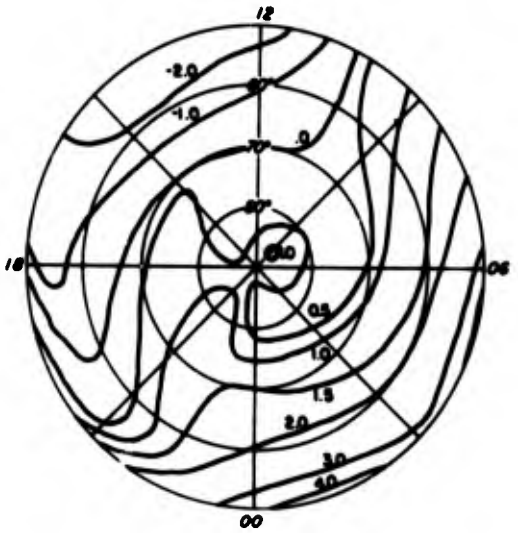

Figure 1-56. Skewness for Distribution of Hourly f_oF_2 Values, in Corrected Geomagnetic Coordinates (December, 1958

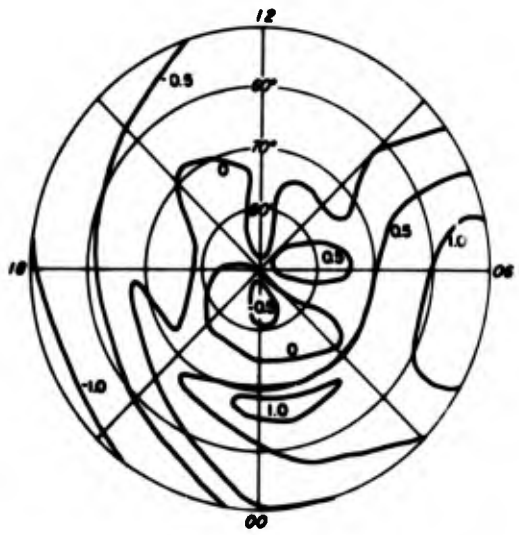

Figure 1-57 Skewness for Distribution of Hourly f_oF_2 Values, in Corrected Geomagnetic Coordinates (September, 1958

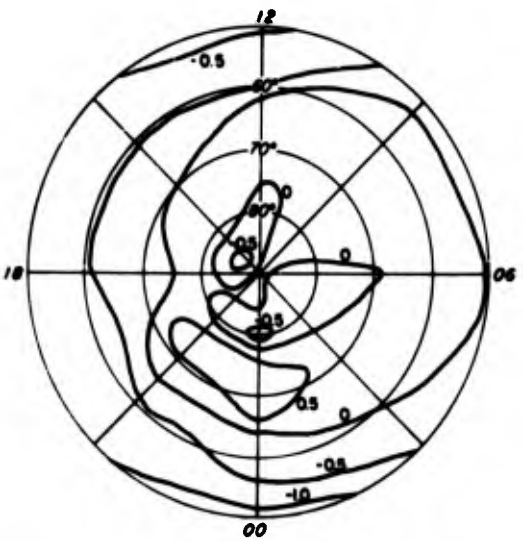

Figure 1-58. Skewness for Distribution of Hourly f_oF_2 Values, in Corrected Geomagnetic Coordinates (July, 1958)

1-8. MUF PROBABILITY DISTRIBUTION

For an obliquely propagated signal, it is usually desirable to establish the statistical distribution of the maximum usable frequency (MUF). For a simplified plane earth and ionosphere model, the MUF is given by the following relationship:

$$\begin{aligned} \text{MUF} &= f_o X \cdot \sec I \\ &= f_o X \cdot \frac{\mathcal{R}}{2h} \end{aligned}$$

where

$f_o X$ is the layer critical frequency ($X = F_2$, F_1, E, or E_s)

I is the angle of incidence

h is the height of the layer

$\mathcal{R}$ is the propagation range

In the case of a spherical earth and ionosphere model, the above relationship is only approximately valid, but the difference between plane and spherical geometry will not be of major significance in the following discussion.

In general, $f_o X$ and h are random variables which may be partially correlated. Thus MUF is a random variable, whose statistics may be derived from those of $f_o X$ and h, determined from a model of these parameters. If the joint probability density of $f_o X$ and h is $p(\chi, y)$, then the probability density of $f_o X/h$ is (Gnedenko, 1967),

$$p(\chi) = \int_o^\infty z p(z\chi, z)dz - \int_{-\infty}^o z\, p(z\chi, z)dz$$

For example, if both $f_o X$ and h are normally distributed, with standard deviations normalized to the mean of σ_1 and σ_2 and with correlation r

$$p(\chi) = \frac{\sigma_1 \sigma_2 \sqrt{1-r^2}}{\pi(\sigma_2^2 \chi^2 - 2r\sigma_1\sigma_2\chi + \sigma_1^2)}$$

where χ = MUF

If f_oX and h are independent ($r = 0$), this reduces to the Cauchy probability density:

$$p(\chi) = \frac{\sigma_1\sigma_2}{\pi(\sigma_1^2 + \sigma_2^2\chi^2)} .$$

The distribution function for this density is

$$P(\chi<\chi_o) = \frac{1}{2} + \frac{1}{\pi}\tan^{-1}\frac{\sigma_2}{\sigma_1}(\chi - \overline{\chi})$$

where $\overline{\chi}$ is the median MUF. The upper and lower deciles of the Cauchy distribution are located at

$$\overline{\chi} \pm 3.0777\frac{\sigma_1}{\sigma_2} .$$

In contrast, if as is sometimes assumed, the MUF is normally distributed with standard deviation σ_m, then the upper and lower deciles are located at

$$\overline{\chi} \pm 2.56\,\sigma_m .$$

In actuality, both the Cauchy and normal distributions are only rough approximations to the distribution of MUF, although the former is probably a better representation of the true situation, since f_oX and h are only poorly correlated in reality. A more serious objection to the Cauchy distribution arises, however, in the case of propagation via the F_2-layer ($X = F_2$), where the probability density of f_oF_2 is often markedly non-Gaussian, especially in the polar regions. It has been found, in the past, that a convenient distribution to use in representing f_oF_2 variations about the mean is the Chi-squared distribution. If f_oX is assumed to have a Chi-squared distribution, and h to have a normal distribution, then the distribution of MUF can again be evaluated in closed form. This will form the subject of a separate report.

1-9. F-REGION IRREGULARITIES

Although the high latitude ionosphere is highly irregular on a small spatial scale, certain patterns in the distribution of small scale F-region irregularities can be observed. Penndorf (1960) showed that the temporal and spatial distribution of these high latitude irregularities can be considered as a combination of

a region of enhanced occurrences near the magnetic pole, which varies little in time, and a moving maximum which in retrospect appears to be located in the midnight sector of the auroral oval. Similar conclusions may be reached by studying the morphological distributions of Spread-F producing irregularities published by Tao (1966). There are well-defined seasonal and solar cycle dependences in the percentage occurrence of Spread-F, even though the parameter itself is not precisely measurable, being usually estimated by visual examination of ionosonde records.

Spread-F is also observed by topside sounders (Alouette 1 and 2, ISIS), and the morphology of topside ionospheric irregularities is found to be somewhat different from that of bottomside irregularities. The most obvious difference is the greater percentage occurrence of topside irregularities, but there are also differences in the space-time distribution. Irregularities are also observed by their effect upon VHF signals propagated through the ionosphere, from a satellite to a ground receiver. Scintillations thus imposed on the propagating signal are a measure of the integrated irregularity distribution along the ray path. The precise determination of irregularity distribution from the scintillation amplitude is a complex task, involving diffraction theory, and has no unique solution. Generally speaking, the scintillations are caused by irregularities near the peak of the F-layer and above, roughly in proportion to the ambient or background electron density. The irregularities contributing to the generation of scintillations are those having a scale approximating the first Fresnel zone size (normally, several kilometers).

1-9.1 Spectrum of Irregularity Size

The size distribution of F-region irregularities has been determined by spectral analysis of the scintillation of satellite signals (Elkins and Papagiannis, 1969) and of direct plasma probe measurements (Dyson, 1973; Phelps, 1973). In the polar ionosphere, it appears that this distribution may be best represented by a power law

$$P(x) \sim x^{q}$$

where x is the characteristic size associated with the electron density fluctuation (assumed isotropic) and

$$q \sim 2.0 \pm 0.5 .$$

Figure 1-59 shows a typical power spectrum of the scintillation of the VHF signal from a geostationary satellite, observed at a subauroral location. The natural logarithm of the spectral power density is shown as a function of frequency (Hertz).

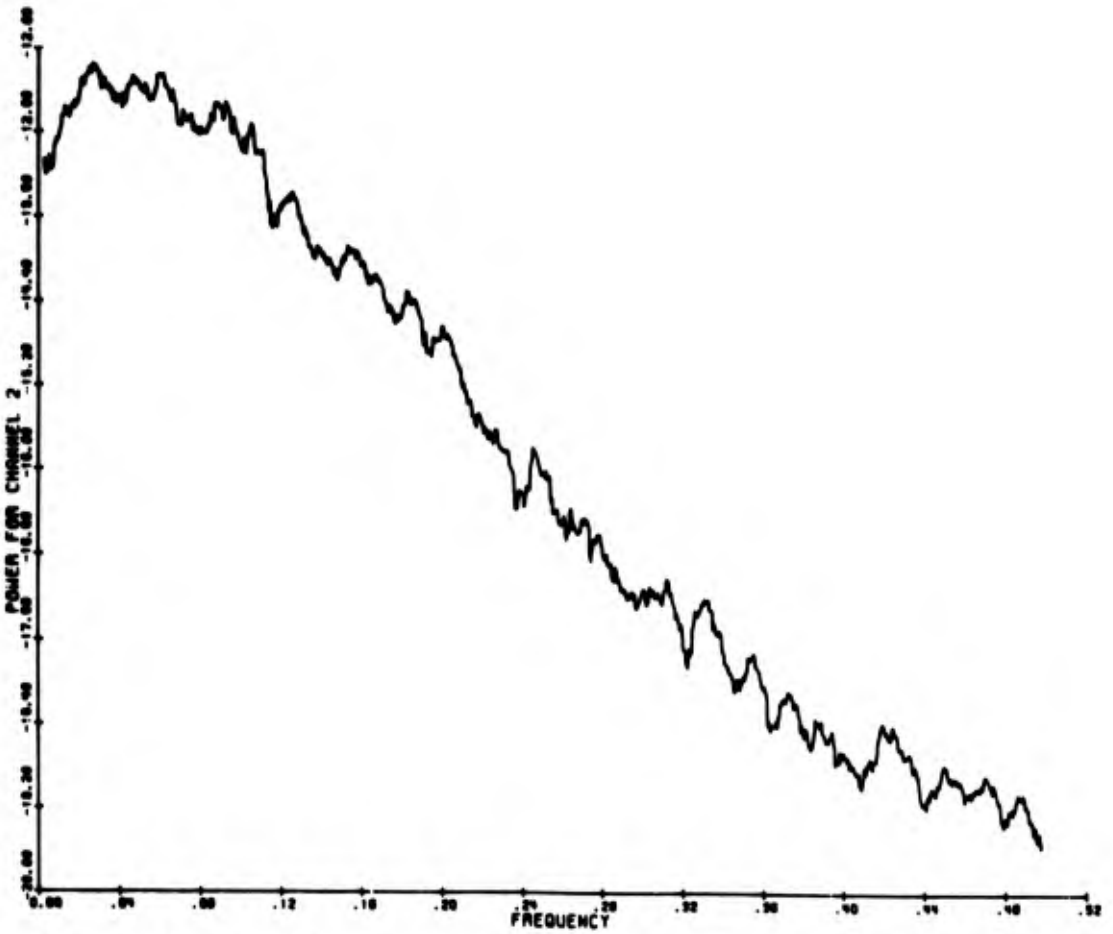

Figure 1-59. Typical Scintillation Power Spectrum, Showing Natural Log of Power Density as a Function of Scintillation Frequency (Hz). Geostationary satellite at 136 MHz operating frequency

None of the small fluctuations is statistically significant, and the "turn-overs" at low and high frequencies are due, respectively, to diffraction effects and receiver noise. The slope of the straight line approximating this distribution is q+1, where the +1 results from diffraction theory.

1-9.2 Morphology of Irregularities

It has already been noted that bottomside Spread-F is characterized by the combination of a stationary and a moving peak in occurrence frequency. Figure 1-60 shows the results of analysis of 180,000 topside ionograms from Alouette 1 in 1963. The percent occurrence of ionograms showing moderate and large spread is shown in magnetic latitude and magnetic time. The polar maximum is clearly displayed, but there is little evidence of the midnight maximum. It may be inferred that the

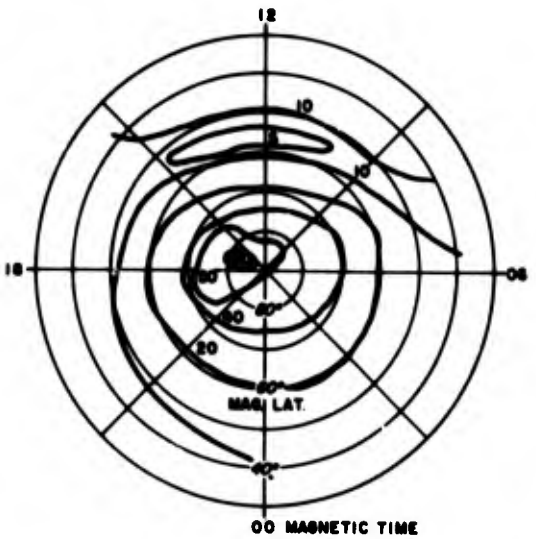

Figure 1-60. Distribution of Percentage Occurrence Frequency of Topside Irregularities in Corrected Geomagnetic Coordinates, from Alouette 1, 1963 (all seasons)

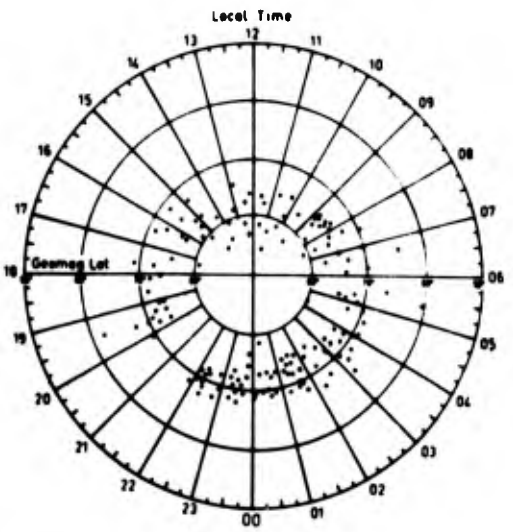

Figure 1-61. Location of Maximum Frequency Spread in Alouette Topside Soundings (Petrie, 1966)

midnight maximum occurs predominantly on the bottomside. Figure 1-61 (Petrie, 1966) shows the location of maximum frequency spread in topside ionograms, for a more limited sample of Alouette data. In this case, the auroral oval is clearly delineated, suggesting that the most intense topside irregularities occur in the presence of visual aurora.

The seasonal and solar-cycle variations of bottomside polar Spread-F may be expressed by the following relationship:

$$P(F_s) = (20 + 0.22\ R) + (10 + 0.11\ R) \cos \frac{2\pi D}{365}$$

where $P(F_s)$ is the probability of Spread-F occurrence in percent, R is sunspot number, and D is day number.

Scintillation of signals propagating through the ionosphere is probably mainly due to irregularities near the peak of the layer and above. Because of the variability of satellite altitudes, and the necessity of considering diffraction effects, the morphology of scintillations at high latitudes may depend to some extent on the particular observational situation (height of irregularities and of the satellite). Also, because the power spectrum of the plasma irregularities may vary spatially, these same diffraction considerations should cause the scintillation morphology to

be dependent upon operating frequency, as well as height of satellite and irregularities and satellite elevation. Aarons (1973) has examined the variations of scintillation occurrence and found a sharp boundary of high latitude scintillations, generally lying a few degrees equatorward of the auroral oval, but differing somewhat in shape from the oval. This boundary shows latitudinal motion with varying magnetic activity, in much the same way as does the auroral oval.

1-10. DESCRIPTION OF SUBROUTINE "JACCHIA"

The subroutine returns the density scale height—SCALEHT—when the following parameters are specified:

FBAR	- average of daily 10.7-cm solar flux values over three successive solar rotations.
F	- value of 10.7-cm solar flux one day earlier than the time specified.
KP	- planetary K-index (real), six hours earlier than the time specified.
SOLDEC	- solar declination in radians.
GEOLAT	- geographic latitude in radians.
HA	- solar hour angle in radians (local solar time + π) .
HEIGHT	- altitude in kilometers.
SCALEHT	- returned in units of kilometers.

The subroutine contains entry points CHGLAT, CHGTIM, and CHGRAD for use when looping on latitude, time, and height respectively. These entry points can be used to reduce execution time when computing grid values. The subroutine occupies 4668 words of core storage and executes in 1 ms on the CDC6600 for a call to SCALEHT. A call to CHGRAD executes in about 0.5 ms.

1-10.1 Description of Subroutine "PROFFIL"

PROFFIL generates a vertical electron density profile from 40-km altitude up to the altitude of the F-layer maximum. Its principal use is intended to be for daytime bottomside ray-tracing applications. The profile which is generated has no discontinuities throughout the specified height range, although two first order (gradient) discontinuities exist in the D-region. These gradient discontinuities, occurring at low electron density values, should have little effect on ray tracing in the HF range. At low frequencies, however, they could conceivably cause problems (spurious partial reflections, coupling between modes) and could be eliminated at some cost in terms of additional complexity.

The required input parameters are

R—sunspot number

SECCHI—secant solar zenith angle

f_0E

f_oF_1

f_oF_2; $h_{max}F$

Bottomside total electron content (TEC)

The subroutine returns the electron density at altitude increments, DH, specified as an input parameter.

1-10.1.1 PROFILE DESCRIPTION

(1) 40 km < z < 65 km

An exponential is fitted:

$$N(z) = N_{40} \exp (B\ (z-40)) \ .$$

(2) 65 km < z < HBOT

HBOT is the altitude one scale height (20 km) below the peak of the E-layer which, in turn, is located at 100 + 20 ln sec χ km. The electron density at HBOT is EDD, determined by extending the E-layer downwards analytically. The shape of the profile in this height range is represented by

$$N(z) = N_{65} \exp (B(z-65)) \ .$$

(3) HBOT < z < HMF

HMF is the height of the F_1-layer maximum, given by

$$156 + 0.15\ R + 45 \ln \sec \chi \text{ km} \ .$$

The profile in this height range is represented by the sum of two alpha Chapman layers, each having a constant scale height (45 km for the F_1-layer; 20 km for the E-layer). The amplitude of the maximum of each layer is adjusted so that the combination of the two reproduces the peak E- and F_1-layer electron densities corresponding to the input parameters. These amplitudes are XONE and XONF for E- and F-layers respectively. The electron density, EDD, at the lower boundary, HBOT, of the layer is obtained from the analytic representation in the upper range.

(4) HMF < z < h_{max}

The total electron content between the F_1- and F_2-layers (CONT) is determined approximately by integrating the combined Chapman layers below HMF and subtracting the result from TEC. The value CONT is then used as a constraint in a special curve-fitting subroutine (COVE). The parameters of the fitted curve, output from COVE, are used to synthesize the electron density in this height range.

If there is no F_1-layer (f_oF_1 = 0), but there is an E-layer, the subroutine fits a single Chapman layer, corresponding to the E-layer, and uses COVE to interpolate between E- and F-layers. If there is no E-layer, PROFFIL should not be used. A simpler parabolic or biparabolic profile is then suggested.

1-10.1.2 ERROR MESSAGES

(1) NO E-LAYER, PROFILE NOT GENERATED

No attempt is made to fit a profile if f_oE is zero.

(2) NO ROOT FOUND IN RANGE 1.10 TO 41.00

The subroutine COVE was unable to fit a curve of the required shape under the given total electron content constraint. The value CONT is bounded by the limits

$$N_1 (h_2-h_1) < CONT < N_2 (h_2-h_1)$$

where

$$N_1 = 1.24 \times 10^4 \times (f_oF_1)^2$$
$$N_2 = 1.24 \times 10^4 \times (f_oF_2)^2$$
$$h_2 = h_{max}$$
$$h_1 = HMF$$

1-11 MAGNETIC ACTIVITY

Short-term variations of the earth's magnetic field are caused by currents flowing in the ionosphere. Since the ionospheric plasma undergoes displacements in the process, the geomagnetic fluctuations may more properly be thought of as manifestations of hydromagnetic phenomena. The driving force may be electric fields, such as the "cross-tail" magnetospheric electric field, or mechanical forces, such as tidally induced pressure gradients. Because of the finite ionospheric conductivity, current flow is accompanied by Joule, dissipative

heating. This heating may have profound effects on the ionospheric structure, due to the temperature dependence of chemical reaction rates, diffusion coefficients, etc. The purely mechanical effects accompanying current flow may also substantially modify ionospheric structure. The geomagnetic field is most variable in the polar regions, and consequently the ionospheric variability is most pronounced there. In order to better understand the polar ionosphere, it is helpful to study the characteristics of geomagnetic disturbance. This section is concerned with the gross indicators of geomagnetic disturbance, K_p, AE and D_{st}—the planetary magnetic index, the auroral electrojet index, and the storm index, respectively.

1-11.1 Statistics of Planetary Index (K_p)

Of the various indices of geomagnetic activity, the most commonly used is K_p, which is derived from the weighted records of 12 standard magnetic observatories. These observatories are so located that the K_p index is a measure of geomagnetic activity at about 40° latitude. Since it is known that the character of magnetic disturbance at high latitudes is notably different from that at midlatitudes, K_p represents a mixture of these two different types of activity, and is not an ideal descriptor of high latitude disturbance. Nevertheless, it is widely used as a measure of high latitude disturbance, as well as a planetary index. K_p is a logarithmic index, and may be converted to the "planetary amplitude index" (a_p) by the following approximate relationship, which is valid for $K_p > 1$:

$$\log a_p \simeq \frac{1}{4} K_p + 0.4 .$$

A recent statistical analysis of K_p, by Zawalick and Cage (1971) covers the period 1932-1970; these results have been adapted to derive the predictive model which follows.

1-11.2 Probability Distribution of K_p

The probability distribution of K_p is shown in Figure 1-62 averaged over approximately 4 1/2 solar cycles. The median index is slightly less than 2-, while the upper and lower deciles are, respectively, 4- and 0.

1-11.3 Persistence of K_p

The persistence is a measure of the length of time that a particular K_p level is exceeded. It is here characterized by the joint probability distribution of the K_p value in any 3-hour interval and the value in the following interval. Figure 1-63 has been constructed from values tabulated by Zawalick and Cage (1971) to display

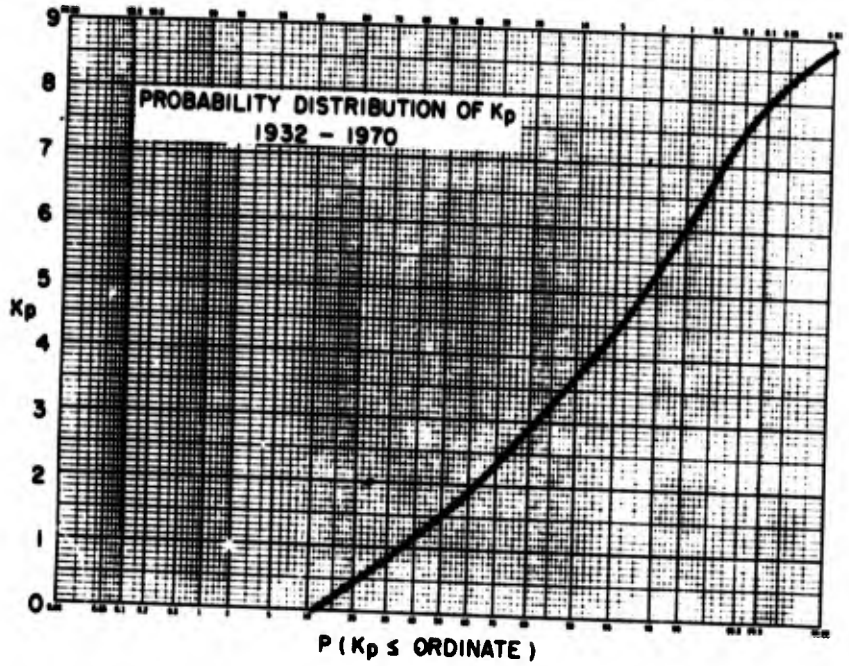

Figure 1-62. Probability Distribution of K_p for the Period 1932-1970

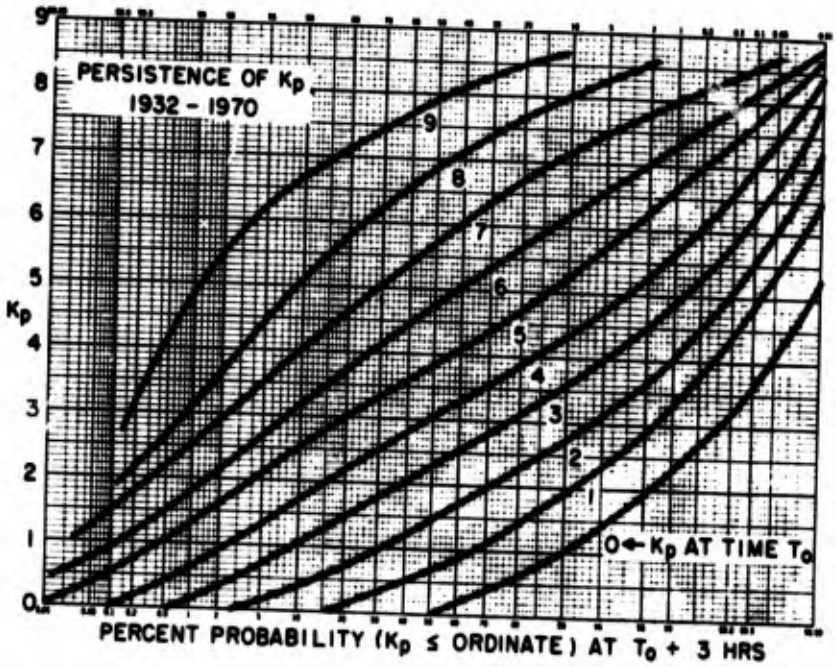

Figure 1-63. Joint Probability Distribution of K_p Values in Any Given 3-hour Interval and the One Immediately Following

this function. An example will serve to illustrate the use of Figure 1-63. Given that the value of K_p in any 3-hour interval is 4, the probability that K_p in the next 3-hour interval will be less than or equal to 4 is 82.5 percent. In general, for K_p greater than about 2, there is approximately a 50 percent probability that the K_p value in the next 3-hour interval is reduced by 1 or more (for example, K_p of 5 followed by K_p of $\leq$ 4). The persistence may be used in a number of ways. An example is shown in Figure 1-64, where the data in Figures 1-62 and 1-63 have been used to compute the number of periods of a given duration (over a 10-year span) in which K_p remains above some preset value.

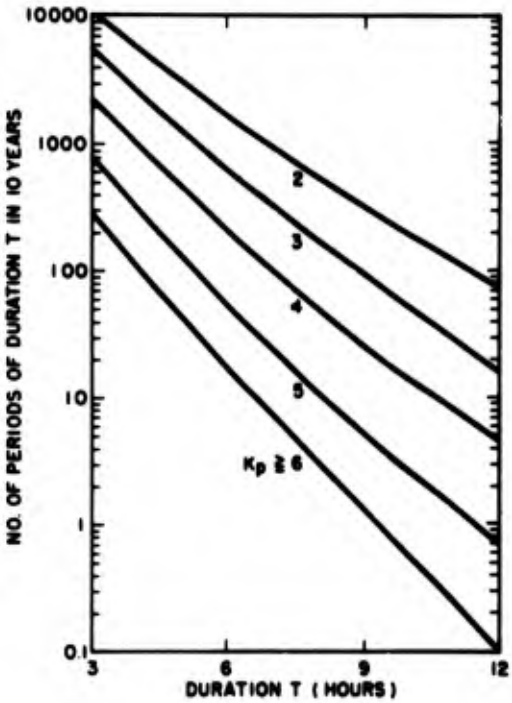

Figure 1-64. Illustrating the Use of K_p Statistics to Estimate the Number of Periods in a 10-year Span in Which the K_p Index Remains Above Some Particular Value for a Given Length of Time

1-11.4 Auroral Electrojet Index (AE)

Beginning in 1957, a magnetic index, designated AE, has been deduced from the records of 7 to 10 observatories located in the zone of maximum auroral occurrence. This index is a better estimator than K_p of high latitude magnetic disturbance, but is not routinely available usually until a year or more after the fact. The AE index is principally a measure of magnetic activity in the midnight sector of the auroral oval, and as such, might be approximated in real time by a suitable located station or set of stations.

Figure 1-65 shows the variation of AE throughout a solar cycle, indicating a maximum variation in the average monthly value of a factor of about 6. Figure 1-66 is a typical probability distribution of hourly AE values, for 1966 in this case. The AE index is seen to be approximately log-normally distributed, with a median value, in 1966, of about 48 gammas. Figure 1-67 shows the solar cycle variation of the median and upper decile of this distribution. These data have been smoothed by numerical filtering in a bandpass filter consisting of the basic 11-year solar cycle period, plus the first two harmonics. Figure 1-68 shows the standard deviation of the AE distribution for each year, after filtering out the seasonal and solar cycle variations (highpass filter with cutoff at 1 cycle/month). The solar cycle trend in short-term variability is clearly seen.

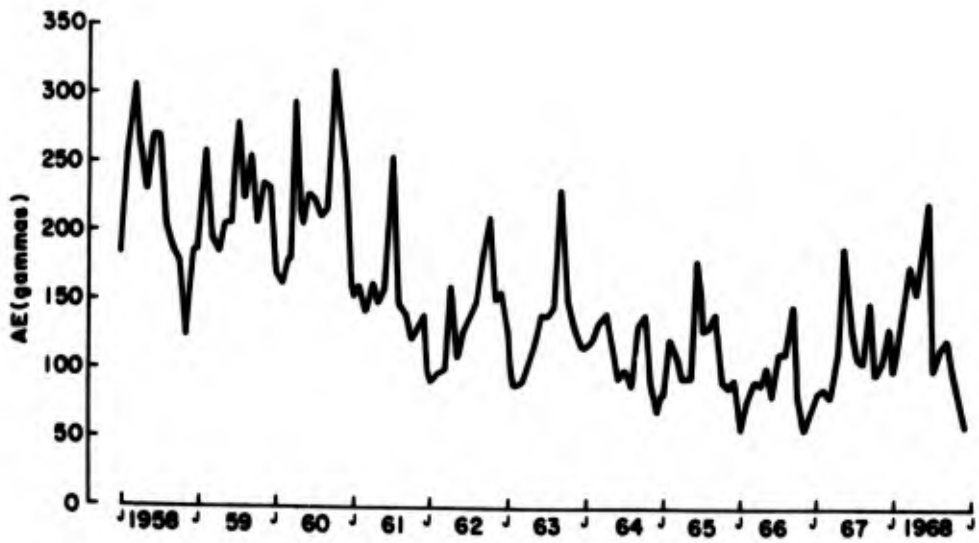

Figure 1-65. Solar Cycle Variation of Average Monthly AE Values

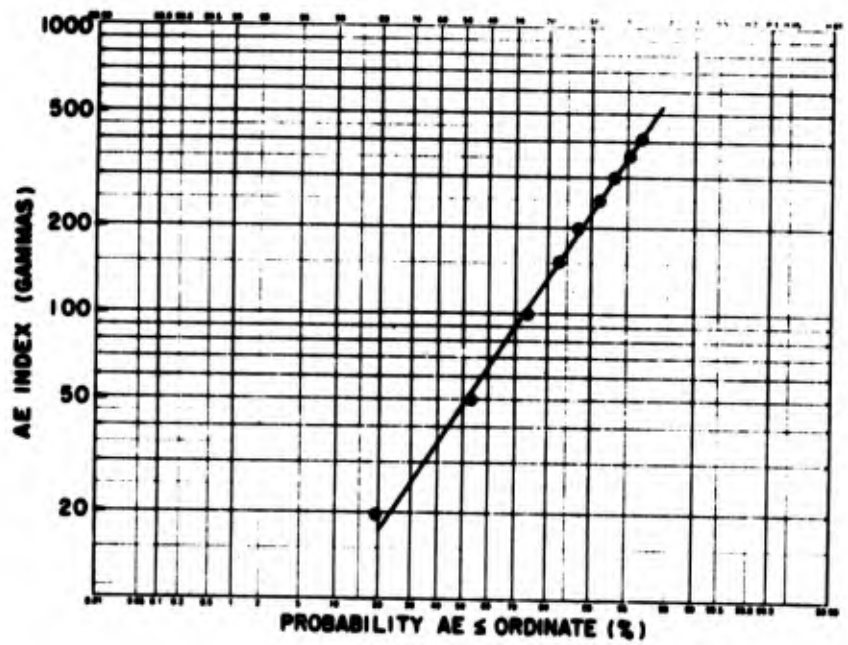

Figure 1-66. Probability Distribution of AE Index for 1966

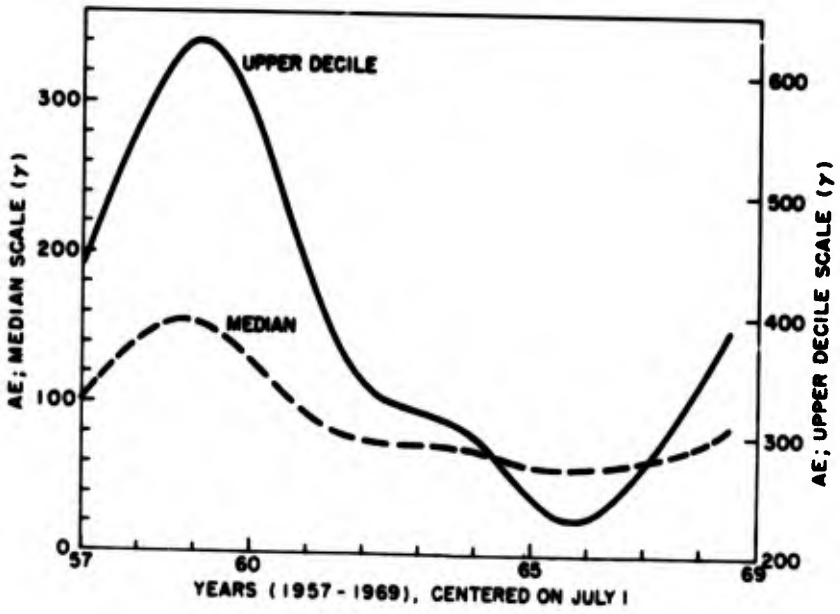

Figure 1-67. Secular Variation of Median and Upper Decile for AE Distribution, Smoothed by a Special Band-pass Filter (see text)

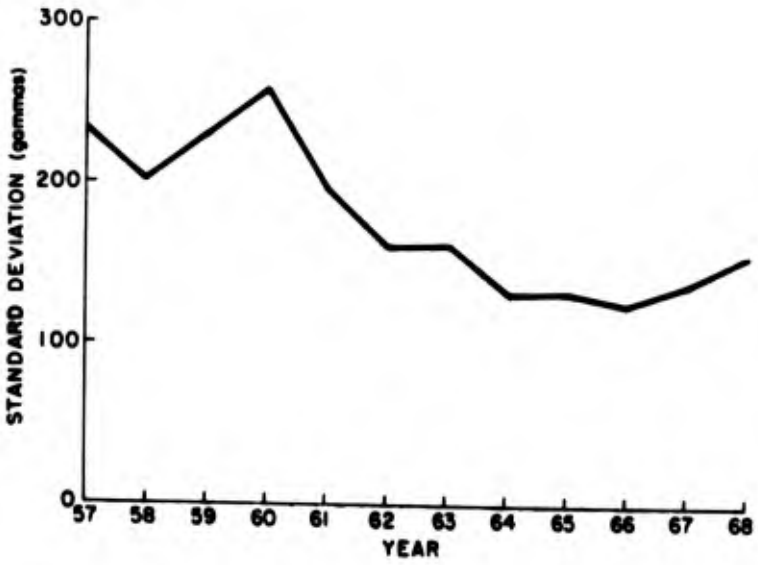

Figure 1-68. Standard Deviation of Short-term (less than 1 month) Fluctuations in AE Index, for period 1957-1968

1-11.5 D_{st} Index

The disturbed (storm-time) component of the worldwide magnetic field is composed of several distinguishable components. Of these, the component that is rotationally symmetric about the earth's magnetic axis (designated D_{st}) has been isolated and is available from 1957 onwards. This component has been tentatively identified with the ring current due to motion of energetic trapped protons in the inner magnetosphere. Enhancements of D_{st} during disturbed periods are therefore caused by ring current enhancements which result from compression of the magnetosphere by the fluctuating momentum flux of the solar wind.

An analysis has been performed on D_{st} similar to that for AE. This analysis, together with a more complete statistical treatment of all magnetic indices will form the basis of a separate report. For purposes of illustration, Figure 1-69 shows the solar cycle trend of the standard deviation of short-term D_{st} variations, in a manner analogous to the AE variation in Figure 1-68.

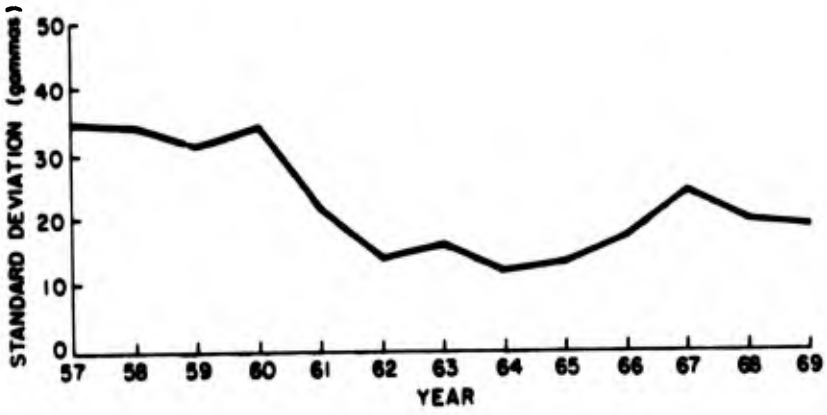

Figure 1-69 Standard Deviation of Short-term (less than 1 month) Fluctuations in AE Index, for D_{st}

1-11.6 Prediction of Solar and Magnetic Activity

There is no known reliable means of predicting, far in advance, what levels of solar and magnetic activity will be observed. Nevertheless, certain periodicities have been noted in the time series of existing magnetic and solar data, and it seems not unreasonable to attempt to extrapolate these variations into the future. To the extent that such a method is philosophically valid, future levels of solar and magnetic activity can be estimated, at least in statistical terms.

Fraser-Smith (1972) has performed spectral analysis on sunspot number and A_p data, covering the period 1930-1970. A_p is the average of the eight daily a_p values. By approximating both time series by the six or seven largest spectral features, the series can be extended to any arbitrary date in the future.

Acknowledgments

Mrs. Margo Leftin of the Institute for Telecommunications Sciences generously provided the hourly f_oF_2 data for 1958 in digital form.

Dr. G. Lockwood of the Canadian Communications Research Center made available the Alouette true-height profiles and Alosyn f_oF_2 data in digital form.

Dr. M. Friedman, Mr. J. Tardelli, and Mr. E. Cohen of the ARCON Corporation performed the bulk of the computer analysis.

The assistance of all of these people is gratefully acknowledged.

References

Aarons, J. (1973) AGARD Report AG-166, p57.

Astakov, P.G., Gorbushina, G.N., and Krupitskaya, T.M. (1970) Problemi Antarktiki, Gidrometeorizdat, Leningrad, No. 33.

Barghausen, A.F., Finney, J.W., Proctor, L.L. and Shultz, L.D. (1969) ESSA Tech. Rept., ERL 110 - ITS 78.

Becker, W. and Stubbe, P. (1963) Proc. Int. Conf. on the Ionosphere, Inst. Phys. and Phys. Soc., p. 35.

Bowman, G.G. (1967) AVCO Rept., AVSSD-0354-66-CR.

Chandra, S. and Krishnamurthy, B.V. (1968) J. Atmos. Terr. Phys. 30:47.

Charakhchyan, A.N. and Charakhchyan, T.N. (1967) Geomag. and Aeron. 7:791.

Craven, J.D. (1970) J. Geophys. Res. 74:2468.

Davies, K. (1965) Ionospheric Radio Propagation, NBS Monograph No. 80.

Dyson, P. (1973) Private Communication.

Dungey, J.W. (1956) J. Atmos. Terr. Phys. 9:90.

Eather, R.H. and Jacka, F. (1966) Australian J. Phys. 19:241.

Elkins, T.J. and Papagiannis, M.D. (1969) J. Geophys. Res. 74:4105.

Fairfield, D.H. (1968) J. Geophys. Res. 73:7329.

Fraser-Smith, A.C. (1972) J. Geophys. Res. 77:4209.

Freyzon, I.A. and Shapiro, B.S. (1972) Geomag. and Aeron. 12:101.

Gnedenko, B. (1967) Theory of Probability, Chelsea Publ. Co.

Gordon, W.E. (1967) Rev. Geophys. 5:191.

Gustaffson, G. (1970) Ann. Geophys. 5(No. 40).

Hakura, Y. (1965) Repts. Ionos. Space Res., Japan, 19:121.

Jacchia, L.G. (1970) Smithsonian Astrophys. Observ., Rept. No. 313.

King. G.A.M. (1965) J. Atmos. Terr. Phys. 27:426.

Lingenfelter, R.E. (1963) Rev. Geophys. 1:35.

Montalbetti, R. and McEwen, D.J. (1962) J. of Phys. Soc. (Japan) 17 (Supplement A-1).

Nestorov, G. (1972) Geomag. and Aeron. 12:36.

Oguti, T. and Marubashi, K. (1966) Repts. Ionos. Space Res., Japan, p 96.

Penndorf, R.B. (1960) RADC Tech. Rept., RAD-TR-61-1.

Penndorf, R.B. and Katz, A. (1969) RADC Tech. Rept., AF RADC-TR-69-390.

Petrie, L.E. (1966) Spread-F and its Effects on Radiowave Propagation and Communication, P. Newman, Editor, Maidenhead, England, Technivision, p 67.

Phelps, A. (1973) Private communication.

Rawer, K. and Suchy, K. (1967) Handbuch der Physic, Vol. XLIX/2, Geophysics, Part III.

Rishbeth, H. (1967) Proc. IEEE 55:16.

Rishbeth, H. and Barron, D.W. (1960) J. Atmos. Terr. Phys. 18:234.

Rishbeth, H. and Setty, C.S.G.K. (1961) J. Atmos. Terr. Phys. 18:234.

Sukhorukova, E.V. (196[illegible]) Geomag. and Aeron. 4:732.

Tao, K. (1966) J. Radio Res. Labs. 12(No. 64):317.

Wagner, R. (1973) Private communication.

Walters, G.K. (1966) J. Geophys. Res. 71:1341.

Zawalick, E.J. and Cage, A.L. (1971) J. Geophys. Res. 76:7009.

Zherebtsov, G.A. and Kurilov, V.A. (1971) Geomag. and Aeron. 11:611.

Contents

2. Mapping of High Latitude Ionospheric Characteristics

R. Sagalyn, S. Bredesen, and P. Wildman
Ionospheric Physics Laboratory
Air Force Cambridge Research Laboratories
Bedford, Massachusetts

2-1. INTRODUCTION

Local time and seasonal characteristics of the high-latitude ionization irregularity regions have been determined from the examination of the ISIS-I Satellite thermal charged particle data during the first year of satellite operation, February 1969 to February 1970. ISIS-I, launched 30 January 1969 into a polar orbit, inclination 88.5 deg, has an apogee of 3526 km and perigee of 525 km. Frequency of occurrence calculations of the equatorial and polar boundaries of the irregularity zones are based primarily on Northern Hemisphere data. The amplitude and width of the thermal charged particle trough, for electrons and ions, located at the equatorial edge of the irregularity zone, have been evaluated as a function of local time using both Southern and Northern Hemisphere data. Results from over 3000 satellite orbits were examined in this study.

Although the electrostatic probe results were obtained in the topside ionosphere, extensive comparisons with simultaneous topside sounder measurements on board ISIS-I show that down to the minimum scale size which can be observed with the sounder, approximately 18 km, the irregularities map down to the peak of the F-region. These results thus represent a statistical mapping of ionospheric characteristics at the peak of the F-layer of the ionosphere.

2-2. THE EXPERIMENT

The thermal charged particle data used in this study was obtained with a spherical electrostatic analyzer which measured the ion density, the ion energy distribution (to 75 eV), the satellite potential, and the ratio of the ion mass to the ion temperature. The sensor, mounted on a 96-cm boom, consists of three concentric spherical electrodes with radii of 1.90, 2.54, and 3.18 cm. The operation of the probe is described by the equations of motion for charged particles in a central force field (Sagalyn et al, 1963; Sagalyn and Smiddy, 1967; Smiddy and Stuart, 1969). Ion densities are sampled 60 times per second (corresponding to a spatial resolution of 150 m), the ratio of the mass to the temperature is sampled once per minute, and the energy distribution is sampled once every 2 min.

2-3. METHOD AND DEFINITIONS

The equatorial boundary of the irregularity region is taken to be the latitude of onset of persistent small-scale ionization irregularities extending over at least a few degrees in latitude with amplitudes amounting to 20 percent or more of the mean background level. The scale size is highly variable with dimensions ranging typically from 1 to 140 km. Representative examples of small-scale irregularities are shown in Figure 2-1. The electron or ion trough, when observed, is found at the equatorwards edge of the irregularity region. In this study, the trough is considered as part of the irregularity zone. Its scale size typically ranges from 140 to 1500 km in latitudinal extent. Examples of typical troughs are shown in Figure 2-9.

The location of the high latitude boundary of the irregularity zone is defined as the latitude where small-scale irregularities of amplitude 20 percent or more above background are no longer observed.

For the seasonal study, one month's data centered about the equinoxes and solstices was fully examined. This corresponds to about 340 orbits per season. For the frequency of occurrence calculations, the results were separated into intervals of 5 deg of invariant latitude. Orbits on which no clear cut irregularity boundary was observed are included in the frequency calculations. For the local time study, results were separated into 3-hr intervals and 5-deg invariant latitude intervals. All results obtained between February and December 1969, amounting to approximately 3500 orbits of data, were used in the local time study.

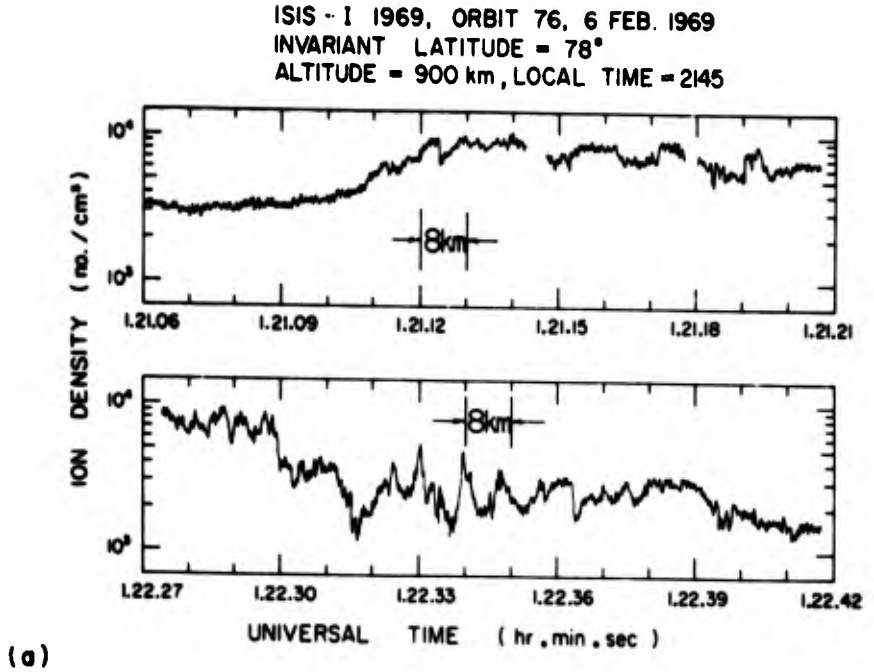

(a)

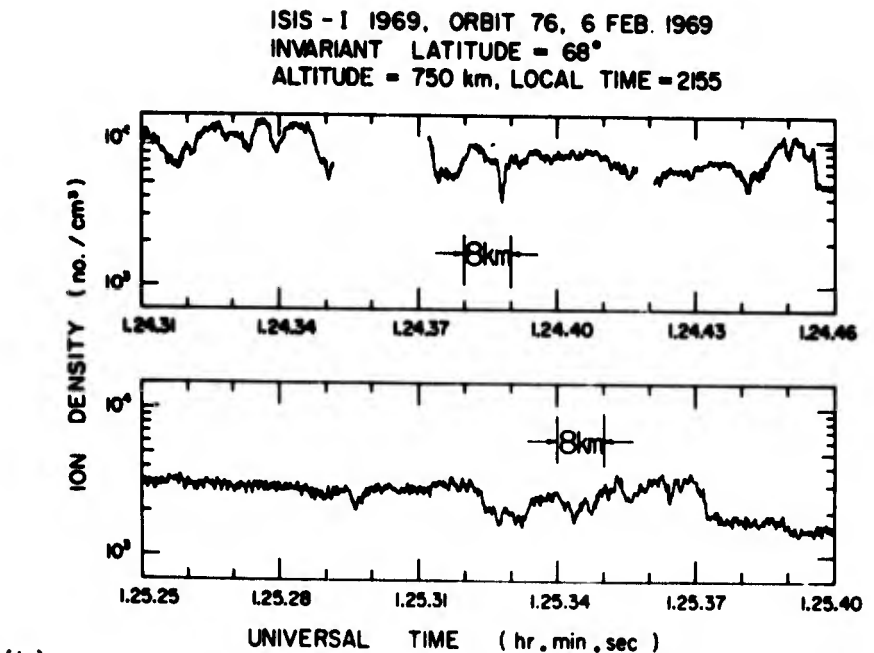

(b)

Figure 2-1. Two Typical ISIS-1 Passes Showing Small-scale Variations in Plasma Density

2-4. SEASONAL VARIATION OF IRREGULARITY BOUNDARIES

The frequency of occurrence of equatorial and polar boundaries of the irregularity regions was evaluated as a function of invariant latitude for the months of March, June, September and December 1969. In each hemisphere, the satellite traverses the irregularity zone at two local times approximately 12 hr apart. Thus, in the Northern Hemisphere for each season there are results for two different local time sectors.

2-5. EQUATORIAL BOUNDARIES

The range of local times at the location of the equatorial boundary for each season are summarized in Table 2-1.

The frequency calculations were averaged over 5-deg intervals of invariant latitude. The results for the morning and day periods are given in Figure 2-2a, and those for evening and night are given in Figure 2-2b. Only results obtained in the Northern Hemisphere when the K_p index was ≤ 3 are included. It is seen from Figure 2-2 and the information given in Table 2-1 that the equatorial boundary is most sharply defined and reaches its maximum value of 72 deg around local noon in June and December. At the equinoxes, the probability of occurrence of the boundary is approximately equal over a 20-deg range in invariant latitude. Then it is not possible to precisely predict the latitude of onset of significant ionization irregularities. In order to accurately describe the seasonal variation of the irregularity boundary, it is necessary to first normalize all results to a given

Table 2-1. Local Times and Mean Locations of Equatorial Boundary of Irregularity Region

Month and Periods		Local Time Range (hr)	Invariant Lat. of Mean (deg)
March	Morning	6 - 10	66
	Evening	18 - 21	64
June	Day	11 - 14	72
	Night	23 - 2	63
September	Morning	5 - 7	61
	Evening	17 - 19	70
December	Day	10 - 13	67
	Night	21 - 24	56

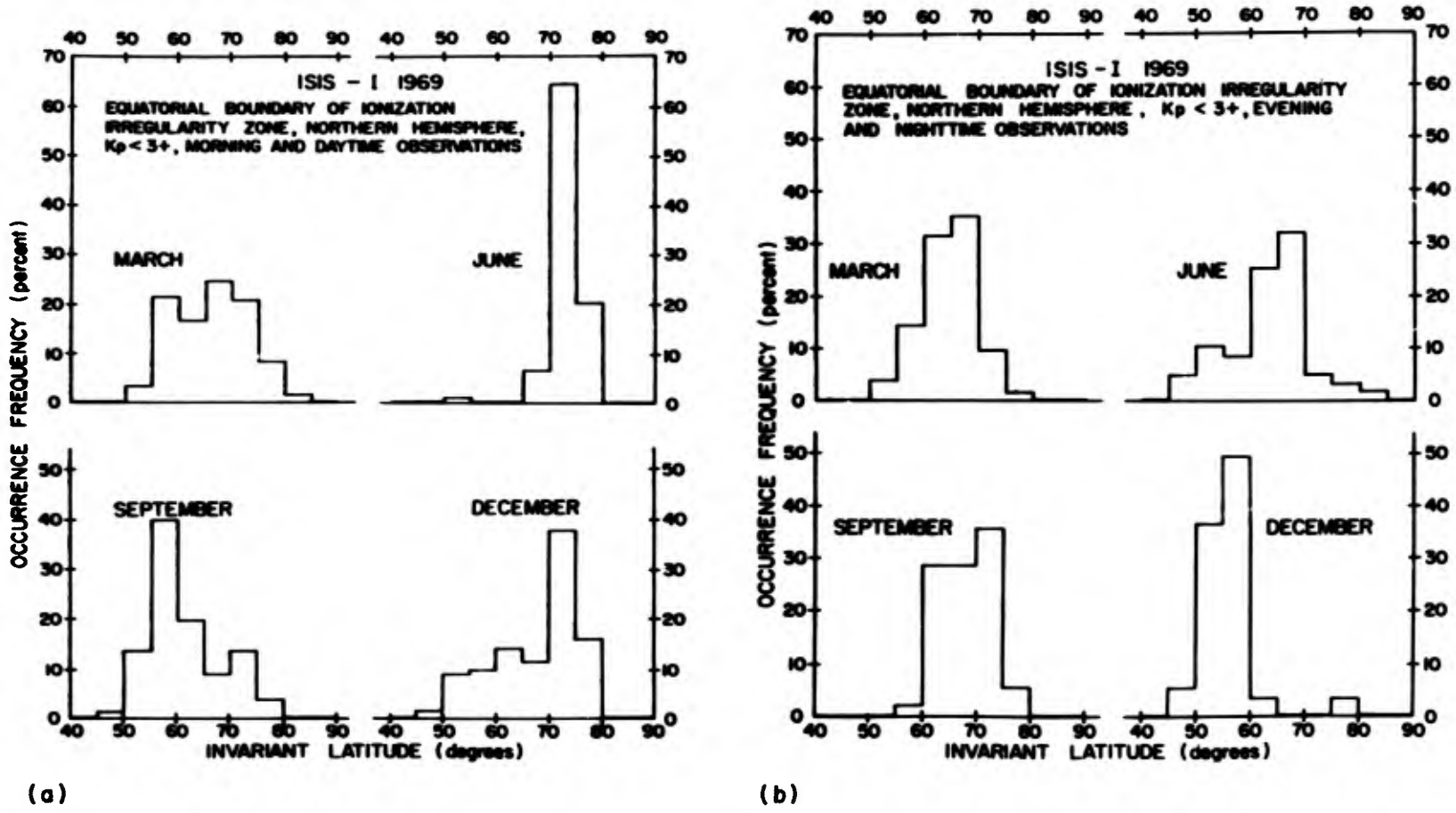

Figure 2-2. Seasonal and Latitudinal Variations of the Equatorial Boundary of the Ionization Irregularity Zone: (a) Morning and daytime observations; (b) evening and nighttime observations

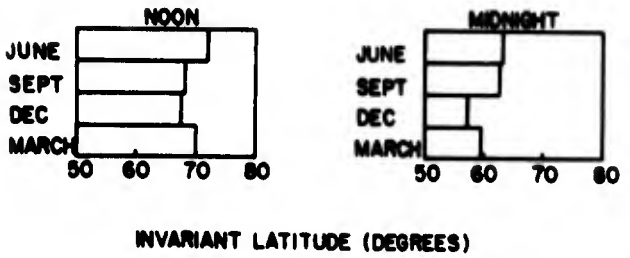

Figure 2-3. Seasonal Variations of the Equatorial Boundary of the Irregularity Zone for the Northern Hemisphere ($K_p \leq 3$) for Low Magnetic Activity

local time because of the large diurnal variation of the boundary location which is described in a later section and illustrated in Figure 2-8. In this work, all morning and daytime results were normalized to local noon and all evening and night results to local midnight. The results given in Figure 2-2 were used to carry out the normalization. The histogram of Figure 2-3 summarizes the normalized seasonal results in the Northern Hemisphere.

The most striking aspect of these results is that the seasonal variation of the location of the boundary is small. At local noon the maximum change of the boundary location is 4 deg, while at midnight a maximum seasonal change of 6 deg is found. Further, as might be expected from the changing position of the sun, in the Northern Hemisphere the boundary is closest to the pole in June and furthest from the pole in December (Figure 2-3). The locations in March and September lie at or in between these limits.

2-6. POLEWARD BOUNDARIES

Identical calculations were carried out for the identification of the polar boundary of the irregularity zone. The number of orbits examined in each season as well as the local time of the measurements are listed in Table 2-2. The maximum invariant latitude of the satellite varied from orbit to orbit between 83 and 90 deg. If the irregularity zone extended up to the maximum latitude reached by the satellite on any given orbit, that orbit was considered to have no upper boundary.

Typical examples of high latitude results are shown in Figure 2-4. In March, June, September and December a total of 295 orbits were included. No polar boundaries for the irregularity zone were found; the inhomogeneities extend across the pole. Since the same result is found in each season and for all local times, this result was assumed in the local time study where the temporal characteristics of only the equatorial boundary were determined.

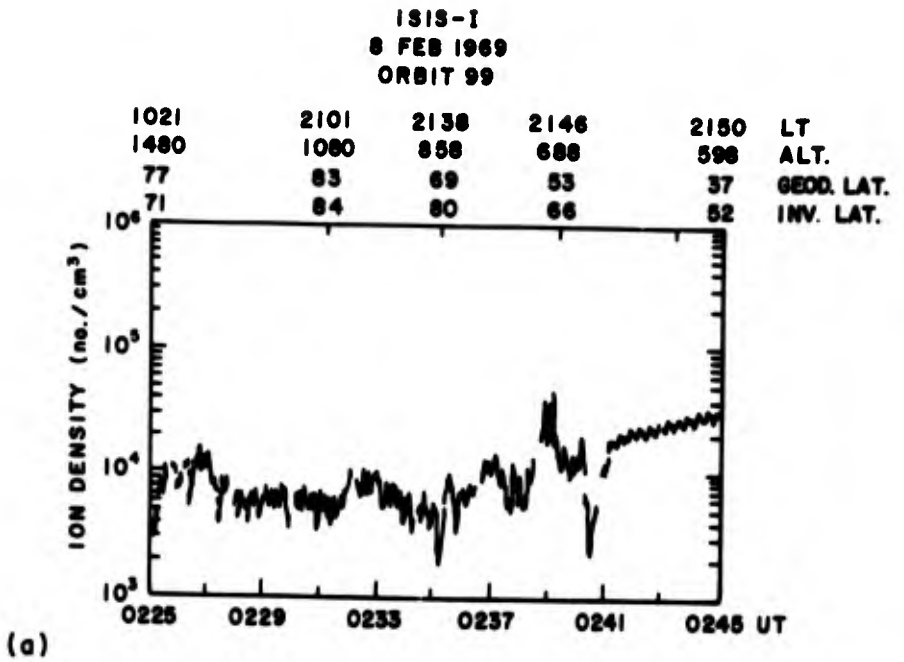

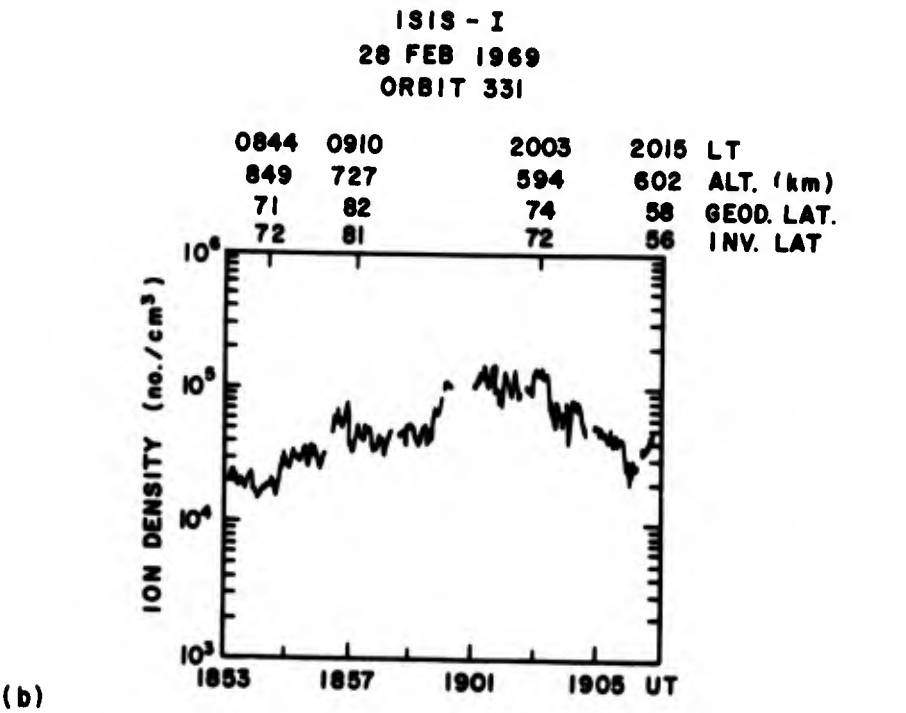

Figure 2-4. Examples of Passes Crossing the Polar Cap

Table 2-2. Poleward Boundaries of Ionization Irregularity Zone, Northern Hemisphere ($K_p < 3+$)

Month	Local Time (hr)	Number of Orbits
March	6 - 10	24
	17 - 20	16
June	10 - 13	49
	0 - 3	39
September	4 - 7	37
	17 - 20	19
December	11 - 15	63
	20 - 24	48

Comparison of these results with the auroral oval of Feldstein and Starkov (1967) show that the mean position of the equatorial boundary of the irregularity zone, as defined by the ISIS satellite date, is at a slightly lower latitude. For example, in Table 2-3 the mean position of the equatorial edge of the oval for $K_p = 3$ is compared with the ISIS diurnal results for $K_p \leq 3$.

Table 2-3. Comparison of Auroral Oval and ISIS-I Equatorial Boundaries

Local Time (hr)	12:00	18:00	24:00	6:00
Invariant Latitude Oval	73	69	64	69
Invariant Latitude ISIS	72	66	61	64

The small differences in these two types of results could be due to differences in the definitions of the quantities measured. The oval boundary is defined as the latitude above which the probability of optical emissions is ≥ 70 percent. The ISIS boundary is defined as the location of the onset of irregularities of magnitude 20 percent or greater which persist over several degrees of latitude.

A significant difference exists in the identification of the upper boundary. The oval boundary for the conditions cited above is located at 76-deg invariant at local noon and 72 deg at midnight, whereas no upper boundary is found in the ISIS results. We do not have an unambiguous explanation for these differences.

It could be that the mechanisms operating to produce irregularities in electron and ion density near the pole do not produce optical emissions. Examples of such mechanisms could be plasma turbulence, or particles with energies below 15 eV. These results indicate that the upper boundary of the auroral oval is not a good reference parameter for propagation work. Rather, it must be assumed that the ionization irregularities which perturb electromagnetic propagation persist across the polar cap.

A comparison of the ISIS results with the evening and night scintillations of Aarons et al (1971) is given in Table 2-4.

Table 2-4. Comparison of Scintillation and ISIS-I Equatorial Boundaries

Local Time (hr)	18:00	22:00	3:00
Invariant Latitude Scintillation	60	58	62
Invariant Latitude ISIS	65	60	62

The lower scintillation boundary is defined as the latitude at which the mean scintillation index at 40 MHz is 50 percent. The results are in good agreement except in the early evening hours. Between 20 and 4 hr LT, the scintillation and in situ ISIS-I boundaries agree within 2 deg for $K_p \leq 3$. This gives strong support to the conclusion that the scintillations are produced by small-scale irregularities of the type observed by ISIS-I. It further suggests that the ISIS-I statistical results could be used to predict the location of high latitude scintillation regions from 5 through 16 hr LT. Little statistical information on high latitude scintillation boundaries is available at these times (Aarons and Allen, 1971).

2-7. DIURNAL VARIATION

The diurnal variation of the location and characteristics of the equatorial boundary of the irregularity region were examined. The frequency of occurrence was evaluated as a function of invariant latitude at 3-hr intervals of local time for the Northern Hemisphere measurements. The data was separated into two parts depending upon the magnetic conditions: magnetic activity index $K_p \leq 3$ and $K_p \geq 3+$. The number of orbits for which data was available for each time interval varied between 22 and 186. On the average, there were 80 orbits of data for each 3-hr period.

The results are shown in Figures 2-5 and 2-6 for low and high K_p, respectively. Examination of the results in Figure 2-5 shows that the frequency of occurrence distribution of the location of the equatorial boundary for low K_p is broad, poorly defined, on a statistical basis except within 3 hr of local noon. The distribution obtained from 9-to-12 and 12-to-15 hr show that the location of the boundary can be predicted to within 5 deg near noon. This result corroborates information gained from studies of precipitating particles, namely, that near local noon there is only one significant cause of ionization inhomogeneties—the precipitation of magnetosheath particles via the neutral points in the geomagnetic field. At other local times several influences are operating simultaneously, including bulk ion motions, plasma deformation, plasma instabilities, greatly reduced influence of solar UV, etc. As reflected in the results of Figures 2-5 and 2-6, the boundary is poorly defined on a statistical basis.

The results of Figure 2-5 also show that the mean location of the boundary has a simple diurnal variation. Around midnight the boundary is located at minimum latitude and reaches a maximum around local noon. This is clearly illustrated in Figure 2-7 where the mean location of the boundary has been plotted as a function of local time for the two ranges of magnetic activity. The diurnal results are also summarized on the polar plot of Figure 2-8 where the mean location of the equatorial boundary for $K_p < 3+$ has been plotted versus local time.

In the results for high K_p (Figure 2-6), diurnal trends similar to those observed for low K_p are found. In the evening between 18 and 24 hr LT, however, the distributions are distinctly sharper. This is the region of the turbulent convective interface between the ionosphere and the magnetosphere, and could be the result of increased plasma convective flow during magnetic disturbances. Also, the boundary is at a minimum latitude in the 3-hr period following midnight rather than in the 2100 - 2400 hr period observed at low K_p. This is in good agreement with the scintillation measurements of Aarons and Allen (1971) at high K_p. The diurnal variation of the mean location of the boundary for $K_p \geq 3+$, as shown in Figure 2-7, follows the results obtained for low K_p; however, the amplitude of the daily variation is larger. Further, at each local time range the mean location of the boundary $K_p \geq 3+$ is found at a lower invarient latitude than during undisturbed conditions. This is due to the movement of the ionospheric plasma equatorwards during storms and is in agreement with results of optical measurements, whistler studies, and satellite electrostatic probe measurements.

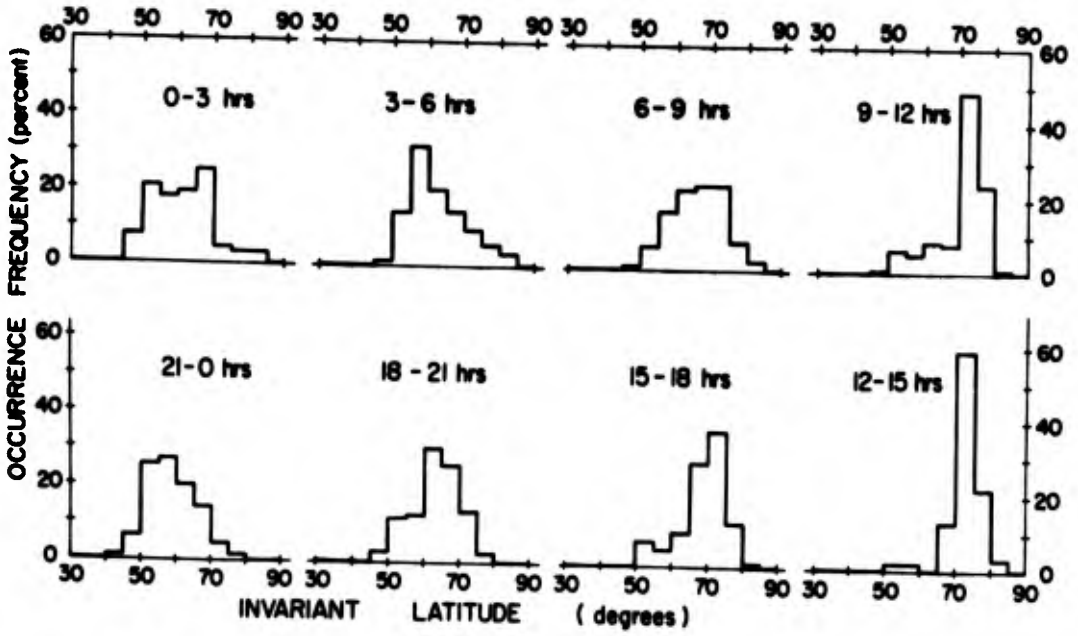

Figure 2-5. Equatorial Boundary of the Ionization Irregularity Zone in the Northern Hemisphere ($K_p \leq 3+$) as a Function of Local Time for Low Magnetic Activity

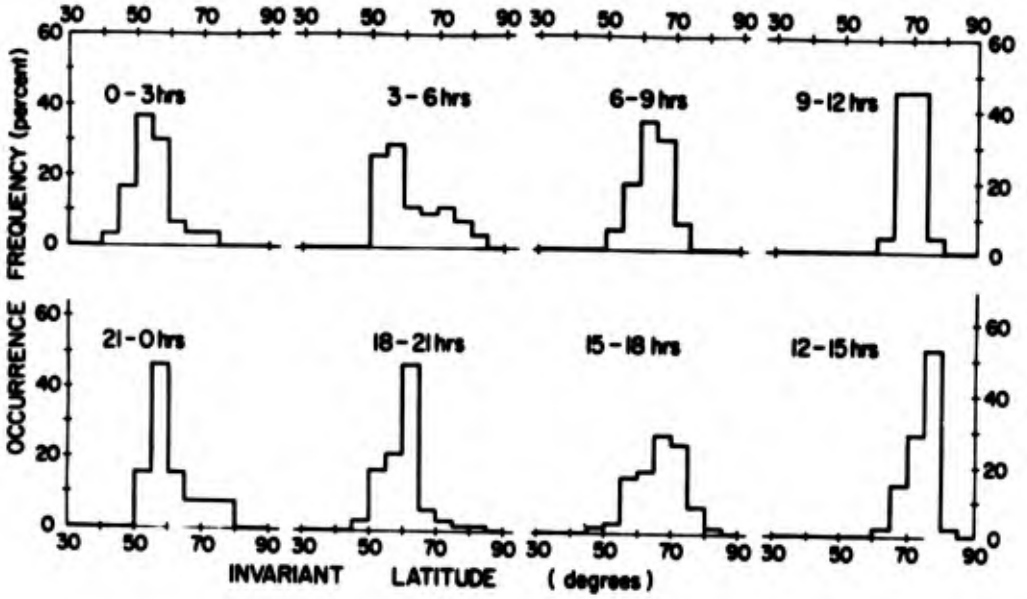

Figure 2-6. Equatorial Boundary of the Ionization Irregularity Zone in the Northern Hemisphere ($K_p \leq 3+$) as a Function of Local Time for High Magnetic Activity

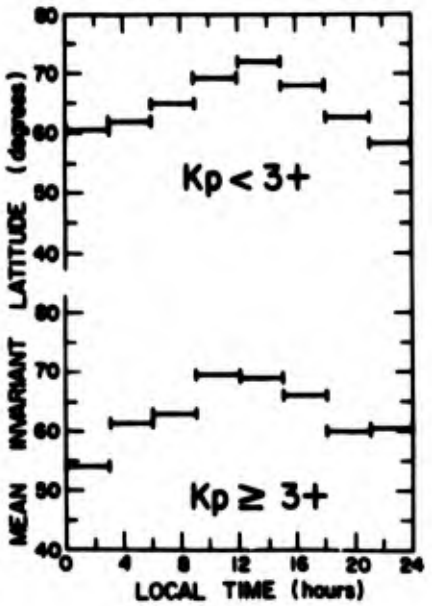

Figure 2-7. Mean Invariant Latitude of the Equatorial Boundary of the Ionization Irregularity Zone in the Northern Hemisphere for Two K_p Ranges

Figure 2-8. Mean Invariant Latitude of the Equatorial Boundary of the Ionization Irregularity Zone as a Function of Time; Northern Hemisphere ($K_p < 3+$)

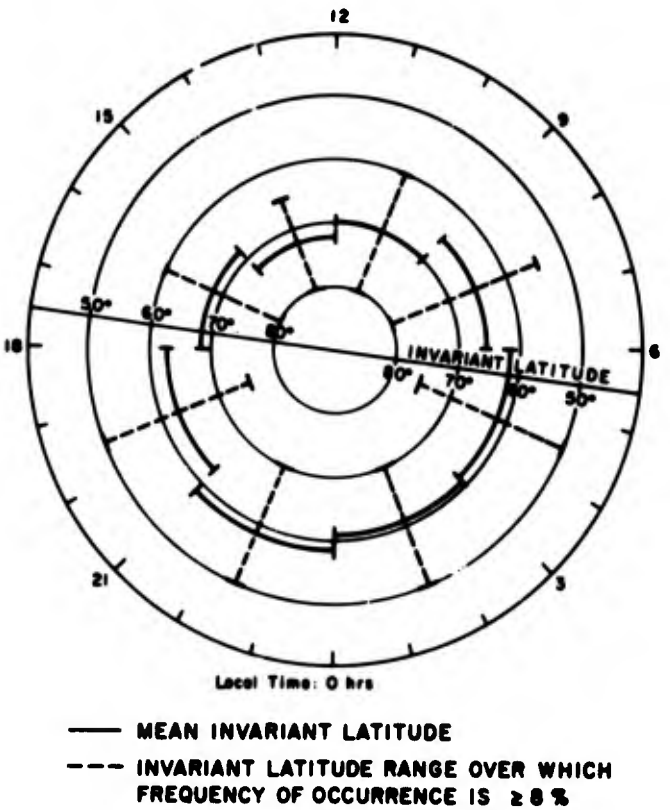

2-8. SOUTHERN HEMISPHERE

Mapping of the characteristics of the irregularity region in the Southern Hemisphere as a function of season and local time is under way. Significant differences are found in the location and shape of the frequency of occurrence distributions as compared with results obtained in the Northern Hemisphere.

2-9. HIGH LATITUDE TROUGH

One type of high latitude ionization irregularity has been studied in some detail; that is, the trough or depression in the thermal ion and electron density which is frequently observed at the equatorial edge of the irregularity zone (Muldrew, 1965; Rycroft and Thomas, 1970; Tulunay and Sayers, 1971). The trough is often the first of several major depressions and enhancements of the ambient plasma density. A trough is counted when two measurable gradients (density decrease followed by an increase toward the pole) are observed in the data. In addition, for a trough to be included in the calculations of frequency of occurrence, a minimum value of 1.3:1 for the peak to valley density ratio must be observed. Typical trough examples are shown in Figures 2-9 and 2-10.

Frequently, a sharp depression of ionization is observed at the equatorial boundary which is not followed by a poleward increase. These have been included in the study as single gradient depressions. The trough and single gradient depressions are of special interest to electromagnetic propagation. They are the first major ionospheric irregularity in the poleward direction which can significantly alter electromagnetic wave properties producing refraction, absorption, phase changes, etc.

The frequency of occurrence of both troughs and troughs plus single gradient depressions have been evaluated in 2-hr intervals over a 24-hr period using results of 6 months of satellite data. The results are given in Figure 2-11. Troughs are found to occur on 27 percent of all orbits at all local times, while either troughs or single gradient depressions are found to occur on 51 percent of all orbits at all local times. A significant diurnal variation in the frequency of occurrence exists, as seen in Figure 2-11. Troughs are rarely observed in daylight between 6 and 16 hr LT. The frequency of occurrence increases near sunset, reaching a maximum between 22 and 3 hr LT. A rapid decrease in trough frequency is observed around sunrise. The diurnal distribution of either troughs or single gradients is similar, but with a maximum frequency of occurrence found in the early morning hours around 4 hr LT.

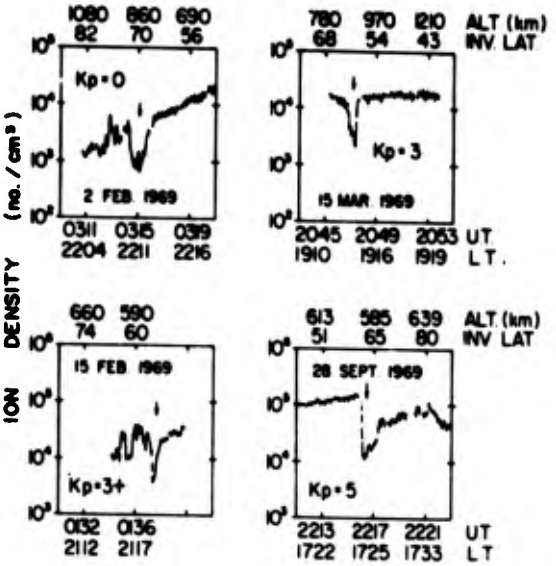

Figure 2-9. Examples of Ionization Troughs

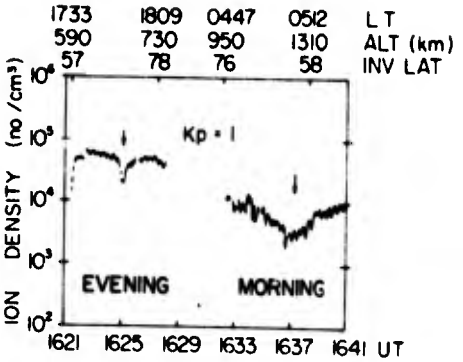

Figure 2-10. A Transpolar Orbit Showing Nightside and Dayside Trough

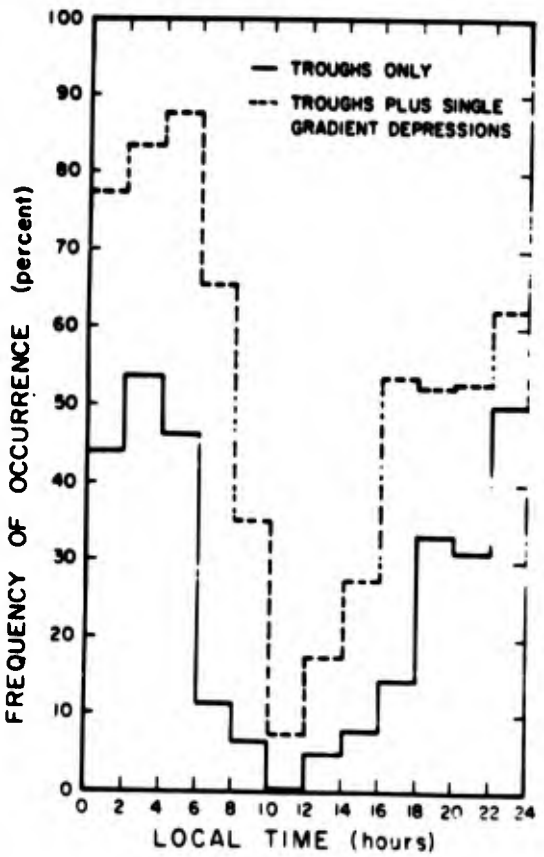

Figure 2-11. Variation With Local Time of the Occurrence Frequency of the Trough

The diurnal variation in the frequency of occurrence of troughs and single gradients is the result of the combination of two processes: (1) the diurnal variation of the bulk motion of the plasma with a maximum outward flow at night, and (2) the diurnal variation in the charged particle production rate due to solar UV. A strong dependence of local production on solar zenith angle exists; also, charged particle production at any given solar zenith angle tends to fill in troughs on the dayside.

Since troughs are included in the calculations of the equatorial boundary of the irregularity zone, the seasonal and local time results given in Figures 2-2, 2-3, 2-5, 2-6, 2-7, and 2-8 define the position of the equatorial edge of the trough or single gradient depressions from approximately 16 through 6 LT when their occurrence frequency is high. The average trough width at half depth is found to be 4 ± 2 deg of latitude. The average charge density gradient at the trough (that is, N_1/N_2 per degree of latitude) is found equal to 1.6. (If N_1 is the density at L_1° latitude, then N_2 is the density at $L_2^{\circ} = L_1^{\circ} + 1^{\circ}$.) A maximum value of 2.8 is observed in the late evening hours.

2-10. SUMMARY

The mapping of the characteristics of the high latitude ionization irregularity regions of the ionosphere as a function of season and local time, based on ISIS-I electrostatic probe measurements, has yielded the following results:

(1) A small seasonal variation exists in the location of the equatorial boundary of the irregularity region. The boundary reaches its maximum latitude in June and its minimum in December at any given local time. The magnitude of the seasonal variation in the location of the boundary is $5^{\circ} \pm 1^{\circ}$ for $K_p \leq 3$.

(2) A large diurnal variation, magnitude 15 deg, is found in the mean location of the equatorial boundary for $K_p \leq 3$. The occurrence frequency distributions also vary with local time. The sharpest distribution is found near local noon; standard deviation of the distribution $\sigma = 5^{\circ}$. The broadest distribution is observed near local midnight; standard deviation of the distribution $\sigma = 8^{\circ}$.

(3) The ionization irregularity region extends across the polar cap. There is no upper boundary.

(4) The average location of the boundary at a given local time is 2 to 6 deg lower for $K_p \geq 3+$ than for $K_p \leq 3$.

(5) A large diurnal variation is found in the frequency of occurrence of troughs and troughs plus single gradient depressions. The maximum frequency of occurrence equal to 88 percent is found near 5 hr LT; the minimum of 6 percent is observed between 10 and 12 hr.

(6) The average trough width at half depth is found to be 4 ± 2 deg latitude.

(7) The evaluation of the density gradients at the trough gives an average value of 1.6 in units of N_1/N_2 per degree of latitude.

References

Aarons, J., and Allen, R.S. (1971) Scintillation boundary during quiet and disturbed magnetic conditions, J. Geophys. Res. 76:170.

Aarons, H., Whitney, H.E., and Allen, R.S. (1971) Global morphology of ionospheric scintillations, Proc. of IEEE 59:159.

Feldstein, Y.I. and Starkov, G.V. (1967) Dynamics of auroral belt and polar geomagnetic disturbances, Planet. Space Sci. 5:209.

Muldrew, D.B. (1965) F-region ionization trough deduced from Alouette data, J. Geophys. Res. 70:2635.

Rycroft, M.J., and Thomas, J.O. (1970) The magnetospheric plasmapause and the electron density trough at the Alouette I orbit, Planet. Space Sci. 18:65.

Sagalyn, R.C. and Smiddy, M. (1967) Charged particle measurements by means of electrostatic probes, electron density and temperature measurements in the ionosphere, Cospar Tech. Manual Ser., edited by K. Maeda, p. 90, Comm. on Space Res., Paris, France.

Sagalyn, R.C., Smiddy, M., and Wisnia, J. (1963) Measurement and interpretation of ion density distributions in the daytime F-region, J. Geophys. Res. 68:199.

Smiddy, M., and Stuart, R.D. (1969) An analysis of the behavior of a multi-grid spherical sensor in a drifting Maxwelliam plasma, Rep. AFCRL-69-0013, Phys. Sci. Res. Pap. 364, AFCRL, Bedford, Massachusetts.

Tulunay, Y. and Sayers, J. (1971) Characteristics of the Midlatitude trough as determined by the electron density experiment on Ariel III, J. Atmos. Terr. Phys. 33:1737.

Contents

3. Computation of the Electron Density During an Aurora From the Incident Energetic Electron Spectrum

J.C. Ulwick
Ionospheric Physics Laboratory
Air Force Cambridge Research Laboratories
Bedford, Massachusetts

3-1. GENERAL DESCRIPTION OF THE PROGRAM

A computer program is presented here which will calculate the electron density observed during an aurora from the measured spectrum of incident energetic electrons. The measured incident differential electron energy spectrum (dN/dE) gives the number of electrons/(keV-cm^2-sec-sr) as a function of energy (E) and is used to calculate the ionization rate per unit volume or ion-electron production rate, q(cm^{-3}-sec^{-1}), as a function of altitude from 85 to 150 km. The electron density, N_e, is computed at each altitude from the equation

$$N_e = \sqrt{\frac{q}{\alpha}}$$

where q is the production rate and α is an effective recombination coefficient.

The calculation of the production rate is based on the methods used by Rees (1963). Rees calculates the ionization rate per unit volume q, per incident unit electron flux F from the equation

$$\frac{q}{F} = \frac{\varepsilon_o / r_o}{\Delta\varepsilon_{ion}} \lambda \left(\frac{Z}{R}\right) \frac{n(M)_Z}{n(M)_R} \qquad (3\text{-}1)$$

where

ε_o is the initial energy of the electron.

$\Delta\varepsilon_{ion}$ is the mean energy loss per ion pair formed (35 eV).

$n(M)_Z$ is the number density of ionizable atoms or molecules at atmospheric depth $Z(gm/cm^2)$.

$n(M)_R$ is the number density of ionizable atoms or molecules at atmospheric depth $R(gm/cm^2)$.

R is the penetration depth $(gm/cm^2) = 4.57 \times 10^{-6} \varepsilon_o^{1.75}$ where ε_o is expressed in keV.

r_o is the range at the "top of the atmosphere" $= R/\rho$ where ρ is the mass density (gm/cm^3) at the lowest altitude of penetration.

$\lambda(Z/R)$ is the normalized energy dissipation distribution function and is tabulated in the program for various angular distributions of the incident electrons.

The various atmospheric parameters required for the calculation are listed in the program (Table 3-1).

The normalized energy dissipation distribution function, $\lambda\left(\frac{Z}{R}\right)$, is tabulated for three angular distributions of the incident electrons, monodirectional, cosine dependent, and isotropic over the downward hemisphere (Table 3-2). In this calculation the definition of isotropic is the same as that used by Berger et al (1970); that is, the intensity, defined as the number of particles crossing a unit area of surface perpendicular to the velocity vector, is constant over the downward hemisphere. This is not the same as Ree's definition and to compare his results with this work, the labels of cosine dependent and isotropic must be interchanged.

The equation given by Rees computes the production rate per incident unit electron flux. The program given here calculates the total electron flux in 70 energy intervals from 0.4 to 300 keV, and computes the contribution of each of these energy intervals at each altitude and adds them to obtain the total production rate at each altitude. To calculate the total energy flux, however, the differential energy spectrum, dN/dE, must be expressed as a function that has an indefinite integral. For example, if

$$\frac{dN}{dE} = 10^6 \, e^{-E/5keV} \, (cm^2\text{-sec-sr-keV})^{-1}, \qquad (3\text{-}2)$$

Table 3-1. Atmospheric Parameters Used in the Program

h (km)	Z (gm/cm^2)	ρ (gm/cm^3)	n(M) (cm^{-3})
60	2.34×10^{-1}	3.04×10^{-7}	6.33×10^{15}
64	1.37×10^{-1}	1.89×10^{-7}	3.93×10^{15}
68	7.76×10^{-2}	1.15×10^{-7}	2.39×10^{15}
72	4.20×10^{-2}	6.71×10^{-8}	1.39×10^{15}
76	2.17×10^{-2}	3.71×10^{-8}	7.72×10^{14}
80	1.08×10^{12}	1.94×10^{-8}	4.03×10^{14}
84	5.16×10^{-3}	9.59×10^{-9}	1.99×10^{14}
88	2.46×10^{-3}	4.56×10^{-9}	9.48×10^{13}
92	1.19×10^{-3}	2.17×10^{-9}	4.37×10^{13}
96	5.88×10^{-4}	9.93×10^{-10}	2.07×10^{13}
100	3.10×10^{-4}	4.48×10^{-10}	1.04×10^{13}
108	1.04×10^{-4}	1.32×10^{-10}	3.18×10^{12}
114	5.18×10^{-5}	5.70×10^{-11}	1.43×10^{12}
120	2.75×10^{-5}	2.61×10^{-11}	6.61×10^{11}
126	1.65×10^{-5}	1.30×10^{-11}	3.40×10^{11}
132	1.08×10^{-5}	7.05×10^{-12}	1.91×10^{11}
140	6.90×10^{-6}	3.47×10^{-12}	9.70×10^{10}
150	4.40×10^{-6}	1.70×10^{-12}	4.92×10^{10}
162	2.96×10^{-6}	9.00×10^{-13}	2.66×10^{10}
192	1.41×10^{-6}	2.94×10^{-13}	9.50×10^{9}
230	7.05×10^{-7}	1.16×10^{-13}	3.89×10^{9}
252	5.02×10^{-7}	7.60×10^{-14}	2.57×10^{9}
276	3.59×10^{-7}	5.00×10^{-14}	1.72×10^{9}
300	2.65×10^{-7}	3.42×10^{-14}	1.20×10^{9}

Table 3-2. Normalized Energy Dissipation Distribution Function λ(Z/R)

(Z/R)	λ(Z/R) Isotropic	Cosine Dependent	Monodirectional
0.0	1.48	1.65	0.77
0.025	1.49	1.88	0.82
0.050	1.50	1.90	0.88
0.075	1.49	.87	0.94
0.100	1.48	1.85	1.00
0.150	1.47	1.69	1.11
0.200	1.43	1.50	1.22
0.250	1.37	1.33	1.30
0.300	1.30	1.18	1.37
0.350	1.22	1.06	1.41
0.400	1.13	0.95	1.44
0.450	1.02	0.85	1.42
0.500	0.90	0.73	1.35
0.550	0.77	0.62	1.28
0.600	0.65	0.51	1.19
0.650	0.53	0.42	1.07
0.700	0.42	0.33	0.94
0.750	0.32	0.25	0.80
0.800	0.24	0.19	0.66
0.850	0.15	0.11	0.49
0.900	0.08	0.06	0.33
0.950	0.04	0.03	0.16
1.000	0.00	0.00	0.00

then the program requires the flux $N(cm^2\text{-sec})^{-1}$ expressed as a function of energy E in keV

$$\int \frac{dN}{dE}\, dE = (-5)(10^6)e^{-E/5}\ (cm^2\text{-sec-sr})^{-1} \tag{3-3}$$

and for an isotropic distribution as defined above, it is necessary to multiply the above expression by π to obtain the total flux.

$$N(E)(cm^2\text{-sec})^{-1} = (\pi)(-5)10^6\, e^{-E/5}\ . \tag{3-4}$$

This expression is entered into the program as a function subprogram named FINT. For the monodirectional case the flux is measured per $(cm^2\text{-sec})$, and for the cosine distribution Eq. (303) is multiplied by 2π.

The electron density, N_e, is then calculated from

$$N_e = \sqrt{\frac{q}{\alpha}}$$

where α, the effective recombination coefficient is approximated by (CIRA, 1965)

$$\alpha = 3 \times 10^{-7} \left(\frac{300}{T}\right) cm^3\text{-sec}^{-1}$$

where T is an effective temperature approximately equal to the electron temperature in the aurora. The effective recombination coefficient is a function of the positive ion composition and the ion and electron temperature (Swider, 1972; Biondi, 1969), but the above expression is adequate for calculating auroral electron densities from 85 to 150 km. Since auroral electron temperatures vary from one aurora to another and are not usually readily available, the neutral temperatures from the CIRA (1965) model have been used in the program (Table 3-3). This may be in error by a factor of 3 from the actual electron temperature, but this will introduce an error into the electron density of $\sqrt{3}$. This is the largest uncertainty in the computation, and the overall error in the calculated electron density should be less than a factor of two. Other sources of error include variations in the neutral density and composition, the positive ion composition, and the accuracy of the input electron spectrum.

Table 3-3. Temperature Values From the CIRA 1965 Mean Atmospheric Model

Altitude h(km)	Temperature T (^{o}K)	Altitude h (km)	Temperature T (^{o}K)
80	186	116	313
81	186	117	324
82	186	118	334
83	186	119	344
84	186	120	355
85	186	121	368
86	186	122	380
87	186	123	392
88	186	124	405
89	186	125	417
90	186	126	429
91	188	127	441
92	191	128	453
93	194	129	465
94	196	130	477
95	198	131	487
96	200	132	497
97	202	133	506
98	204	134	516
99	206	135	526
100	208	136	535
101	212	137	545
102	216	138	554
103	220	139	564
104	225	140	573
105	229	141	581
106	233	142	589
107	238	143	597
108	242	144	605
109	247	145	613
110	251	146	621
111	262	147	629
112	272	148	637
113	282	149	645
114	293	150	562
115	303		

3-2. DETAILED DESCRIPTION OF THE PROGRAM

This program was written for the Control Data 6600 computer, and slight Fortran modifications may be necessary if another computer is used.

3-2.1 Function Subprogram FINT

The program requires that the differential flux dN/dE $(cm^2\text{-sec-sr-keV})^{-1}$ be expressed as a function of energy E(in keV) that has an indefinite integral. The indefinite integral, N(E), is inserted into the program as a subprogram called FINT. If,

$$\frac{dN}{dE} = 10^3\, e^{-E/5keV}\ (cm^2\text{-sec-sr-keV})^{-1}, \tag{3-5}$$

then for an isotropic distribution as defined above

$$\frac{dN}{dE} = (\pi)\, 10^3\, e^{-E/5}\ (cm^2\text{-sec-keV})^{-1}$$

$$N(E) = \int \frac{dN}{dE}\, dE = (-5)(\pi)10^3\, e^{-E/5}\ (cm^2\text{-sec})^{-1}. \tag{3-6}$$

The function subprogram is then FUNCTION FINT(E).

```
FINT   = -5. * 3.14159 * 1000 * EXP(-E/5.)
RETURN
END
```

For the cosine dependent case, Eq. (3-5) is multiplied by 2π instead of π; and for the monodirectional case, the differential flux is not measured per unit solid angle.

Figure 3-1 shows the differential energy spectrum measured at 211 km during a visible aurora at Fort Churchill, Canada on 14 December 1966 (Reidy et al, 1968). This spectrum has been approximated by

$$\frac{dN}{dE} = 7 \times 10^7\, e^{-E/5keV}\ (cm^2\text{-sec-sr-keV})^{-1}$$

and used to calculate the production rate q, (for an isotropic distribution) and the electron density shown in Figure 3-2. There was no measurement made of electron density on this rocket.

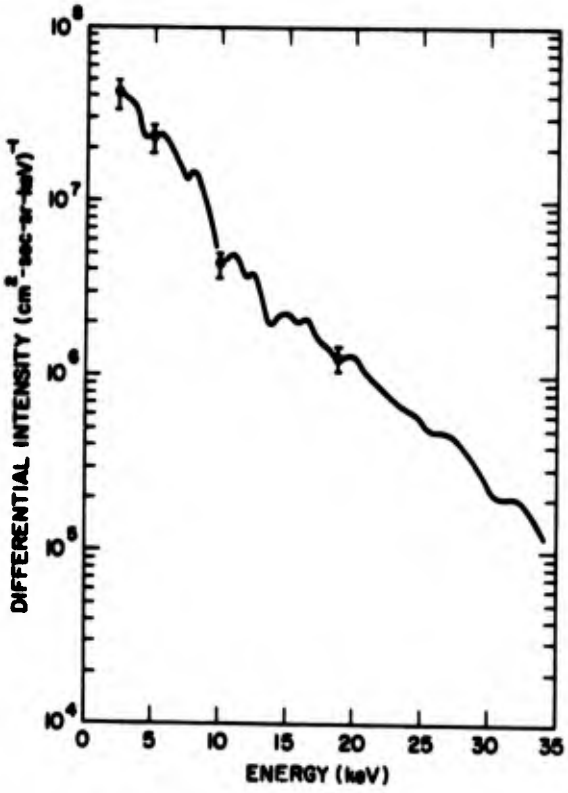

Figure 3-1. Differential Energy Spectrum of Electrons Measured During a Visible Aurora at Fort Churchill, Canada on 14 December 1966 at an Altitude of 211 km and a Pitch Angle of 64°

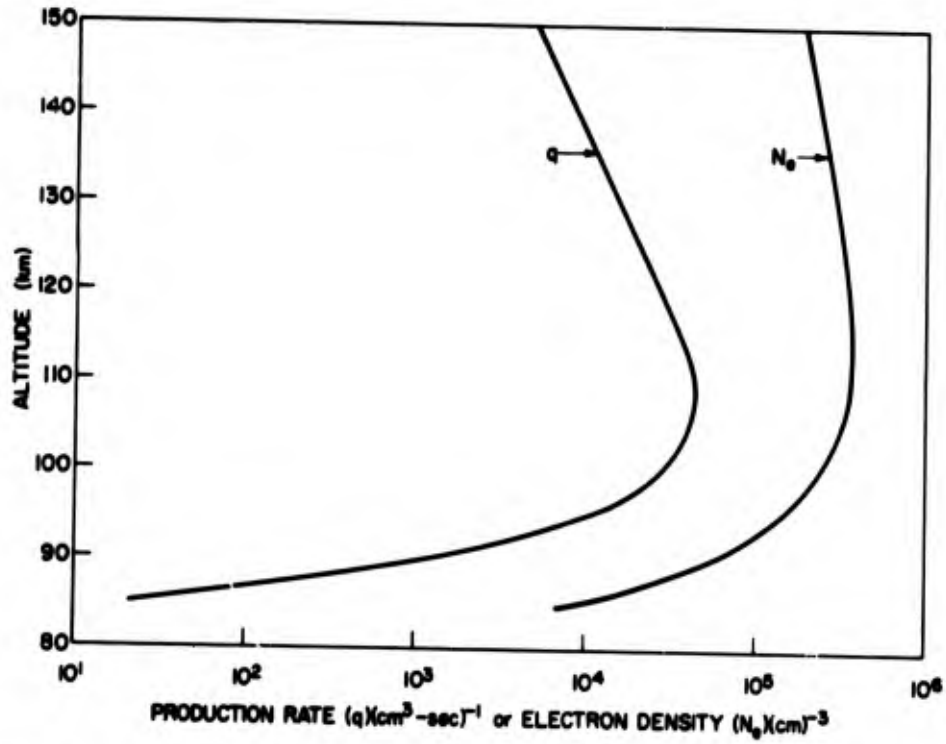

Figure 3-2. The Production Rate (q) and Electron Density (N_e) Calculated From the Approximation $\frac{dN}{dE} = 7 \times 10^7 \, e^{-E/4keV}$ $(cm^2\text{-sec-sr-keV})^{-1}$ to the Spectrum Shown in Figure 3.1

The output is listed with the following headings

Alt. Q N Q N Q N

where the altitude is in km, Q is the production rate $(cm^3\text{-sec})^{-1}$, and N the electron density (cm^{-3}). The first Q and N are for the isotropic distribution, the second set for the cosine distribution, and the last set for the monodirectional case. All three cases are printed-out even though the input to the program is arranged specifically for only one of these cases as explained above.

3.2.2 Data Cards

The first data card is one card of BCD information used as a title which is printed at the top of each page of printed output.

The next five data cards contain five constants: C1, C2, C3, C4, and C5. These constants are used in the following formulas:

$$R = C1 * \varepsilon_o^{C2}$$

$$\Delta\varepsilon_{ion} = C3$$

$$\alpha = \frac{C4 * C5}{T}$$

These constants have been given values:

C1 = 4.57E-6

C2 = 1.75

C3 = 0.035

C4 = 3.E-7

C5 = 300.

Then next follow seven sets of data cards, each set being a description of a function. These seven functions are:

(1) Z atmospheric depth (gm/cm^2), a function of h (altitude).

(2) N(M), a function of Z .

(3) ρ (gm/cm^2), a function of R(gm/cm^2).

(4) T, temperature, a function of h.

(5) The cosine dependent curve.

(6) The isotropic dependent curve.

(7) The monodirectional curve.

Each card of a given set is of the following form:

Column	Description
1-30	BCD description of the function
31-33	Number of the card in the given set
34	/ used as separator
35-37	Total number of cards in the given set
40-54	Abscissa value
55-69	Ordinate value

The next two cards contain the variable formats for the printout: Alphanumeric column heading for printout (1X, 7X*ALT*, 3(12X*Q*12*N*)) where ALT is altitude, Q is production rate and N is electron density. Format for printed output: (1XF10.2, 3(1P2E13.3)).

The next three cards contain the beginning, end, and number of divisions used in the altitude range. Values presently used allow calculations from 85 to 150 km in 1/2 km steps.

The last three cards contain the beginning, end, and number of divisions used in the energy range. Presently, there are 70 steps starting at 0.4 keV and ending at 300 keV.

A detailed description of the program is shown in Table 3-4. This table contains the steps to calculate the production rate and electron density from the incident energetic electron spectrum.

Table 3-4. Program to Calculate the Production Rate and Electron Density From the Incident Energetic Electron Spectrum

```
      PROGRAM DA(INPUT,OUTPUT,TAPE5=INPUT,TAPE6=OUTPUT,TAPE1)
      DIMENSION W(7),XL(4),S(4),Q(4),D(4)
      COMMON /CFUN/IFS,C(16),NC
      EXTERNAL FUN
      CALL RPTL
      C1=FR(42H(/* COEFFICIENT IN FORMULA FOR R=*1PE16.8))
      C2=FR(37H(/* EXPONENT IN FORMULA FOR R=*F15.5))
      C3=FR(24H(/* DELTA E-ION=*F15.10))
      DION=C3
      C4=FR(53H(/* FIRST OF CONSTANTS IN FORMULA FOR ALPHA=*1PE16.8))
      C5=FR(52H(/* SECOND OF CONSTANTS IN FORMULA FOR ALPHA=*F15.5))
      IFS=1
      CALL RCAL(1)
      CALL RCAL(2)
      CALL RCAL(3)
      CALL RCAL(4)
      NLAM=3
      IF(NLAM.LT.1.OR.NLAM.GT.4)GO TO 1000
      DO 300 I=1,NLAM
      CALL RCAL(I+5)
300   CONTINUE
      CALL RPF(1)
      HB=FR(25H(/* ALTITUDE BEGIN=*F10.2))
      HE=FR(24H(/* ALTITUDE END=*F10.2))
      NH=IR(37H(/* NUMBER OF ALTITUDE DIVISIONS=*I5))
      NDH=NH+1
      DH=(HE-HB)/NH
340   EB=FR(24H(/* ENERGY BEGIN=*F10.2))
      IF(IFS.NE.0)GO TO 360
      EE=EB
      NE=1
      GO TO 370
360   EE=FR(22H(/* ENERGY END=*F10.2))
      NE=IR(35H(/* NUMBER OF ENERGY DIVISIONS=*I5))
370   AEE=ALOG10(EE)
      AEB=ALOG10(EB)
      FLG=(AEE-AEB)/NE
      QQ=10.**FLG-1.
      WRITE(6,380)QQ
380   FORMAT(/10X*RESULTING FRACTIONAL INCREASE=*F20.10)
      DO 800 I=1,NDH
      H=HB+(I-1)*DH
      Z=CLOGI(H,1)
      XNZ=CLOGG(Z,2)
      DO 400 K=1,NLAM
      S(K)=0.
400   CONTINUE
      DO 600 J=1,NE
      E1=10.**(AEB+(J-1)*FLG)
      E2=10.**(AEB+J*FLG)
      EN=E1*(1.+QQ/2.)
      R=C1*EN**C2
      RHO=CLOGG(R,3)
      RN=R/RHO
```

Table 3-4 (Contd.). Program to Calculate the Production Rate and Electron Density From the Incident Energetic Electron Spectrum

```
      XNR=CLGLG(R,2)
      IF(IFS.NE.0)GO TO 420
      F=1.
      GO TO 480
420   IF(IFS.NE.1)GO TO 1000
      F=FINT(E2)-FINT(E1)
480   PP=F*EN/RN/DION*XNZ/XNR
      DO 500 K=1,NLAM
      XL(K)=CLINI(Z/R,K+5)
      Q(K)=PP*XL(K)
      S(K)=S(K)+Q(K)
500   CONTINUE
C     WRITE(6,510)J,E1,E2,EN,R,RHO,RN,XNR,F,PP,XL,Q,S
510   FORMAT(/* J=*I5/(1P8E16.8))
600   CONTINUE
      T=CLINI(H,4)
      AL=C4*C5/T
      DO 640 K=1,NLAM
      D(K)=SQRT(S(K)/AL)
640   CONTINUE
      W(1)=H
      DO 700 K=1,NLAM
      W(2*K)=S(K)
      W(2*K+1)=D(K)
700   CONTINUE
      CALL PLOM(1,1,W,1+2*NLAM,1,50,1)
C     WRITE(6,720)I,H,Z,XNZ,T,AL,S,D
720   FORMAT(/* I=*I5/(1PE16.8))
800   CONTINUE
      CALL PLOM(1,-1,W,1+2*NLAM,1,50,1)
      CALL CPCF(-1,6)
      STOP
1000  WRITE(6,1005)IFS,NLAM
1005  FORMAT(/* ERROR DA...*2I10)
      STOP
      END
      FUNCTION FINT(E)
```

```
      RETURN
      END
      SUBROUTINE FCAL(KC)
      COMMON /CZZZ/X(200,9),Y(200,9),YL(200,9),NC(9),NCMX,NARR,
     1  XL(200,9)
      DATA NCMX/200/,NARR/9/,KFRST/1/
      IF(KC.GT.NARR.OR.KC.LT.1)GO TO 1000
      IF(KFRST.NE.1)GO TO 40
      DO 20 I=1,NARR
```

Table 3-4 (Contd.). Program to Calculate the Production Rate and Electron Density From the Incident Energetic Electron Spectrum

```
20      NC(1)=0
        KFRST=0
40      K=0
60      K=K+1
        READ(5,80)H1,H2,H3,KCT,MC,X(K,KC),Y(K,KC)
80      FORMAT(3A10,I3  ,1XI3,2X2F15.0)
        IF(K.GT.1)GO TO 100
        F1=H1
        F2=H2
        F3=H3
        MCF=MC
        IF(MC.LT.2.OR.MC.GT.NCMX)GO TO 1000
        WRITE(6,90)KC,H1,H2,H3
90      FORMAT(/* NUMBER *I2* CALIBRATION CURVE FOR *3A10)
100     IF(H1.NE.F1.OR.H2.NE.F2.OR.H3.NE.F3)GO TO 1000
        IF(K.NE.KCT.OR.MC.NE.MCF)GO TO 1000
        IF(K.EQ.1)GO TO 105
        IF(X(K-1,KC).GE.X(K,KC))GO TO 1000
105     IF(Y(K,KC).GT.0.0)GO TO 110
        YL(K,KC)=1.E60
        WRN=3H***
        GO TO 120
110     YL(K,KC)=ALOG10(Y(K,KC))
        WRN=3H
120     IF(X(K,KC).GT.0.)GO TO 140
        XL(K,KC)=1.E60
        WRNX=3H***
        GO TO 180
140     XL(K,KC)=ALOG10(X(K,KC))
        WRNX=3H
180     WRITE(6,185)K,MC,WRNX,X(K,KC),WRN,Y(K,KC)
185     FORMAT(10X15*/*I3,2(3XA3,2X1PE16.8))
        IF(K.LT.MC)GO TO 60
        NC(KC)=MC
        RETURN
1000    WRITE(6,1005)K,KC
1005    FORMAT(/* ERROR RCAL...*2I10)
        STOP
        END
        FUNCTION CLINI(V,KC)
        COMMON /CZZZ/X(200,9),Y(200,9),YL(200,9),NC(9),NCMX,NARR,
     1  XL(200,9)
        N=NC(KC)
        IF(KC.LT.1.OR.KC.GT.NARR.OR.N.EQ.0)GO TO 1000
        IF(V.GT.X(1,KC))GO TO 100
        CLINI=Y(1,KC)
        RETURN
100     DO 200 I=2,N
        IF(V.GT.X(I,KC))GO TO 200
        CLINI=(Y(I,KC)-Y(I-1,KC))/(X(I,KC)-X(I-1,KC))*(V-X(I-1,KC))+
     1  Y(I-1,KC)
        RETURN
200     CONTINUE
        CLINI=Y(N,KC)
```

Table 3-4 (Contd.). Program to Calculate the Production Rate and Electron Density From the Incident Energetic Electron Spectrum

```
      RETURN
1000  WRITE(6,1005)KC
1005  FORMAT(/* ERROR CLINI...KC=*I10)
      STOP
      END
      FUNCTION CLOGI(V,KC)
      COMMON /CZZZ/X(200,9),Y(200,9),YL(200,9),NC(9),NCMX,NARR,
     1  XL(200,9)
      N=NC(KC)
      IF(KC.LT.1.OR.KC.GT.NARR.OR.N.EQ.0)GO TO 1000
      IF(V.GT.X(1,KC))GO TO 100
      CLOGI=Y(1,KC)
      RETURN
100   DO 200 I=2,N
      IF(V.GT.X(I,KC))GO TO 200
      CLOGI=10.**((YL(I,KC)-YL(I-1,KC))/(X(I,KC)-X(I-1,KC))*
     1  (V-X(I-1,KC))+YL(I-1,KC))
      RETURN
200   CONTINUE
      CLOGI=Y(N,KC)
      RETURN
1000  WRITE(6,1005)KC
1005  FORMAT(/* ERROR CLOGI...KC=*I10)
      STOP
      END
      FUNCTION CLGLG(V,KC)
      COMMON /CZZZ/X(200,9),Y(200,9),YL(200,9),NC(9),NCMX,NARR,
     1  XL(200,9)
      N=NC(KC)
      IF(KC.LT.1.OR.KC.GT.NARR.OR.N.EQ.0)GO TO 1000
      IF(V.GT.X(1,KC))GO TO 100
      CLGLG=Y(1,KC)
      RETURN
100   DO 200 I=2,N
      IF(V.GT.X(I,KC))GO TO 200
      CLGLG=10.**((YL(I,KC)-YL(I-1,KC))/(XL(I,KC)-XL(I-1,KC))*
     1  (ALOG10(V)-XL(I-1,KC))+YL(I-1,KC))
      RETURN
200   CONTINUE
      CLGLG=Y(N,KC)
      RETURN
1000  WRITE(6,1005)KC
1005  FORMAT(/* ERROR CLGLG...KC=*I10)
      STOP
      END
      SUBROUTINE CPCF(MTI,MTO)
      DIMENSION A(14)
      MT=MTI
      IF(MT.GT.0)GO TO 80
      MT=-MT
      REWIND MT
80    READ(MT,100)(A(I),I=1,14)
100   FORMAT(13A10,A2)
      IF(EOF(MT))140,120
```

Table 3-4 (Contd.). Program to Calculate the Production Rate and Electron Density From the Incident Energetic Electron Spectrum

```
 120    WRITE(MTO,100)(A(I),I=1,14)
        GO TO 80
 140    RETURN
        END
        FUNCTION FR(FMT)
        READ(5,80)FR
 80     FORMAT(F20.0)
        WRITE(6,FMT)FR
        RETURN
        END
        FUNCTION IR(FMT)
        READ(5,80)IR
 80     FORMAT(I20)
        WRITE(6,FMT)IR
        RETURN
        END
        SUBROUTINE PBFH(NSR,MTIN,MTOUT,NWPG,NGPL,NLPP,KUSR)
C               THIS SUBROUTINE CALLS @REB, AND @PLOH@
        DIMENSION D(20)
        IF(NWPG.GT.20)GO TO 1000
        MT=MTIN
        IF(MT.GT.0)GO TO 100
        MT=-MT
        REWIND MT
 100    CALL RBH(NSR,MT,D,NWPG,KQT)
        IF(KQT.NE.0)GO TO 300
        CALL PLOH(1,MTOUT,D,NWPG,NGPL,NLPP,KUSR)
        GO TO 100
 300    CALL PLOH(1,-MTOUT,D,NWPG,NGPL,NLPP,KUSR)
        RETURN
 1000   WRITE(6,1010)NWPG
 1010   FORMAT(* ERROR PBFH...NWPG=*I15)
        STOP
        END
        SUBROUTINE PLOH(NFP,MTP,G,NWPG,NGPL,NLPP,KUSR)
        DIMENSION G(1),X(50)
        DATA J/0/,IPAGE/0/,KLN/-1/,KP/-1/
        IF(NWPG*NGPL.GT.50)GO TO 1000
        MT=MTP
        IF(MT.GT.0)GO TO 80
        MT=-MT
        GO TO 140
 80     KP=KP+1
        IF(MOD(KP,NFP).NE.0)RETURN
        J=J+1
        DO 100 I=1,NWPG
        X((J-1)*NWPG+I)=G(I)
 100    CONTINUE
        IF(J.LT.NGPL)RETURN
        KGPL=NGPL
 120    NPTS=NWPG*KGPL
        KLN=KLN+1
        IF(MOD(KLN,NLPP).NE.0)GO TO 130
        IPAGE=IPAGE+1
```

Table 3-4 (Contd.). Program to Calculate the Production Rate and Electron Density From the Incident Energetic Electron Spectrum

```
      CALL PUSR(MT,X,NPTS,-KUSR)
130   CALL PUSR(MT,X,NPTS,KUSR)
      J=0
      IF(MTP.LT.0)GO TO 160
      RETURN
140   IF(J.EQ.0)GO TO 160
      KGPL=J
      GO TO 120
160   IPAGE=0
      J=0
      KLN=-1
      KP=-1
      RETURN
1000  WRITE(6,1010)NWPG,NGPL
1010  FORMAT(* ERROR PLOH...NWPG=*I15*  NGPL=*I15)
      STOP
      END
      SUBROUTINE PPHD(MTM)
C             THIS SUBROUTINE HAS ENTRY ORPTL)
      DIMENSION HCRD(8)
      DATA HCRD/8*10H
      KSW=0
      MT=MTM
100   WRITE(MT,120)(HCRD(I),I=1,8)
120   FORMAT(*1*/3X8A10/)
      IF(KSW.EQ.0)RETURN
      WRITE(6,140)
140   FORMAT(* INPUT CONSTANTS*/)
      RETURN
      ENTRY RPTL
      READ(5,180)(HCRD(I),I=1,8)
180   FORMAT(8A10)
      MT=6
      KSW=1
      GO TO 100
      END
      SUBROUTINE PUSR(MT,X,NX,KUSR)
      DIMENSION FMT(24,2,5),X(1)
      DATA FMT(1,1,1)/2H()/,FMT(1,1,2)/2H()/,FMT(1,1,3)/2H()/,
     1  FMT(1,1,4)/2H()/,FMT(1,1,5)/2H()/,FMT(1,2,1)/8H(8E16.8)/,
     2  FMT(1,2,2)/8H(8E16.8)/,FMT(1,2,3)/8H(8E16.8)/,FMT(1,2,4)
     3  /8H(8E16.8)/,FMT(1,2,5)/8H(8E16.8)/
      DATA KLP/51B/,KRP/52B/,NFMTX/5/
      KW(I)=(I-1)/10+1
      KC(I)=I-(KW(I)-1)*10
      IF(KUSR.GT.0)GO TO 100
      CALL PPHD(MT)
      KHF=-KUSR
      IF(KHF.LT.1.OR.KHF.GT.NFMTX)GO TO 1000
      WRITE(MT,FMT(1,1,KHF))
      RETURN
100   IF(KUSR.LT.1.OR.KUSR.GT.NFMTX.OR.NX.LT.1.OR.NX.GT.50)GO TO 1000
      WRITE(MT,FMT(1,2,KUSR))(X(I),I=1,NX)
      RETURN
```

Table 3-4 (Contd.). Program to Calculate the Production Rate and Electron Density From the Incident Energetic Electron Spectrum

```
      ENTRY RPF
      IF(MT.LT.1.OR.MT.GT.NFMTX)GO TO 2000
      WRITE(6,110)MT
110   FORMAT(/* NUMBER *I2* FORMAT SET*)
      DO 300 I=1,2
      NLP=0
      NRP=0
      DO 280 J=1,3
      KB=1+(J-1)*8
      KE=KB+7
      READ(5,200)(FMT(K,I,MT),K=KB,KE)
200   FORMAT(8A10)
      IF(EOF(5))2000,210
210   DO 260 K=1,80
      KT=MXGETX(FMT(KW(K)+(J-1)*8,I,MT),KC(K),1,
      IF(K.EQ.1.AND.J.EQ.1.AND.KT.NE.KLP)GO TO 2000
      IF(KT.NE.KLP)GO TO 220
      NLP=NLP+1
220   IF(KT.NE.KRP)GO TO 240
      NRP=NRP+1
240   IF(NRP.EQ.NLP)GO TO 290
260   CONTINUE
280   CONTINUE
      GO TO 2000
290   NGO=J*8
      WRITE(6,295)(FMT(K,I,MT),K=1,NGO)
295   FORMAT(10X*--->*8A10*<---*)
300   CONTINUE
      RETURN
1000  WRITE(6,1005)NX,KUSR
1005  FORMAT(/* ERROR PUSR...*2I10)
      STOP
2000  WRITE(6,2005)MT,I,J,K,NLP,NRP
2005  FORMAT(/* ERROR RPF...*6I10)
      STOP
      END
```

References

Berger, M.J., Seltzer, S.M. and Maeda, K. (1970) J. Atmos. Terr. Phys. 32: 1015-1045.

Biondi, M.A. (1969) Can. J. Chem. 47:1711-1722.

COSPAR International Reference Atmosphere (CIRA) (1965) North Holland, Amsterdam.

Rees, M.H. (1963) Planet. Space Sci. 11:1209-1218.

Reidy, W.P., Hegblom, E.R. and Ulwick, J.C. (1968) J. Geophys. Res. 73: 3072-3076.

Swider, W. (1972) J. Atmos. Terr. Phys. 34:1615-1626.

Contents

4. A Numerical Model of TEC Over Europe for Sunspot Minimum Conditions

J. Klobuchar
Ionospheric Physics Laboratory
Air Force Cambridge Research Laboratories
Bedford, Massachusetts

4-1. INTRODUCTION

Results of two studies of the TEC of the ionosphere over Europe have been given by Amayenc (1971). They presented contours of equal TEC values as a function of geographic latitude and local time over the 40- to 72-deg geographic latitude range over Europe for nine seasons in the 1964-1967 period. The TEC data shown in their isocontour maps was taken from two stations in Europe, from Kiruna, Sweden, and from Val Joyeux, near Paris, France. Original glossy prints of the isocontours in the Amayenc et al (1971) paper* were kindly provided by F. Bertin for use in this report. TEC hourly values were scaled from these glossy prints at 5-deg geographic latitude intervals, and a Fourier time series expansion of harmonic number 4 was made to each latitude set. A least squares third degree polynomial then was fitted separately to each Fourier coefficient over the latitude range from 40 to 70 deg. The resultant coefficients equal 36 in number; one set of 4 polynomial coefficients to represent the latitude dependence of each of

* Amayenc, P., Bertin, F., and Papet-Lepine, J. (1971) Sur l'evolution latitudinale du contenu electronique de l'ionosphere, Annales de Geophysique 27(No. 3):345-357.

the 9 Fourier terms. Thus, a set of 36 numbers specify the seasonal mean TEC behavior over the 40- to 70-deg geographic latitude range. All that is necessary to obtain a value of TEC is to use the coefficients for the season desired, and to specify a latitude and local time. The model is in the following form:

$$TEC = DC + 2 \sum_{i=1}^{4} C_i \cos (it - 2\Pi\phi_i/24)$$

where DC, C and $\phi = K_0 + \sum_{j=1}^{3} K_j(lat)^j$ for the appropriate DC, C_i or ϕ_i term.

The coefficient sets for the seasons are given in Table 4-1. Table 4-2 contains a list of the months in each season along with the mean observed 10.7-cm solar flux over each season. Note that the mean 10.7-cm solar flux was nearly the same for all seasons.

In order to determine how well the numerical coefficients represent the actual data, the TEC values obtained from the model were subtracted from the original contour values at 5-deg latitude intervals. The resultant errors are shown for the four seasons in Table 4-3. Differences less than 1×10^{16} were left blank, as this is probably the experimental accuracy of the original data. Note that the model fit is good indeed, as evidenced by the large blank areas in the table. Figure 4-1A is an isocontour of TEC as constructed by the numerical model for season 1 of the four seasons. It compares well with the original isocontour for this season which is shown in Figure 4-1B.

This model should have use in determining average TEC values for a given season for time delays, satellite navigation, and satellite detection radars operating in the VHF-UHF bands. It is not intended for use in a day-to-day operational mode, but as an average background model. It will be particularly useful as a representative TEC background model for the approaching 1974-1975 solar minimum conditions for system design studies for the European sector.

Table 4-1. Seasonal Coefficients Sets

Season	Poly. Term	DC	C1	C2	C3	C4	PHI1	PHI2	PH13	PH14
1	K-ZERO	-0.364E+02	0.305E+02	-0.871E+01	0.591E+01	0.867E+01	0.337E+02	0.717E+02	-0.139E+04	-0.152E+02
1	K1	0.254E+01	-0.162E+01	0.532E+00	-0.345E+00	-0.486E+00	-0.123E+01	-0.443E+01	0.801E+02	0.582E+00
1	K2	-0.498E-01	0.299E-01	-0.981E-02	0.669E-02	0.903E-02	0.247E-01	0.902E-01	-0.130E+01	0.180E-01
1	K3	0.306E-03	-0.184E-03	0.590E-04	-0.423E-04	-0.550E-04	-0.159E-03	-0.582E-03	0.918E-02	-0.303E-03
2	K-ZERO	-0.239E+02	0.208E+02	0.103E+02	0.368E+01	0.602E+01	0.457E+02	-0.961E+01	0.229E+03	0.164E+03
2	K1	0.187E+01	-0.105E+01	-0.652E+00	-0.198E+00	-0.413E+00	-0.183E+01	0.725E+00	-0.140E+02	-0.803E+01
2	K2	-0.366E-01	0.192E-01	0.136E-01	0.360E-02	0.808E-02	0.363E-01	-0.362E-02	0.286E+00	0.135E+00
2	K3	0.225E-03	-0.118E-03	-0.908E-04	-0.213E-04	-0.510E-04	-0.241E-03	-0.222E-04	-0.190E-02	-0.753E-03
3	K-ZERO	0.209E+02	0.160E+02	-0.281E+02	-0.675E+01	-0.297E+01	-0.799E+02	0.577E+02	-0.429E+03	0.482E+03
3	K1	-0.642E+00	-0.660E+00	0.167E+01	0.450E+00	0.209E+00	0.556E+01	-0.263E+01	0.264E+02	-0.262E+02
3	K2	0.101E-01	0.950E-02	-0.310E-01	-0.925E-02	-0.415E-02	-0.103E+00	0.580E-01	-0.514E+00	0.468E+00
3	K3	-0.519E-04	-0.459E-04	0.186E-03	0.607E-04	0.253E-04	0.602E-03	-0.405E-03	0.324E-02	-0.270E-02
4	K-ZERO	-0.304E+02	0.158E+02	-0.167E-01	-0.353E+01	-0.405E+01	-0.497E+02	-0.576E+03	-0.716E+03	0.401E+03
4	K1	0.229E+01	-0.758E+00	-0.172E-01	0.185E+00	0.235E+00	0.386E+01	0.320E+02	0.418E+02	-0.224E+02
4	K2	-0.451E-01	0.136E-01	0.685E-03	-0.304E-02	-0.434E-02	-0.730E-01	-0.559E+00	-0.780E+00	0.418E+00
4	K3	0.280E-03	-0.810E-14	-0.555E-05	0.162E-04	0.263E-04	0.444E-03	0.313E-02	0.472E-02	-0.252E-02

Table 4-2. Seasonal Solar Flux

Season	Month	2800 MHz Observed Flux	Mean Seasonal Observed Flux
I	November 1964	72.8	75.9
	December 1964	77.5	
	January 1965	77.5	
II	February 1965	74.6	73.4
	March 1965	73.8	
	April 1965	71.9	
III	May 1965	77.9	76.4
	June 1965	77.0	
	July 1965	74.3	
IV	August 1965	74.8	76.9
	September 1965	76.3	
	October 1965	79.6	

Table 4-3. Difference Between Model and Actual TEC (units of 10^{16} el/m^2)

Winter, 1964-1965	Hour																							
Latitude	0	1	2	3	4	5	6	7	8	9	10	11	12	13	14	15	16	17	18	19	20	21	22	23
70											1						1							
65			1	1			-1	-1			1					-1	-1		1			-1	-1	-1
60			1	1			-1	-1									-1		1					
55	-1				1			-1	-1		1	1	1						1	1			-1	-1
50	-1			1																				-1
45																-1	-1					1		
40										1							-1	1	1					

Spring, 1965	Hour																							
Latitude	0	1	2	3	4	5	6	7	8	9	10	11	12	13	14	15	16	17	18	19	20	21	22	23
70	1																							-1
65																-1				-1	-1			-1
60																			1					
55															1			1						
50																				-1				
45																								
40																								

Summer, 1965	Hour																							
Latitude	0	1	2	3	4	5	6	7	8	9	10	11	12	13	14	15	16	17	18	19	20	21	22	23
70																								
65			1			-1											-1							
60												-1												
55				-1	-1	-1													1	1	1	1		
50		-1	1	1	1							1		1						-2	-1		1	1
45	-1								-1	-1						-1		1			-1	-1	1	1
40	-1		1			-1		1										1		-1		1	1	-1

Autumn, 1965	Hour																							
Latitude	0	1	2	3	4	5	6	7	8	9	10	11	12	13	14	15	16	17	18	19	20	21	22	23
70																								
65																								
60				1	1	1						-1	-1			1				1				
55	-1	-1		1	1	1					-1	-1	-1			1	1	1	1	1	1			-1
50												1		-1								-1	-1	-1
45																				1				
40																								

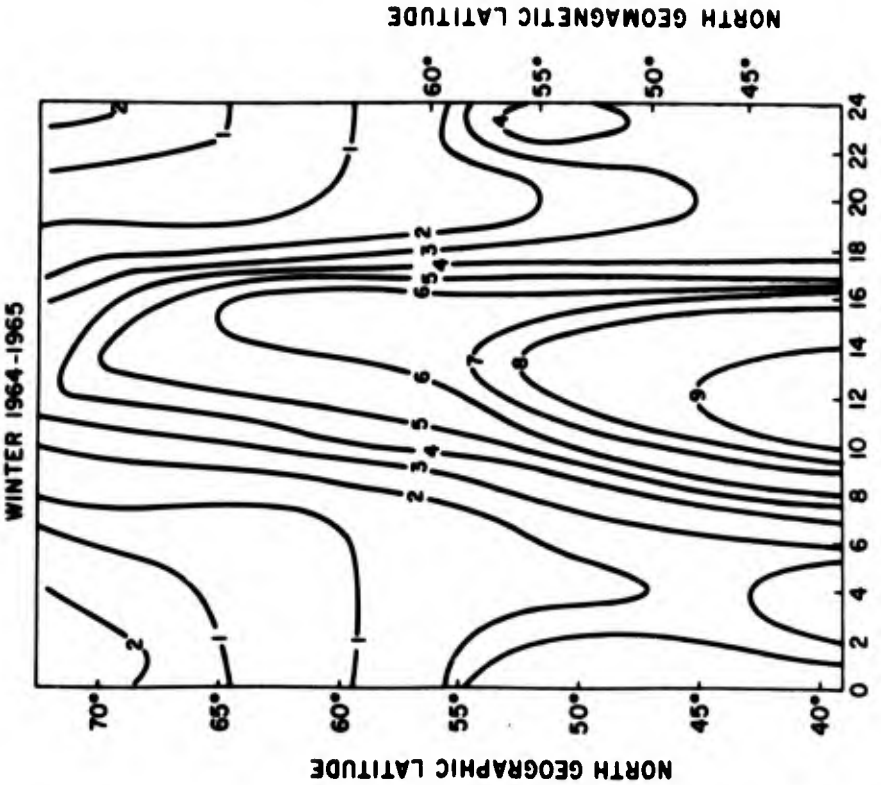

Figure 4-1b. Original Isocontour of TEC Over Northern Europe, Winter 1964-65

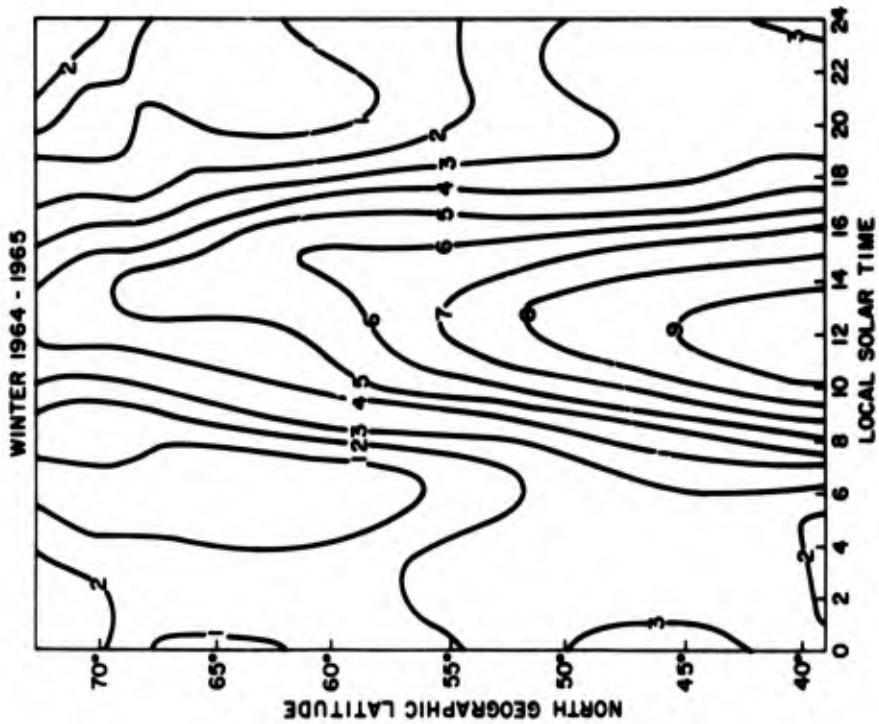

Figure 4-1a. Isocontour of TEC Over Northern Europe as Reconstructed by the Numerical Model, Winter, 1965-65